A Continuum Model for Needlepunched Nonwoven Fabrics

by

Petch Jearanaisilawong

Sc.B., Brown University (2002)
S.M., Massachusetts Institute of Technology (2004)

Submitted to the Department of Mechanical Engineering
in partial fulfillment of the requirements for the degree of

Doctor of Philosophy in Mechanical Engineering

at the

MASSACHUSETTS INSTITUTE OF TECHNOLOGY

June 2008

Signature of Author ....
Department of Mechanical Engineering
May 30, 2008

Certified by ....
Simona Socrate
d'Arbeloff Assistant Professor of Mechanical Engineering
Thesis Supervisor

Accepted by ....
Lallit Anand
Professor of Mechanical Engineering
Chairman, Department Committee on Graduate Students

A Continuum Model for Needlepunched Nonwoven Fabrics

by

Petch Jearanaisilawong

Submitted to the Department of Mechanical Engineering
on May 30, 2008, in partial fulfillment of the
requirements for the degree of
Doctor of Philosophy in Mechanical Engineering

Abstract

Nonwoven fabrics are sheet structures created by bonding or interlocking a web (network) of fibers through mechanical, thermal or chemical processes. In general, the mechanical response of nonwoven fabrics exhibits two major characteristics. First, the mechanical response can vary significantly when the fabric is loaded along different directions, depending on the existence of a preferential orientation in the fiber arrangement and/or in the pattern of inter-fiber bonding/entanglement. Second, the mechanisms of deformation include elastic and inelastic components, accompanied by an irrecoverable evolution of the texture of the fiber network.

In this work, we propose a three-dimensional, large strain continuum model for the constitutive behavior of nonwoven fabrics that accounts for the fiber network characteristics responsible for its anisotropic behavior, and captures the effects of deformation mechanisms at the micro-scale (fiber and bonds/entanglement) level. The model consists of two constitutive components: a nonlinear elastic component representing the resistances to recoverable deformation mechanisms, and a non-linear inelastic component representing the resistances to irrecoverable deformation and texture evolution. For nonwoven fabrics in which the anisotropy of fiber orientation is combined with random entanglement processes, we propose to capture the combined effects of fibers and junctions orientation distributions using a single tensorial representation of the network anisotropy (fabric ellipsoid). An orthotropic elastic constitutive model for the elastic response of nonwoven fabrics is then formulated based on this structural measure and deformation mechanisms of the network structure. The inelastic component of the model is then prescribed in terms of an evolution law for the fabric ellipsoid.

A needlepunched web of high strength polyethylene fibers, "Dyneema Fraglight", is selected as the representative material, to be used as a test case to validate the proposed modeling approach. The model is shown to capture the macroscopic nonlinear anisotropic elastic-inelastic response of the fabric in planar deformation, as well as the underlying micromechanical deformation mechanisms, such as fiber stretch, and irrecoverable evolution of fabric texture. The proposed model can be used to predict the mechanical behavior of nonwoven fabrics and can be combined with other continuum models to aid in the design of multi-component structures. In addition, the proposed elastic formulation can be used to model different classes of anisotropic network materials, such as biological tissues, and tissue engineering scaffolds.

Thesis Supervisor: Simona Socrate
Title: d'Arbeloff Assistant Professor of Mechanical Engineering

Acknowledgements

Given the scope of this work, I would not have accomplished it alone without support of many individuals. My appreciation goes out to them, and I would like to acknowledge some of them here.

First of all, I would like to thank my thesis advisor, Professor Simona Socrate, for her insightful guidance and continued support over these years at MIT. I consider myself quite fortunate to be able to work with an advisor who is as caring and as dedicated to her student as she is. I cannot thank you enough for what you have done for me. Thanks Simona!

I also would like to express my gratitude to Professor Parks and Professor Rutledge for serving on my thesis committee and providing thoughtful suggestions.

I would like to thank my past and present officemates at MIT: Mike King, Anastassia Paskaleva, Kristin Myers, Asha Balakrishnan, Bruce Wu, Timothy Johnson, Thibault Prevost, Jamie Kofoid. You guys are great! My life at MIT was so enjoyable because of all of you. I also would like to thank Una Sheehan and Ray Hardin for all the administrative support and every words of encouragement they provided over the years.

After having been away from home over these long years, I have developed a group of Thai friends who are more like another family here. I would like to thank my second family at the 16 Corinthian – Wang, Fu, N Fang, P Gift, P Tik, Sup, P Peng, and Joy. Thanks for being there to listen when I had something to say, for sharing all the good and bad times together, and for living with me. I would like to acknowledge people who have been sharing great time with me in Boston - N Kai, N Ton, N Jin, N Prae, N Gift, N Bird, N Ta, N Kob, Pounds, P Yai, and many others.

Finally, I would like to thank my family in Thailand for their advice, support and love they have provided. Thank you for always being there for me.

Contents

B Application of the Effective Stretch 151

List of Figures

List of Tables

Chapter 1

Introduction

1.1 Motivation

Nonwoven fabrics have been widely used in conventional applications such as apparels and protective clothing. With the advancement of related technologies, nonwoven fabrics have become an integral part of novel applications. For example, nonwoven fabrics manufactured from nano-size electrospun fibers can be used as filters for molecular-size particles, or scaffolds for tissue engineering. Nonwoven fabrics created from high strength-low density polymer fibers are used in a variety of structural applications, ranging from ballistic protective gears to the reinforcement in composite materials (Figure 1-1).

Increasing numbers of nonwoven fabric applications create a demand for a better under-

Figure 1-1: Nonwoven fabric applications: (a) nano filter, (b) protective gear, and (c) composite mat

standing of the mechanical behavior of nonwoven fabrics. Early studies of the mechanics of nonwoven materials focused primarily on applications for apparel and protective clothing industries. Attention was given to the development of fabric characterization techniques and nonwoven models that were capable of predicting the behaviors of textile materials. However, the introduction of novel technologies, especially in composite technology, requires new approaches for studying nonwoven fabrics as components of more complex structures.

1.2 Background

Nonwoven fabrics are sheet structures created by bonding or interlocking a web (network) of fibers through mechanical, thermal or chemical processes. In general, the mechanical response of nonwoven fabrics exhibits two major characteristics. First, the mechanical response can vary significantly when the fabric is loaded along different directions, depending on the existence of a preferential orientation in the fiber arrangement and/or in the pattern of inter-fiber bonding/entanglement. Second, the mechanisms of deformation include elastic and inelastic components, accompanied by an irrecoverable evolution of the texture of the fiber network.

This study focuses on the mechanical response of high performance ballistic nonwoven fabrics. Many of the commercially available ballistic nonwoven fabrics are provided in the form of needlepunched nonwoven felts. In this work, a web of high strength polyethelene fibers manufactured by DSM "Dyneema Fraglight" is selected as the representative material. This needlepunched fabric is created by entanglements of a single fiber material, hence, its mechanical response is governed by the properties of the web layout, which usually are expressed in terms of statistical distributions of the geometrical features such as fiber entanglement, fiber curl and fiber orientation, and the mechanical properties of constituent fibers.

Previous experimental characterizations of nonwoven fabrics can be classified into two categories. The first category focuses on the characterization of the fabric morphological properties by means of image analysis techniques. A number of image analysis algorithms were developed to measure specific geometric properties such as fiber orientation distribution [34], [64], fiber curl distribution [78], and fabric weight distribution [22], [33] from images of the fabric surface. Ad-hoc algorithms were typically developed for input images taken from specific acquisition systems such as front illumination with filtration [64], or backscattering light [33], [34]. Most algorithms also required pre-conditioning of the input images using a sequence of image-processing methods [64]. The second category focuses on the characterization of the mechanical macroscopic response, and the mesoscale deformation mechanisms of nonwoven fabrics under in-plane modes of deformation, particularly uniaxial tension (e.g., [8], [23], [61]). For additional references on the mechanical characterizations of nonwoven fabrics, see [43].

A number of nonwoven fabric models were developed based on the mechanical response observed in the experiments. In general, these models can be categorized into four main approaches based on the method of idealizations of nonwoven materials.

The first approach models the macroscopic response of nonwoven fabrics by idealizing them as either a homogeneous continuum or a composite of homogeneous components. This idealization forgoes the analysis of fiber interactions within the fabric microstructures for an ability to predict the macroscopic response of the fabrics at a low computational cost. The fabric continuum models can be easily interfaced with other continuum material models to create complex models for hierarchical structures. Examples of the "single homogenous continuum models" include the linear elastic orthotropic model by Backer and Petterson [4] for an area-bonded nonwoven fabric, and by Chocron [23] for a needlepunched nonwoven. These models do not retain any information relating to the structure of the material at the mesoscale (fiber) level, such as the non-uniform distribution of fiber entanglements in needlepunched nonwovens, or the bond pattern in area-bonded nonwoven fabrics, and cannot account for the effects of mesoscale deformation mechanisms on the macroscopic fabric response. A second class of continuum models idealizes nonwoven fabrics as composite structures consisting of many continuum components, representing idealized elements of the fabric structure. Lee and Argon [51] proposed a self-consistent model which idealizes the fabric as a composite structure consisting of stiff linear through-thickness disks, representing the junction points, surrounded by a softer matrix, representing the unconstrained fibers. This model was developed primarily to predict the fabric bending behavior, and is not applicable to predict the fabric behaviors under other modes of deformation. To incorporate the effect of non-uniform fiber orientation distribution, Bias-Singh et al. [8] and Liao and Adanur [53], [54] proposed composite laminate models, consisting of planar fiber layers, each with a single fiber orientation. The mono-directional layers are then stacked at relative angles from each other in an arrangement that tries to match the "average" fabric macroscopic anisotropy. The models are implemented in planar finite element frameworks. The layers of different fiber orientations (laminae) are stacked and bonded along the entire contacting interface, and the model response is calculated according to the laminate composite theory. These models are shown to capture some aspects of fabric anisotropy arising from non-uniform fiber orientation distribution, particularly in the small strain regime. However, because the fibers are fixed within the laminae, and the laminae cannot slide relative to one another, re-orientation of the fibers is over-constrained. Also, because the laminae are bonded at the interface, modeling locally irrecoverable deformation mechanisms, such as fiber slipping, fiber disentanglement, and bond breaking, is not feasible. Liao and Adanur's model tries to account for the macroscopic effects of fiber rupture during the deformation process, by introducing a failure criterion at the element interfaces.

The third approach models nonwoven fabrics as a complex fiber-network structure, and the macroscopic response of the fabric is calculated from the interactions between the components of the structure, particularly at the fiber and bond levels. This microstructurally-based approach has the benefit of capturing the physics of fabric deformation mechanisms at the expense of a high computational cost. Typical microstructurally-based models idealize nonwoven fabrics as a two-dimensional network consisting of an arrangement of individual fibers and bonds that tries to mimic the observed fabric morphological properties. A number of the models that were developed based on this approach consider the *fibers* as the essential elements of the fabric. They construct an idealized fiber network, and follow fiber deformation and displacement histories, accounting for interactions between the constituent fibers and considering the bonds as "indestructible" [15]-[17], [75]. A complementary approach considers the bonds as the essential elements, following the displacement history of the bonds and allowing for some evolution of the bond structure [36], [44]. Due to their extremely high computational costs, network models are typically limited to two-dimension. Therefore, these models cannot be used to predict out-of-plane bending and twist response of the fabric. In an attempt to overcome this limitation, Termonia [70] introduced a discrete lattice model as a computationally efficient compromise that allows some consideration of three-dimensional effects to predict the bending behavior of heat-bonded sheets. In this model the fabric is represented as a stack of initially-planar arrays of fiber strands aligned along x-y edges of lattice layers. Fibers are bonded within the same layer and across all layers in the stack at locations consistent with the heat bonding patterns. The model was shown to capture the fabric bending behavior with good degree of accuracy. However, its practical applicability is limited by the high computational expense required to formulate even a small area of fabric as an array of discrete lattices.

The fourth approach models the macroscopic response of nonwoven fabrics by homogenizing the response of a representative volume (or area) element of the material. This class of models enjoys the benefits of both continuum and microstructurally-based approaches by being computationally efficient while still capturing the physics of fabric deformation mechanisms. Petterson [63] introduced the 'fiber web' model, an analytical approach that treats the fabric as a periodic array of "unit cells" containing a statistical distribution of fibers with orientations consistent with the macroscopic fabric texture. The macroscopic response of the fabric is obtained by homogenizing the response of the unit cell to a given mode of deformation (e.g., uniaxial tension). The fibers in the cell are straight, the junctions are rigid, and the fiber network is taken to deform affinely with the macroscopic deformation. The fabric normal stress component in a given direction is obtained by integrating the fibers tension contributions across a cutting plane normal to that direction. The fiber web model was later modified by Hearle et al. [39] to incorporate the effect of fiber curls, and again by Kothari and Patel [50] to include the creep response of individual fibers by formulating an empirical fiber stress-stretch response as a function of time. This class of models has been developed to provide the response of the material under uniaxial loading, and has not been cast in terms of a generalized formulation in which the complete stress state is obtained in terms of an arbitrary deformation history. The fiber web model and its variations were shown to capture the small strain responses of both needlepunched and thermal bonded nonwoven fabrics under uniaxial tension. However, some inelastic deformation mechanisms, such as irrecoverable textural evolution, are notably missing from these models. Narter et al. [58] introduced a micromechanics-based anisotropic continuum model for the small-strain elastic response of fibrous materials that incorporates the effects of fiber orientation and inter-fiber interactions in a representative cubic volume element. The fabric anisotropy was modeled by expressing the coefficients of the elastic stiffness matrix as a linear combination of the spherical harmonic coefficients of the fiber orientation distribution.

However, no experimental validation of the model was provided.

The phenomena that control the compaction of fiber web materials, such as volume exclusion, are quite distinct from the fiber-stretching mechanisms that control their tensile behavior. Correspondingly, a separate class of microstructurally-based continuum models was developed primarily to capture the fabric compressive behavior. Van Wyk [73] pioneered this area by analyzing the bending behavior of two orthogonal yarn families based on the classic beam theory. Van Wyk's fiber-on-fiber compression model was later modified by Pan and Carnaby [60], Carnaby and Pan [20], and Komori et al. [48]-[47] to include the effects of fiber curl and fiber orientation distributions. Wilde [74] proposed another microstructurally-based continuum model for the compression behavior of goosedown. This model was formulated based on three underlying mechanisms; fiber bending, fiber straightening and fiber slipping. The model also addresses the effect of fiber orientation, as well as the softening behavior observed in the cyclic loading experiments of the material. This class of models focuses on capturing the compression behavior of nonwoven webs, and is generally not effective in predicting fabric response under other modes of deformation.

1.3 Objective

The objective of this project is to develop a continuum model for nonwoven fabrics that meets the following requirements:

1) The model should be able to predict the macroscopic response of the fabrics (i.e., stress and strain or load and displacement responses) as well as to capture the important features of the deformation mechanisms at the structural level, such as the fiber re-orientation, and the interactions between fibers.

2) The model should be of practical use. Many of the proposed models, although they can effectively predict fabric response under certain modes of deformation, are not of practical use because of the high computational expense or the limitations imposed by the models. In addition, the fabric model should also be able to interface with other material models to aid in the design of multi-component structures required by the new technologies.

With such requirements, the most suitable approach to model the mechanical response of nonwoven fabrics is by means of microstructurally-based continuum approach. The main advantage of the continuum models is their efficiency in modeling a large scale fabric application. And by homogenizing the response of the representative fiber network accounting for the elastic and inelastic deformation mechanisms based on the fabric macroscopic response, the continuum models can also capture the fabric behavior at the microstructural level. In addition, the continuum models can be easily interfaced with the continuum models of different materials to formulate models of hierarchical structures.

1.4 Model formulation approach

This project is divided into two parts. The first part addresses the characterization of fabric microstructure and the investigation of deformation mechanisms of nonwoven fabrics under different modes of deformation. The second part relies on the characterization of morphological properties of the material and the observed deformation mechanisms, to formulate a microstructurally-based continuum model for nonwoven materials. In formulating the fabric model, attentions are given to (1) the effects of material anisotropy arising from directional variations in fabric morphology, and (2) the inelastic effects of irrecoverable textural evolution. The model formulation is divided into a 2-step approach:

Step 1) Formulating an anisotropic elastic continuum model based on the material anisotropy In developing the anisotropic elastic model we consider two primary morphological sources of mechanical anisotropy in nonwoven fabrics:

1) *Fiber orientation distribution (FOD)* – This distribution represents the normalized probability of having fibers aligned in each material direction, and gives rise to deformation resistance biased toward the directions of preferential fiber alignment.

2) *Orientation distribution of junction-to-junction distance (JJD)* – the normalized distance between two junctions in each material direction. This distribution is related to the anisotropy of the extensibility limits of the network, and gives rise to the stress contributions that are biased in the directions of long junction-to-junction distances.

For nonwoven fabrics in which the anisotropy of fiber orientation is combined with random entanglement processes, we propose to capture the combined effects of fibers and junctions orientation distributions using a single tensorial representation of the network anisotropy (fabric ellipsoid). An appropriate orthotropic form for the stress tensor based on this structural measure will be derived.

Step 2) Incorporating anelastic effects arising from irrecoverable texture evolution The orthotropic elastic model from Step 1 will be modified to include unrecoverable deformation mechanisms observed in the nonwoven fabric experiments. The inelastic component of the constitutive model will reflect the evolution of the network structure due to irrecoverable realignment of the constituent fibers, as well as other resistive mechanisms to inelastic deformation, such as inter-fiber friction and volume exclusion.

1.5 Thesis organization

This thesis will be organized as follows. Chapter 2 presents the experimental characterizations of nonwoven fabrics. Attention is given to the investigation of deformation mechanisms of nonwoven fabrics under different modes of deformation as well as the characterization of fabric microstructure. Motivated by deformation mechanisms in nonwoven fabric observed in the experiments, we propose a microstructurally-based continuum model consisting of two constitutive components: a nonlinear elastic component representing the resistances to recoverable deformation mechanisms, and a non-linear inelastic component representing the resistances to irrecoverable deformation and texture evolution. Chapter 3 discusses the formulation of a constitutive relation for the elastic response of nonwoven fabrics. Specifically, we present an approach to incorporate fabric network structure into a continuum model via a tensorial representation (fabric ellipsoid) of morphological sources of network anisotropy. An orthotropic elastic constitutive model for the elastic response of nonwoven fabrics is then formulated based on this structural measure and deformation mechanisms of the network structure. Chapter 4 discusses an extension of the orthotropic elastic model to account for inelastic deformation mechanisms, particularly the irrecoverable evolution of the fabric structure. The inelastic formulation is prescribed in terms of an evolution law for the fabric ellipsoid. Chapter 5 demonstrates the predictive capability of the proposed fabric model by comparing model simulations under uniaxial tension and equibiaxial tension to the corresponding experimental data. The model sensitivity to the model parameters is also investigated. Chapter 6 summarizes the accomplishments of this work and discusses venues for further improvement.

Chapter 2

Experimental Characterizations of Nonwoven Fabrics

Nonwoven fabrics are sheet structures created by bonding or interlocking a web (network) of fibers through mechanical, thermal or chemical processes. In general, the mechanical response of nonwoven fabrics exhibits two major characteristics. First, the mechanical response can vary significantly when the fabric is loaded along different directions, depending on the existence of a preferential orientation in the fiber arrangement and/or in the pattern of inter-fiber bonding/entanglement. Second, the mechanisms of deformation include elastic and inelastic components, accompanied by an irrecoverable evolution of the texture of the fiber network.

This study focuses on the mechanical response of high performance ballistic nonwoven fabrics. Many of the commercially available ballistic nonwoven fabrics are in the form of needlepunched nonwoven felts, which are typically fabricated by entangling fibers of the same material. Therefore, the mechanical response of this class of materials is governed by the morphological properties of fiber web, such as fiber entanglement, fiber curl and fiber orientation, and the mechanical properties of constituent fibers. In this work, A web of high strength polyethelene fibers manufactured by DSM "Dyneema Fraglight" is selected as the representative material.

In this study, the investigation of the properties of Dyneema Fraglight is carried out in a two-step approach. First, the fabric structure is characterized in terms of its morphological

Properties	**Unit**	**Dyneema Fraglight**
Roll Width	cm	160
Areal Density	g/m^2	190-220

Table 2.1: Properties of Dyneema Fraglight provided by the manufacturers

properties and the mechanical behavior of individual constituent fibers using image analysis techniques and single-fiber tension test, respectively. Then, the fabric macroscopic response under in-plane modes of deformation is investigated. Attention is given to the evolution of the fabric structure with macroscopic deformation, and to damage mechanisms associated with fiber slip and fiber disentanglement. These experimental results serve as a guidance in model development, as well as validation for the proposed modeling formulation.

2.1 Characterization of fabric structure

Dyneema Fraglight is manufactured by needlepunching overlays of combed fiber mats and provided in rolls of 1.6m width. Table 2.1 shows the geometric properties of Dyneema Fraglight provided by the manufacturer. Note that the value of the fabric thickness was not provided by the manufacturer. By our measurement at different locations of the fabric roll, the fabric thickness falls in the range of 0.8 - 1.4 mm.

In order to establish a set of terminology for the directionality of this material, the direction along the fabric roll is termed "roll" (R) direction, and the direction perpendicular to the fabric roll is termed "cross" (C) direction. Upon inspection, the fabric appears to have marking lines on one side of the fabric surface at approximately 7mm interval along an angle of 30 degrees to the cross direction. These marking lines were created by the needle-punching machine along the directions of multiple needlepunch runs. In the following sections, the direction along the needlepunch run markings is termed needlepunch machine run, denoted by P-direction, and the direction orthogonal to the needlepunch machine run is termed X-direction. Figure 2-1 shows the schematic of the material directions.

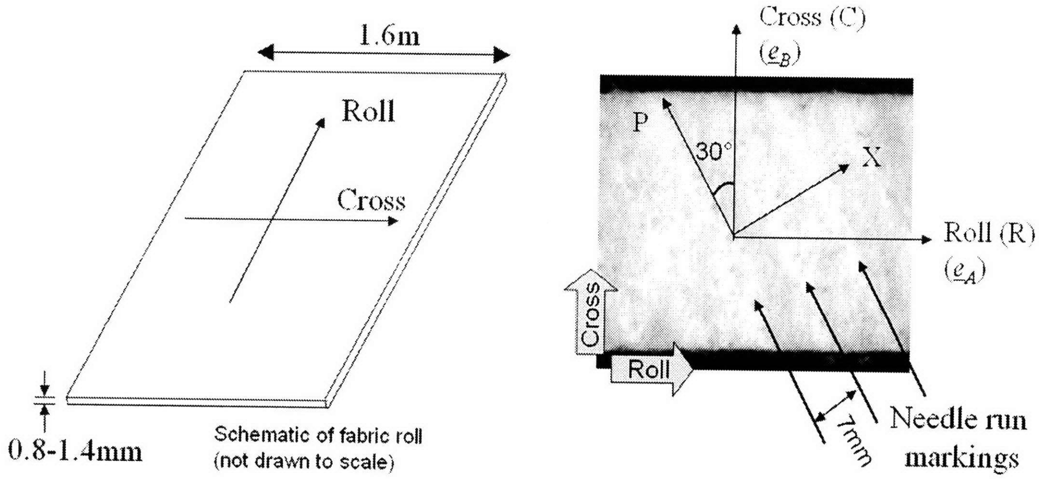

Figure 2-1: Schematic of material directions

2.1.1 Microstructural analysis

Following standard approaches, the microstructure of the fabric is analyzed by means of image analysis. Microstructural images are usually obtained by photographing the fabric with a digital camera (reflective or transmitted light source), or by using an optical microscope. Because of the highly reflective surface of this fabric, we determined that the images of this fabric were best obtained under a transmitted light source. Thirty micrographs of the Dyneema Fraglight were obtained at random locations on the fabric surface using a standard optical microscope. Selected samples of the micrographs of the fabric surface at the virgin state are illustrated in Figure 2-2. These images show that the Dyneema Fraglight is a web of curly self-entangled fibers with preferential alignments along the cross direction. In addition, the fibers appear to be preferentially aligned along the plane of the fabric.

In order to characterize the punch pattern resulting from the needlepunching process, another set of images of Dyneema Fraglight was taken at a larger length scale using a digital camera with a transmitted light source. Figure 2-3 shows that the punch pattern in Dyneema Fraglight is approximately random with weak bias along the needle run direction (P).

In the characterization of fabric structure we focus on determining two critical morphological

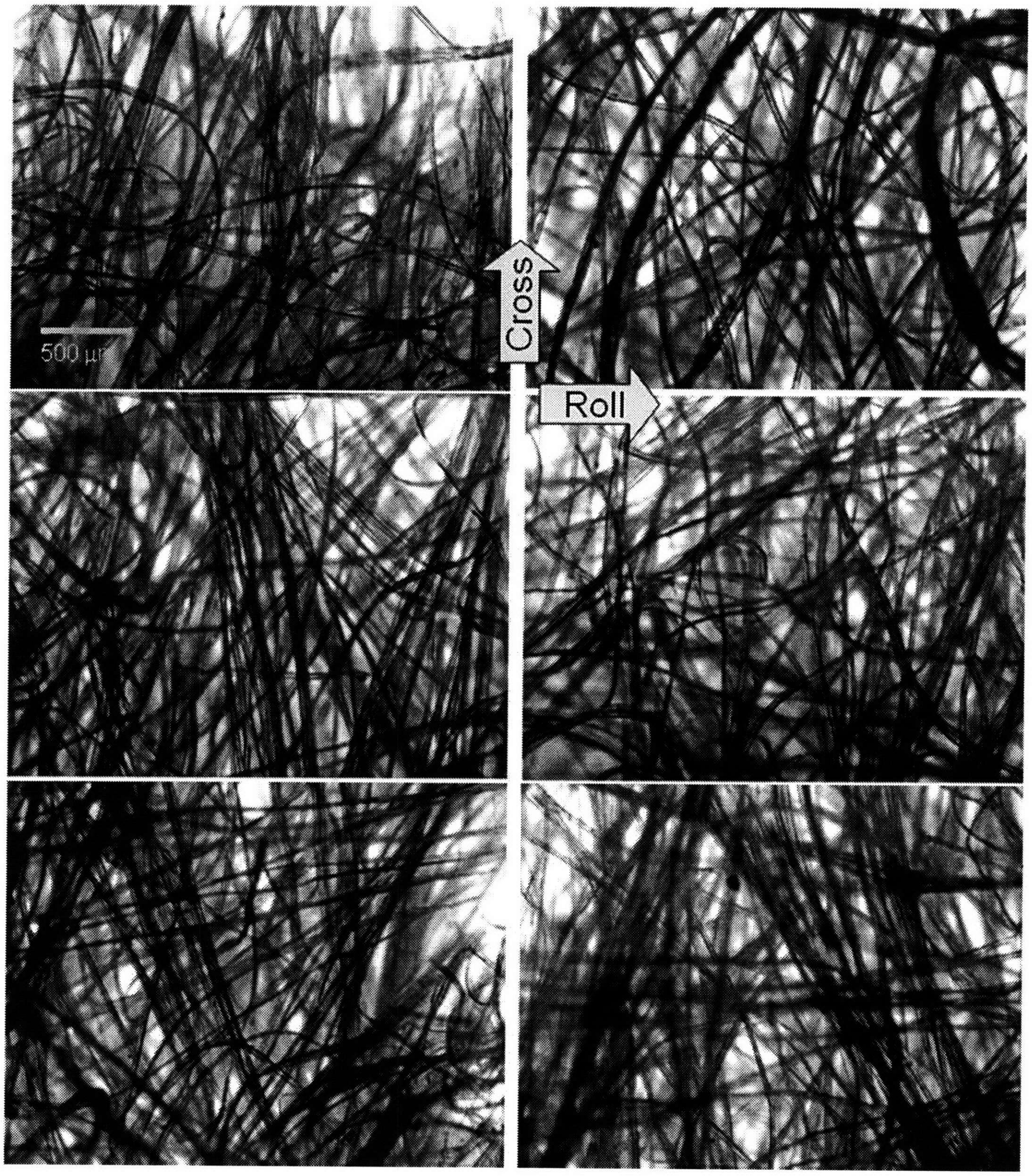

Figure 2-2: Images of Dyneema Fraglight taken from random locations of the fabric surface. The images were obtained using a standard microscope using transmitted light source.

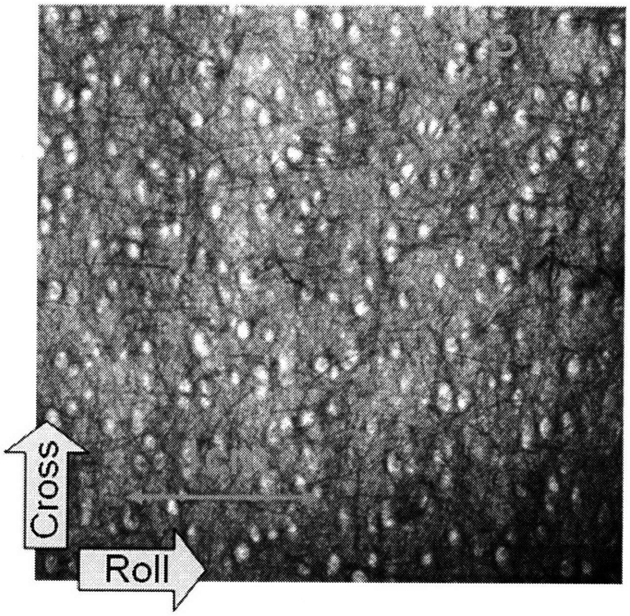

Figure 2-3: Random bonding pattern in Dyneema Fraglight

properties that are related to the anisotropy of the material response.

1) *Fiber orientation distribution (FOD)* – This distribution represents the normalized probability of having fibers aligned in each material direction, and gives rise to deformation resistance biased toward the directions of preferential fiber alignment. The FOD can be measured using various image analysis techniques, e.g., [64] [65] and [42]. In this work, we employed an algorithm based on the orientation of simple neighborhoods proposed by Jahne [42] to quantify the FOD of the Dyneema Fraglight. The algorithm was implemented in a Matlab code by Dimitrios Tzeranis from the So Bioinstrumentation Lab at MIT. In summary, the algorithm uses a numerical differentiation scheme to calculate the derivatives of the image intensity along x-y directions in the fabric plane . The derivatives from individual 15x15 pixel windows form a "structure tensor" in which the eigenvectors and eigenvalues represent the orientation of the fiber signal and its significance, respectively. This algorithm was used to analyze the fiber orientation distribution from micrographs at the scale represented in Figure 2-2. Three analyses were performed on 10 randomly selected images from the set of 30 micrographs. The analysis results are plotted together with the averaged FOD of all 30 micrographs in Figure 2-4. It is

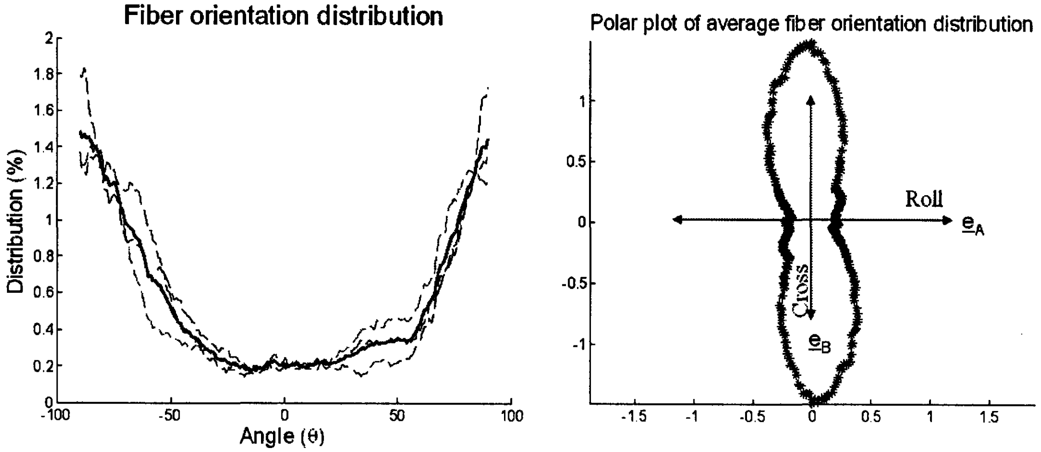

Figure 2-4: A histogram of the fiber orientation distribution for Dyneema Fraglight obtained from averaging 3 sets of 10 random images (dash lines) and 30 images (solid line) (left) and the polar plot of the averaged FOD of 30 images (right)

clear from Figure 2-4 that the average FOD for 10 micrographs are consistent with the average FOD for 30 micrographs. Therefore, the averaged FOD of randomly selected images constitutes a sufficient representation of the FOD of the fabric. When represented as a polar plot, the averaged FOD can be approximated to the second-order accuracy by an elliptical distribution. The ellipse fit of the FOD can be obtained using the following procedure.

Consider the general quadratic equation of an ellipse with the center at the origin:

$$ax^2 + 2bxy + cy^2 + f = 0, \tag{2.1}$$

where x and y are expressed in the Cartesian coordinate system $\underline{e}_A - \underline{e}_B$, and are related to the fiber distribution $m(\theta)$ and the orientation angle θ, by

$$x = m(\theta)\cos(\theta), \tag{2.2a}$$

$$y = m(\theta)\sin(\theta). \tag{2.2b}$$

Equation 2.1 represents an ellipse when $b^2 < 4ac$. By using the ellipse fitting algorithm by Fitzgibbon et al. [29] on the FOD histogram, the coefficients of the best-fitted ellipse are given by $a = 1.0000, b = 0.0694, c = 0.0461$ and $f = -1.8504e - 006$. A non-zero b indicates that the FOD ellipse is slightly rotated due to misalignment in the image acquisition stage (e.g., misalignment of the fabric sample or the camera). The ellipse equation 2.1 can also be cast in terms of a structural tensor $\underline{M}$, and the vector $\underline{m} = x\underline{e}_A + y\underline{e}_B$ by the following relation [37]:

$$1 = \underline{m}^T\left(\underline{M}\underline{m}\right) = -\frac{1}{f}\begin{bmatrix} x & y \end{bmatrix}\left(\begin{bmatrix} a & b \\ b & c \end{bmatrix}\begin{bmatrix} x \\ y \end{bmatrix}\right). \tag{2.3}$$

Although the measured structural tensor $\underline{M}$ is derived from the ellipse equation, the coefficients a, b and c *do not* represent the semiaxes of the ellipse, and therefore $\underline{M}$ is not the proper representation of the ellipse distribution [1]. The measured structural tensor $\underline{M}$ is called "inverse ellipsoid" by Zysset [81], because the magnitudes of $\underline{M}$ is inversely related to the orientation distribution.

The measured structural tensor $\underline{M}$ can be transformed so that it represents the FOD distribution using the following steps. First, consider the tensor $\underline{M}$ in the principal frame so that $\underline{M} = \sum_{i=1,2} M_i \underline{e}_i^M \otimes \underline{e}_i^M$, and M_i and $\underline{e}_i^M$ represent the eigenvalue and eigenvector of $\underline{M}$ in the direction i, respectively. In the principal frame, 2.3 becomes

$$\tilde{\underline{m}}\left(\underline{M}\tilde{\underline{m}}\right) = \begin{bmatrix} x^M & y^M \end{bmatrix}\left(\begin{bmatrix} M_1 & 0 \\ 0 & M_2 \end{bmatrix}\begin{bmatrix} x^M \\ y^M \end{bmatrix}\right) \tag{2.4}$$

$$= M_1 x^2 + M_2 y^2 = 1 \tag{2.5}$$

where $\tilde{\underline{m}} = x^M \underline{e}_1^M + y^M \underline{e}_2^M$. Equation 2.4 represents the ellipse equation when the axes are aligned along $\underline{e}_1^M$ and $\underline{e}_2^M$. 2.4 can also be written as

$$\frac{x^2}{\left(\frac{1}{\sqrt{M_1}}\right)^2} + \frac{y^2}{\left(\frac{1}{\sqrt{M_2}}\right)^2} = 1, \tag{2.6}$$

where $\frac{1}{\sqrt{M_1}}$ and $\frac{1}{\sqrt{M_2}}$ represent the semiaxes of the ellipse. Hence, the FOD ellipse can be

---

[1] Consider, for example, the components of $\underline{M}$ along the $\underline{e}_A$ and $\underline{e}_B$ directions. From the parameters a and b of the best-fitted ellipse equation, $a > b$, suggesting that there are more fibers along $\underline{e}_A$ than along $\underline{e}_B$, but Figure 2-4 suggests otherwise.

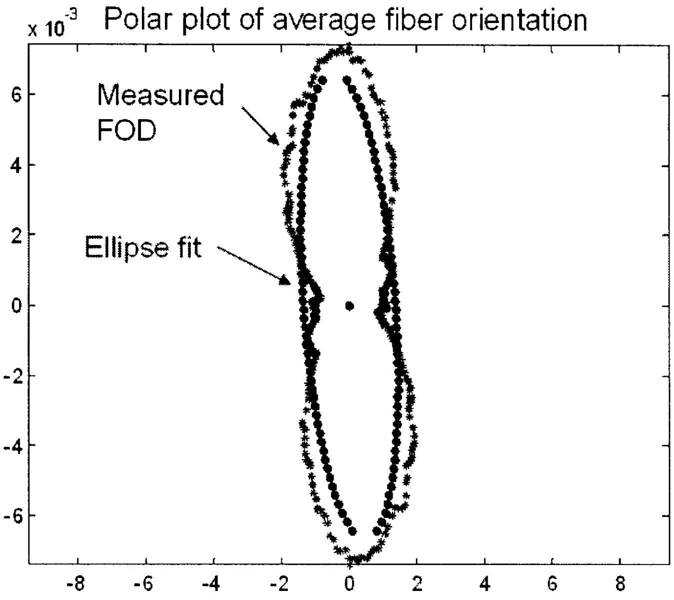

Figure 2-5: Ellipse fit of the measured FOD.

represented by a structural tensor $\underline{W}$ in the following form:

$$\underline{W} = \begin{bmatrix} \frac{1}{\sqrt{M_1}} & 0 \\ 0 & \frac{1}{\sqrt{M_2}} \end{bmatrix}. \tag{2.7}$$

The ellipse fit of the FOD with the structural tensor $\underline{W} = 0.0014 \begin{bmatrix} 1.0 & 0 \\ 0 & 5 \end{bmatrix}$ is shown in Figure 2-5.

2) *Orientation distribution of junction-to-junction distance (JJD)*[2] – the normalized distance between two junctions in each material direction. This distribution is related to the anisotropy of the extensibility limits of the network, and gives rise to stress contributions that are biased in the directions of long junction-to-junction distances. The junctions of distributed fiber networks can be further categorized into two broad classes based on the mechanisms by which junctions are created: patterned junctions created by controlled bonding processes, and random

---

[2] In this work, 'junctions' are defined by the spatial positions where two or more fibers are inter-connected by thermal or chemical bonding processes or, in the case of Dyneema Fraglight, by physical entanglements created by the needlepunching process

junctions created by random bonding process (e.g., thermal bonding of quasi-melted fibers in electrospinning or random entanglements created by needlepunching of fiber webs). The JJD of distributed networks with patterned junctions can be directly measured from the images of the network structure. On the other hand, the JJD of distributed networks with random junctions cannot be easily measured by the currently available image analysis techniques. However, the JJD of distributed networks with random junctions can be related to the FOD of the network because the locations of inter-fiber junctions are statistically biased by the number of fiber intersections, which is related to the fiber orientation distribution.

A relationship between the JJD and the FOD of a network with random bonding process can be obtained using the simplified straight fiber model described in Appendix A. Basically, this model assumes that a distributed fiber network can be represented by a three-dimensional network of straight cylindrical inter-penetrable fibers arranged in a spherical window according to a prescribed fiber orientation distribution. By tracking the locations of the inter-fiber intersections, and by relating the average inter-fiber intersection distance to the fiber orientation, the model can provide an approximated relationship between the fiber orientation distribution and the distribution of the inter-fiber intersections. Because in a network with random bonding pattern, the junction density of the network directly scales with the intersection density, this simplified straight-fiber model can be used to obtain an approximate relationship between FOD and JJD as well.

As noted in Figure 2-3, the bonding (punch) pattern of the Dyneema Fraglight is approximately random. Therefore, the JJD of this fabric can be obtained from the measured FOD of the fabric using the simplified straight fiber model. The measured in-plane FOD was represented as a two-dimensional (ellipse) distribution. However, to apply the approach described in Appendix A, a fully three-dimensional representation of the FOD is needed, with a 3D ellipsoid replacing the 2D ellipse. Consistently with microstructural observations (and the manufacturing process), we assume a low density of fibers arranged in a direction normal to the plane of the fabric. This condition can be expressed in terms of a representation on the semiaxes of the ellipsoid, where the out-of-plane semiaxis is taken to be less or equal to the smallest in-plane semiaxis of the 2D FOD ellipse. By varying the value of the out-of-plane component and fixing the ratio of the in-plane components of the FOD ellipsoid, an appropriate ratio for the in-plane

Input FOD Ellipsoid[4]			Output JJD Ellipsoid			
W_{AA}	W_{BB}	W_{CC}	G_{AA}	G_{BB}	G_{CC}	G_{BB}/G_{AA}
1	5	1	0.7985	1.4024	0.7985	1.7562
1	5	0.8	0.7820	1.4516	0.7662	1.8561
1	5	0.7	0.7615	1.5027	0.7357	1.9733
1	5	0.5	0.7441	1.5514	0.7044	2.0848
1	5	0.3	0.7071	1.6455	0.6472	2.3269
1	5	0.1	0.6550	1.7635	0.5814	2.6922
1	5	0.01	0.6438	1.7893	0.5668	2.7793
1	5	0.001	0.6286	1.8171	0.5541	2.8904

Table 2.2: Approximated values of the JJD ellipsoid from the measured FOD ellipse. All simulations were done using n=2000 and d=2

components of the JJD ellipsoid can be inferred (Appendix A). Table 2.2 provides a list of different ratios between the semiaxis of the JJD ellipsoid obtained from the simplified straight fiber model, with different values of the out-of-plane FOD component and a constant ratio of the in-plane components of the FOD ellipsoid[3].

According to Table 2.2, the ratio of the in-plane components of the JJD ellipsoid $\frac{G_{AA}}{G_{BB}}$ should fall between 1.7 to 3. These approximated values of the JJD ellipsoid will be used for model validation in Chapter 5.

2.1.2 Tensile response of individual fibers

The mechanical response of constituent fibers is investigated as a means to gain a better understanding of the macroscopic response of the fabrics under tensile loading, particularly in the large strain regime. To test the fibers of a needlepunched nonwoven fabric, a bundle of fibers is pulled out of the fabric using tweezers, and the damaged fibers displaying defects such as kinks or frays are removed. An individual fiber is isolated from the bundle, looped around a small, thin rod, such as a staple or paper clip, and bonded to the rod by a drop of 5-minute epoxy. The assembly of fibers and rod is then glued to a paper coupon cut into 40 by 20 mm with a center slot of 20 by 10 mm, creating a coupon specimen with approximately 20 mm initial gauge length. Figure 2-6 shows a coupon specimen of Dyneema Fraglight fiber. The coupon

---

[3] The accuracy of the relationship between FOD and JJD relation decreases as the network becomes highly anisotropic due to numerical instability in the simplified network model

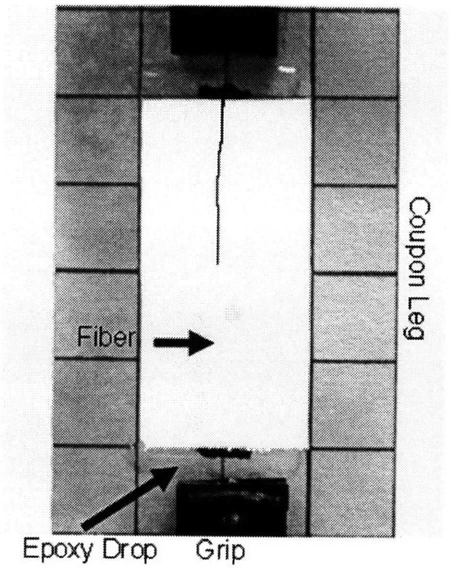

Figure 2-6: Fiber coupon specimen (half of fiber highlighted for clarity)

specimens can be gripped directly on any jaw inserts of regular tensile testing machine. In this study, the Dyneema fibers were tested using a Zwick tensile tester model BTC-FR010TH.A50. After gripping the coupon in the testing machine, the coupon lateral legs are cut prior to each test so that the fiber carries the entire applied load. A preload of approximately one millinewton was applied to the fiber before each test to eliminate kinks and slacks on the fibers. Ten tests were performed at a nominal strain rate of 0.01 s^{-1}. The test results for the Dyneema Fraglight fibers shown in Figure 2-7, suggest the presence of two families of fibers with different stiffnesses.

A study of individual Dyneema® fibers under a microscope reveals that the fibers contain many defects including bulges, kinks, splits and fray. Observations of a number of fiber images suggest that there are two main populations of fibers: one population is a cylindrical shape fiber with a diameter of 20 microns; the fibers in the second population are composed of two joined 10 microns fibers as illustrated in Figure 2-8. This observation provides an interpretation for the two stiffness levels observed in the load-strain plots of tensile tests (Figure 2-7). The average tensile properties of the individual fibers are calculated as shown in Table 2.3.

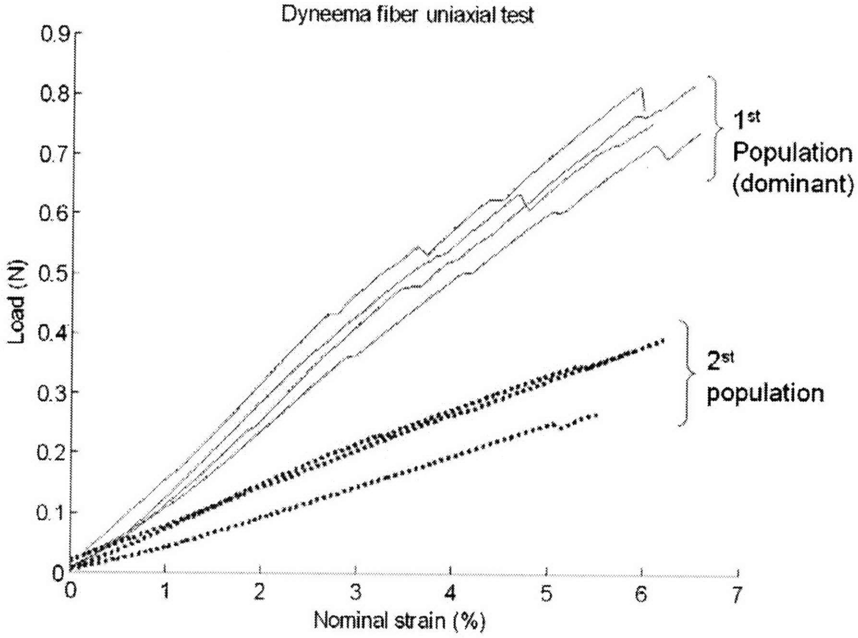

Figure 2-7: Tensile test results of Dyneema Fiber

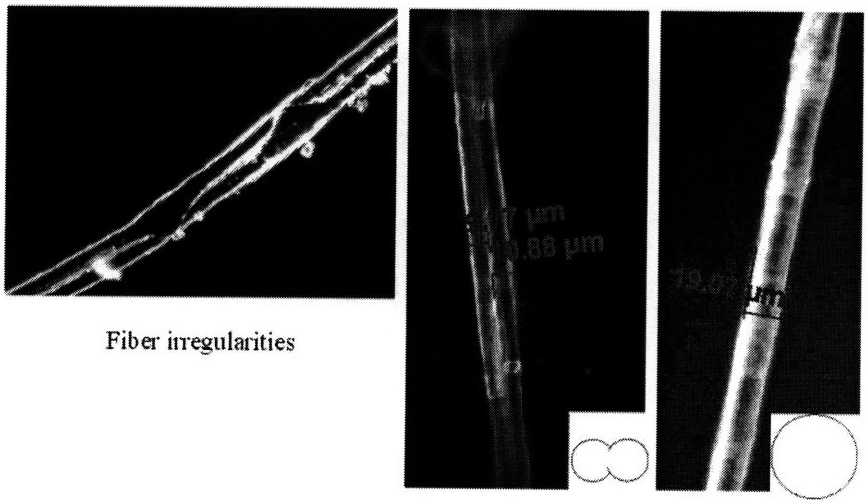

Figure 2-8: Images of fiber irregularities and two populations found in Dyneema fibers

Properties	**Unit**	**Dyneema Fiber**
Diameter	μm	10-20
Young's Modulus	GPa	32
Strength	MPa	2000
Elongation at Break	%	6.0

Table 2.3: Mechanical properties of Dyneema fibers measured from the experiments

2.2 Macroscopic mechanical response of nonwoven fabric

The primary use of Dyneema Fraglight is in ballistic (fragment) protection applications, where the membrane response of the fabric is of critical relevance. As a preliminary step in understanding the fabric behavior, attention is given to the fabric response under in-plane tensile-dominated modes of deformation. In this work, the governing deformation mechanisms of the fabric under tensile loads are identified using two types of mechanical testings: uniaxial tensile tests and equibiaxial stretch tests. The results of these experiments serve as guidance in the development of a microstructurally-based continuum model for nonwoven fabrics, as well as validating cases for the proposed formulation.

2.2.1 Fabric macroscopic response under uniaxial tensile loading

A number of standard techniques have been established in the literature to test nonwoven fabrics under tensile loads. Examples of these are a grab test of narrow-width specimen (ASTM D1682-64), and a grab test of wide-width specimen (ASTM D4595-86). According to the ASTM D5034-95, the standard grab test is only applicable when the total fabric deformation is less than 11% nominal strain. However, the Dyneema Fraglight has been reported by Chocron [23] to undergo uniaxial deformation more than 100% strain before failure, and therefore, the standard tensile testing methods are at least not suitable for characterizing the large strain response of this fabric. In this study, a new technique that allows the measurement of fabric deformation at large strains is proposed as described below.

First, the fabric is cut into dogbone-shape strips as illustrated in Figure 2-9. This specimen shape ensures that the central region of the specimen is subjected to a uniform uniaxial stress state for all levels of deformation. A new set of custom made grips was fabricated to perform the fabric tensile strip tests, see Figure 2-9. By wrapping the sample around a small bar which

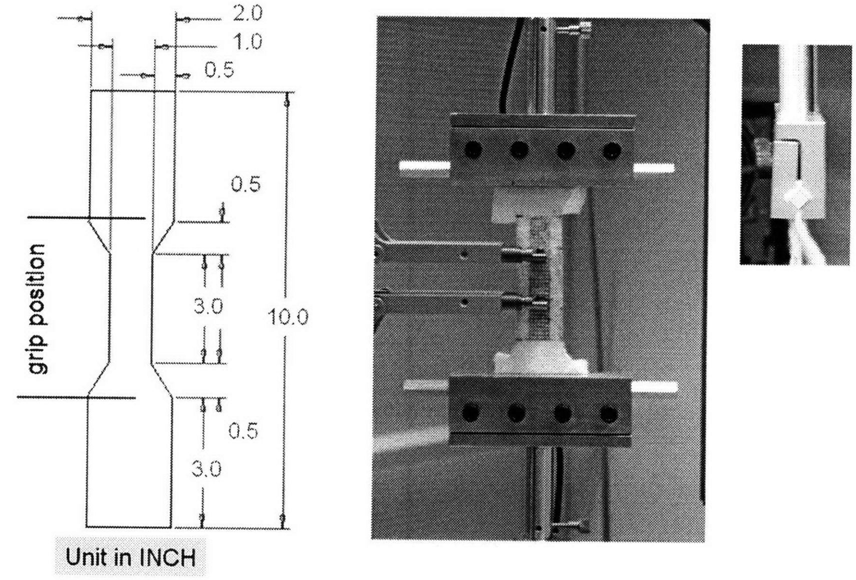

Figure 2-9: Dogbone specimen (left) and custom designed fabric fixture – front view (middle) and side view (right). Each end of the fabric strip is wrapped around a bar, and then clamped between two grooved jaws of the fixture. A contact extensometer is used in this configuration

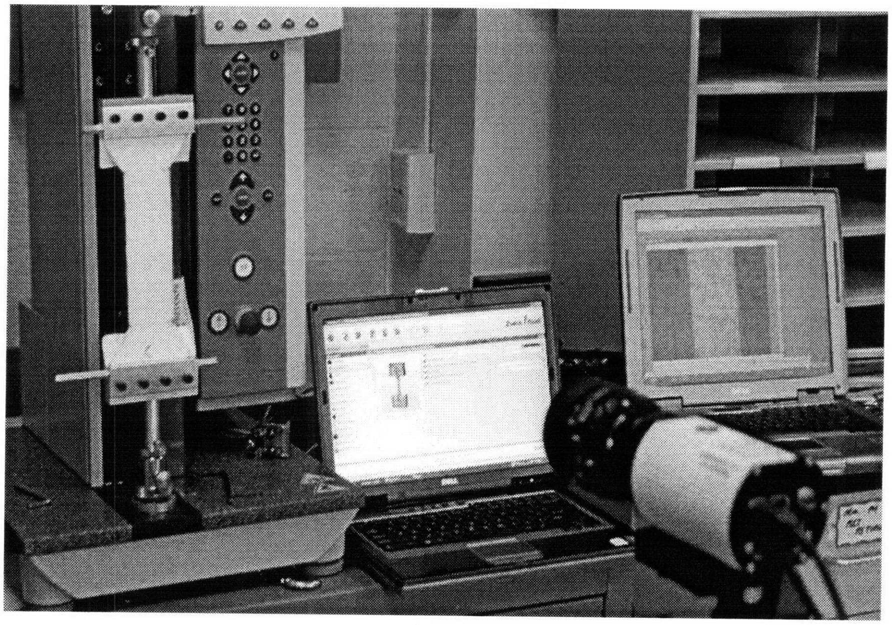

Figure 2-10: Tensile test configuration

fits in a groove between the jaws inserts, the fabric strip is prevented from slipping out of the jaws. The clamping edges define the fabric initial gauge length. In its initial unloaded, gripped configuration, the specimen has a total length of 4 inches; 3 inches of this length is in the constant narrow width region. The displacement is measured by a contact extensometer with an initial gauge length of one inch positioned in the central region of the specimen as shown in Figure 2-9 (middle and right). All tests were carried out on the same tensile tester as in the single fiber tests, but with a load cell with a larger load limit. Figure 2-9 shows a typical uniaxial tensile test configuration. Figure 2-10 shows an alternative testing configuration where the deformation of the specimen is monitored by digital imaging techniques.

Three types of uniaxial loading tests were conducted on the fabric strips using the dogbone configuration: monotonic loading test, cyclic loading test, and two-step monotonic loading test. The **monotonic loading** test provides a means to measure the fabric tensile properties, to determine the fabric anisotropy, as well as to identify the deformation mechanisms of the fabric under tensile loads. To investigate the effects of fabric anisotropy, the uniaxial monotonic loading tests were conducted along the principal directions of the fiber orientation, or the roll

(R) and the cross (C) directions. Additional tests were conducted along the P- and the X-directions to identify the effects of the needlerun markings. All tests were performed at a nominal strain rate of 0.01 s^{-1} until failure.

The **cyclic loading test** was conducted to gain further insight into the inelastic mechanisms of deformation, and texture evolution due to irrecoverable reorientation of the fibers. The cyclic loading test is a displacement controlled test with a series of loading-unloading sequences, each following the pattern described below:

1) Load - the specimen is pulled up to a pre-specified strain,

2) 1st Hold - the specimen is held at the pre-specified strain for a short interval

3) Unload - the strain on the specimen is decreased to reach a condition of zero load

4) 2nd Hold - the specimen is held at this lower strain for a short interval

The cycle continues with higher values of pre-specified loading strains until the specimen fails. Figure 2-11 shows the schematic of the nominal strain history for the uniaxial tensile cyclic loading test. To closely approximate a true strain rate response of the fabrics, the test speed is varied between the cycles, and is calculated so as to obtain the same constant nominal strain rate with respect to the specimen length at the beginning of the loading step. For example, if the desired true strain rate is 0.01 s^{-1} and the specimen length at the beginning of the third cycle is 5 mm, the test speed of that particular cycle is 0.05mm s^{-1}.

The two-step monotonic loading test is used primarily to quantify the degree at which the fabric texture has evolved under monotonic loadings. The **two-step loading test** is a series of two uniaxial monotonic loading tests with the following loading protocol. In the first step, a fabric specimen four times larger than the regular uniaxial tensile specimen in Figure 2-9 is uniaxially stretched to a pre-specified strain that is well below the onset of fabric failure. After the specimen is completely unloaded, a set of fabric specimens with the same aspect ratio but only half the size of regular specimens, are cut from the center region of the large specimen orthogonal to the first loading direction. In the second step, the smaller specimens are tested under monotonic uniaxial tension until failure. Figure 2-12 shows a schematic of the two-step uniaxial tension test protocol.

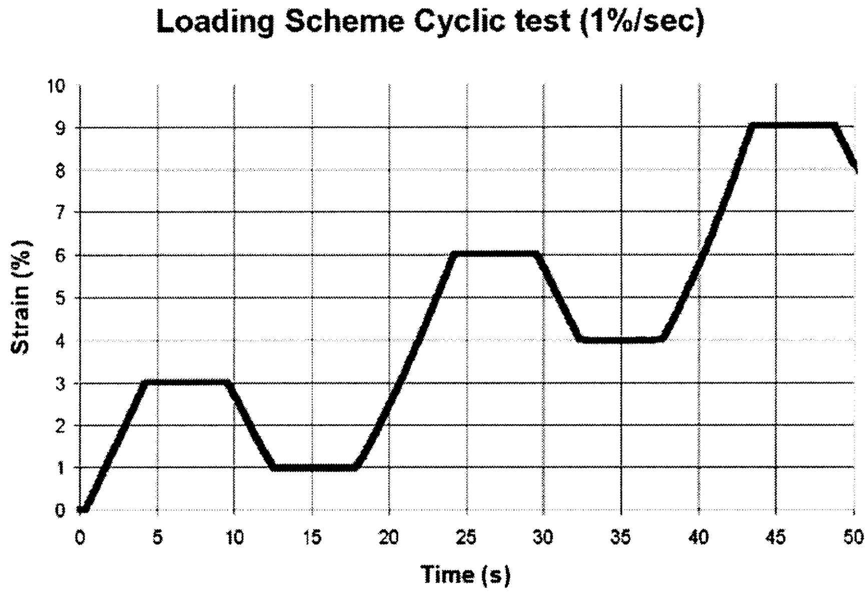

Figure 2-11: Loading schematic of uniaxial cyclic loading test

Fabric response under monotonic uniaxial loadings

Results of the fabric response under monotonic uniaxial loadings along the R,C,P, and X directions are plotted in terms of load per unit specimen width and nominal strain in Figure 2-13. Dyneema Fraglight exhibits a highly anisotropic nonlinear response under uniaxial tensile loads. The fabric response along the cross direction presents the highest stiffness with the shortest elongation at break, and further deviation from the cross direction results in a decrease in stiffness and an increase in elongation at break.

Similarity in the quantitative behaviors in different fabric directions implies that the fabric undergoes similar deformation mechanisms under uniaxial tension. In the initial compliant region of the load-strain plot, macroscopic deformation is primarily accommodated by realignment of constituent fibers. As the strain increases, the fibers realign along the loading direction resulting in a contraction of the specimen along the transverse direction. The fibers realignment continues until the fibers are uncurled and densely compacted. At this point, further deformation can only be accommodated by fiber stretching and fiber slipping out of the junctions (termed junction unraveling). As the deformation progresses, fiber slippage out of the junc-

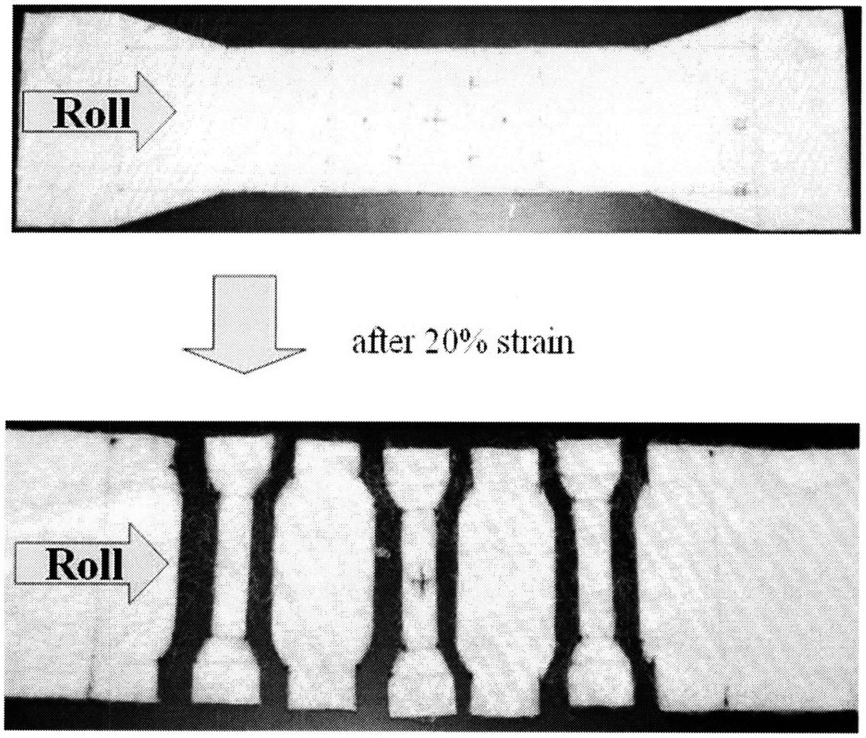

Figure 2-12: Schematic of two-step uniaxial tensile loading test: (top) the specimen for the first loading step, and (bottom) the specimens for the second loading step

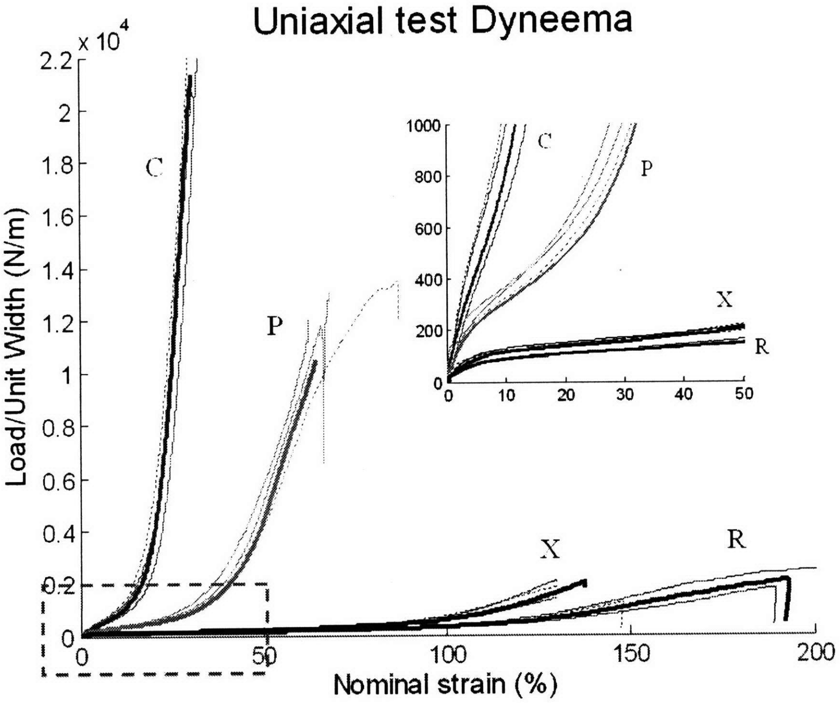

Figure 2-13: Uniaxial tensile responses of Dyneema Fraglight in different loading directions (C-cross, R-roll, P-needlepunch run, and X-orthogonal to the needlepunch run)

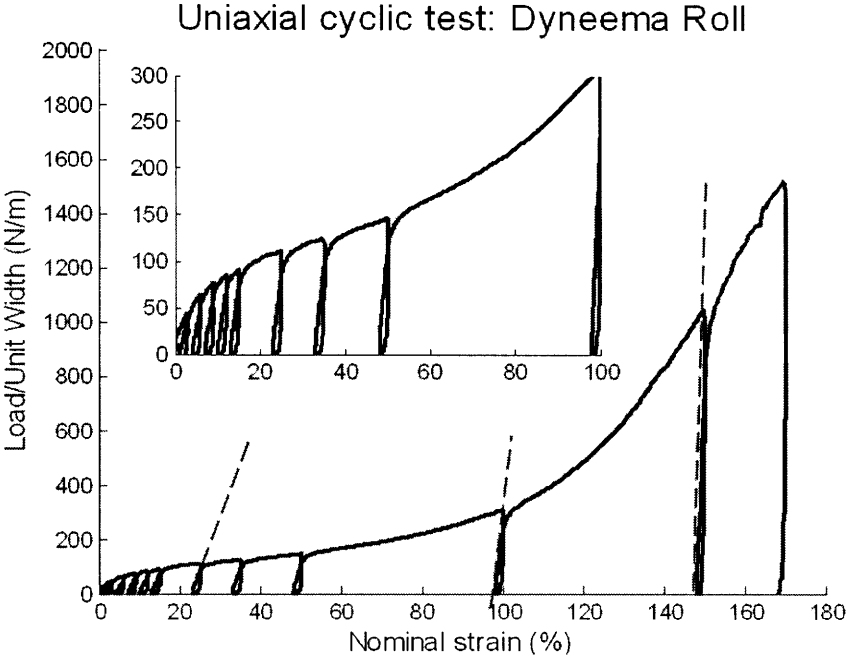

Figure 2-14: Uniaxial tensile test result for the roll direction of Dyneema Fraglight

tions dominates other deformation mechanisms. The sample eventually fails by a combination of junction unraveling and fiber failure.

The results in Figure 2-13 are consistent with the microstructural analysis of the fabric texture in Figure 2-4. Because most of the fibers are already aligned along the cross direction, the response of the fabric along this direction is very stiff because the deformation is accommodated by fiber stretch and junction unraveling. On the other hand, the fabric response along the roll direction is mostly accommodated by fiber re-orientation because the fibers are initially aligned orthogonal to the loading direction. Because the resistance to fiber re-orientation is lower than the resistance to fiber stretch and fiber slippage, the fabric response along the roll direction is much more compliant than the fabric response along the cross direction.

Fabric response under cyclic uniaxial loadings

Typical results of the cyclic loading tests are shown in Figure 2-14 for the roll direction of Dyneema Fraglight, and Figure 2-15 for the cross direction. These results suggest that the

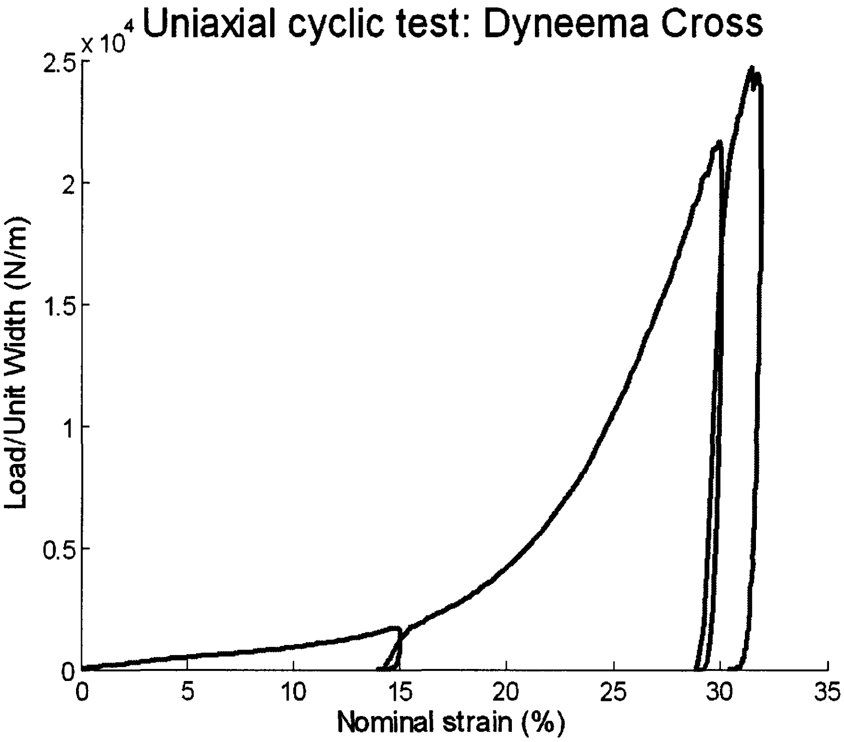

Figure 2-15: Uniaxial tensile test result for the cross direction of Dyneema Fraglight

deformation of the fabric is mostly accommodated by inelastic mechanisms, as illustrated by a small elastic recovery at each load-unload cycle. In addition, the stiffness in each successive loop appears to be increasing as more fibers are aligned along the loading direction. The fiber-level deformation mechanisms corresponding to different stages of the cycle for the roll direction are illustrated in Figure 2-16. In the loading step, the fabric first undergoes an elastic extension accommodated primarily by stretching of the fiber network (image C). Once a sufficient stress level is reached, fiber realignment become the dominant deformation mechanism, with a marked decrease in stiffness (image D). When the fabric deformation reaches the target strain, the fabric is held at constant stretch for a short period over which the stress relaxes by means of fibers slip and realignment. When the fabric is unloaded, the elastic component of deformation is recovered. As indicated by the graph, the magnitude of the load in the reloading step is usually lower than that in the loading step at the same strain, mainly due to the inelastic deformations accumulated over the hold period.

Fabric response under two-step monotonic loadings

The fabric response under the two-step monotonic loading is similar to the uniaxial monotonic tensile loading since the material undergoes the same type of deformation mechanisms. Figure 2-17 shows the results of 2-step monotonic loading tests for three cases of fabric conditions: (1) a virgin fabric loaded along the roll direction (1st step Roll), (2) a virgin fabric loaded along the cross direction (1st step Cross), and (3) a deformed fabric after 20% strain in the roll direction, loaded along the cross direction (2nd step Cross). The plots are presented in terms of normalized load per unit specimen width versus nominal strain to facilitate comparison among the three cases. The response in the second step test appears to be more compliant than the one of the virgin fabric loaded along the cross direction. This result suggests that the fabric texture has evolved in the course of the first load-unload step, and has become less biased along the cross direction.

The fiber orientation distribution of the fabric texture after the 1st step can be analyzed using the same approach as described in Section 2.1.1. Figure 2-18 shows the fiber orientation distribution after the first load-unload step. As expected, the fiber orientation has become less biased along the cross direction due to the 20% stretch along the roll direction. Table 2.4

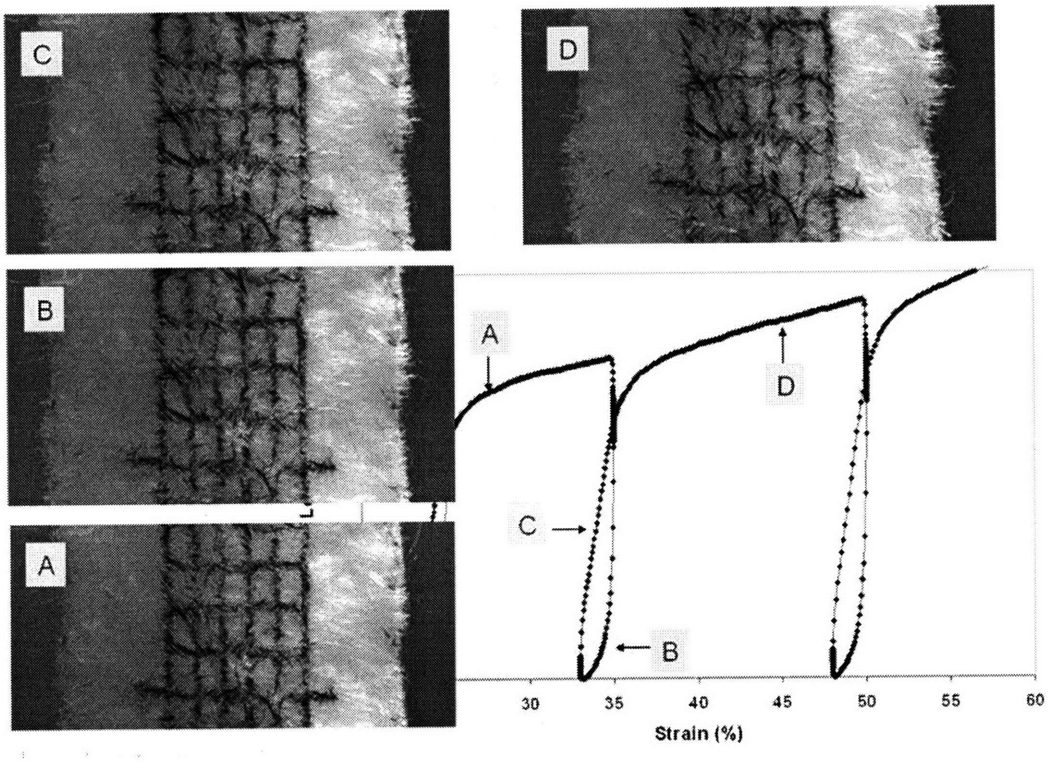

Figure 2-16: Inelastic deformation mechanisms in uniaxial cyclic loading of needlepunched nonwoven fabrics

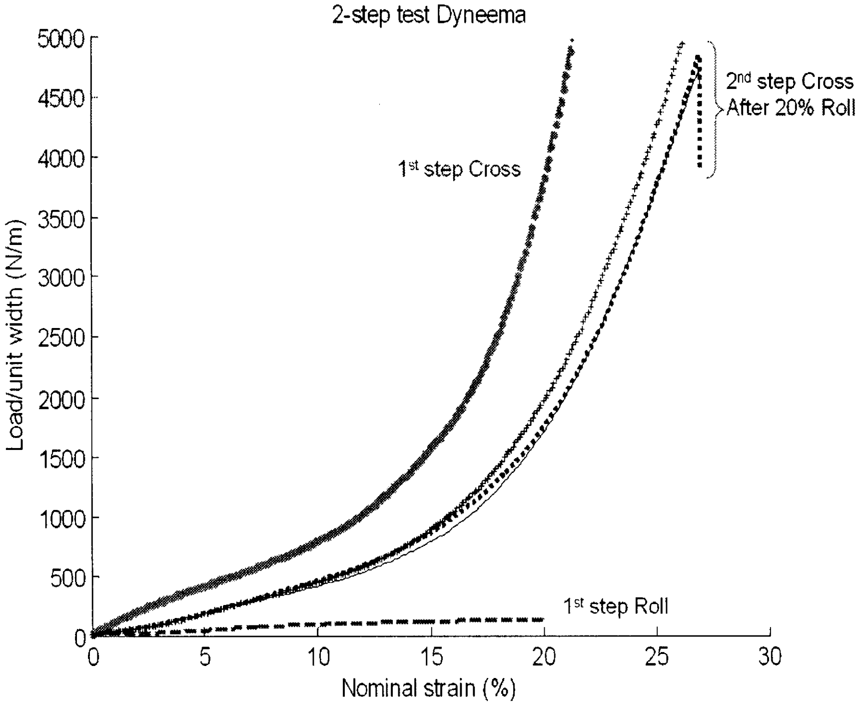

Figure 2-17: Results of 2-step uniaxial monotonic loading tests

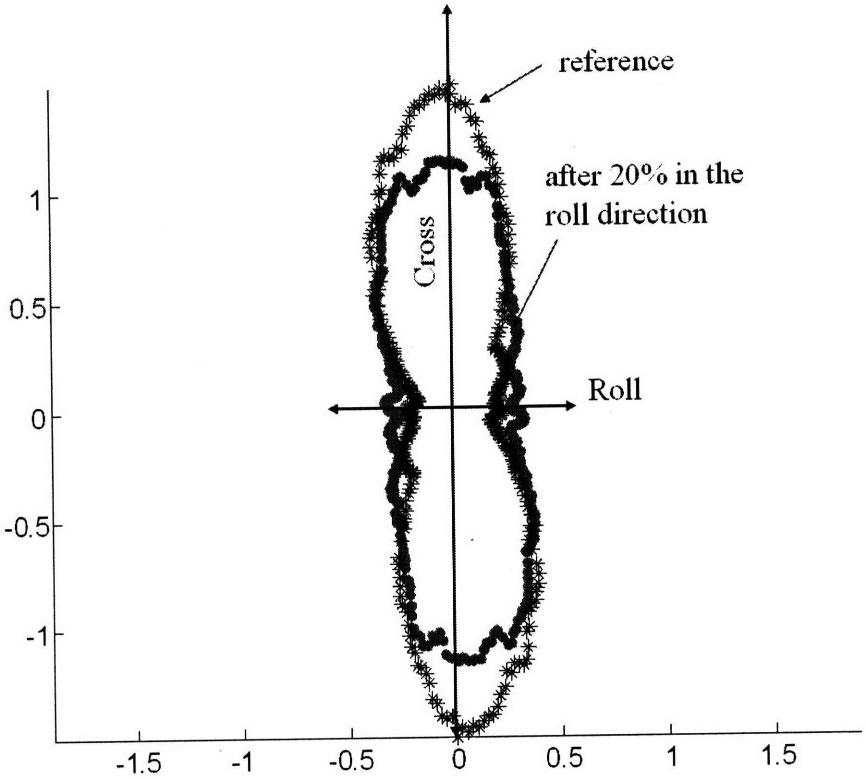

Figure 2-18: Evolution of the fiber orientation distribution after 20% strain in the roll direction

shows the change in the measured FOD tensor and the approximated JJD obtained from the simplified straight fiber model. These data will be used for a model validation in Chapter 5.

2.2.2 Fabric macroscopic response under biaxial tensile loading

The Dyneema Fraglight fabric was tested under biaxial tensile loadings in order to gain additional insight into the evolution of the fabric network structure. In this test, fabric specimens of cruciform shape shown in Figure 2-19 were loaded at a constant displacement rate of 10mm

	Measured FOD (W_{AA}:W_{BB})	JJD from SSF^{5}model (G_{AA}:G_{BB})
Undeformed	1:5	1:1.9733
after 20% Roll	1:3.9265	1:1.6897

Table 2.4: Reference and deformed FOD and the corresponding JJDs

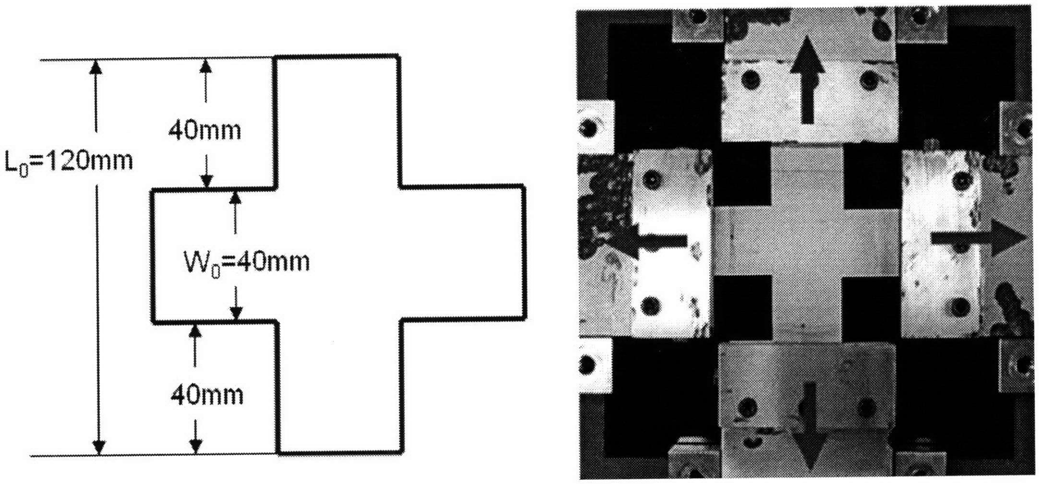

Figure 2-19: dimensions of biaxial test specimens and biaxial tensile test configuration

per second along the orthogonal principal directions of the fabric (i.e. R and C). The test configuration of the biaxial tensile test is illustrated in Figure 2-19. An optical extensometer system is used to observe the deformation mechanisms of the fabric structure. With simultaneous orthogonal loadings, the biaxial test specimen undergoes a complex deformation pattern due to the combination of two uniaxial tensile loads along the cruciform legs, resulting in a complex tensile-shear deformation (as a result of superposition) at the center of the cruciform specimen.

Figure 2-20 shows the macroscopic response of Dyneema Fraglight fabric under biaxial loading plotted in terms of load and machine crosshead displacement. The response indicates a highly anisotropic response where the stiffness along the cross direction is significantly higher than that along the roll direction. Images of the biaxial specimen at different stages of deformation in Figure 2-21 demonstrate a biased evolution of the fabric texture with fibers at the center of cruciform specimen reoriented toward the cross (stiff) direction. Fabric tear by means of fiber slippage and bond breakage is also observable along the boundary of the compliant cruciform leg and the center of the cruciform specimen. The result of this test indicates that the dominating deformation mechanism in this material is the irrecoverable reorientation of fabric texture.

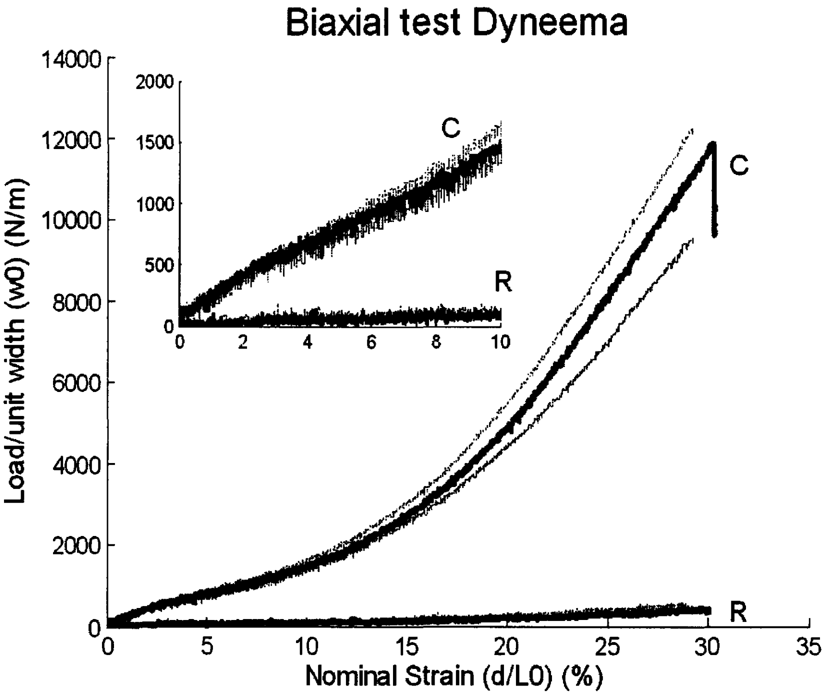

Figure 2-20: Equibiaxial stretch response of Dyneema Fraglight

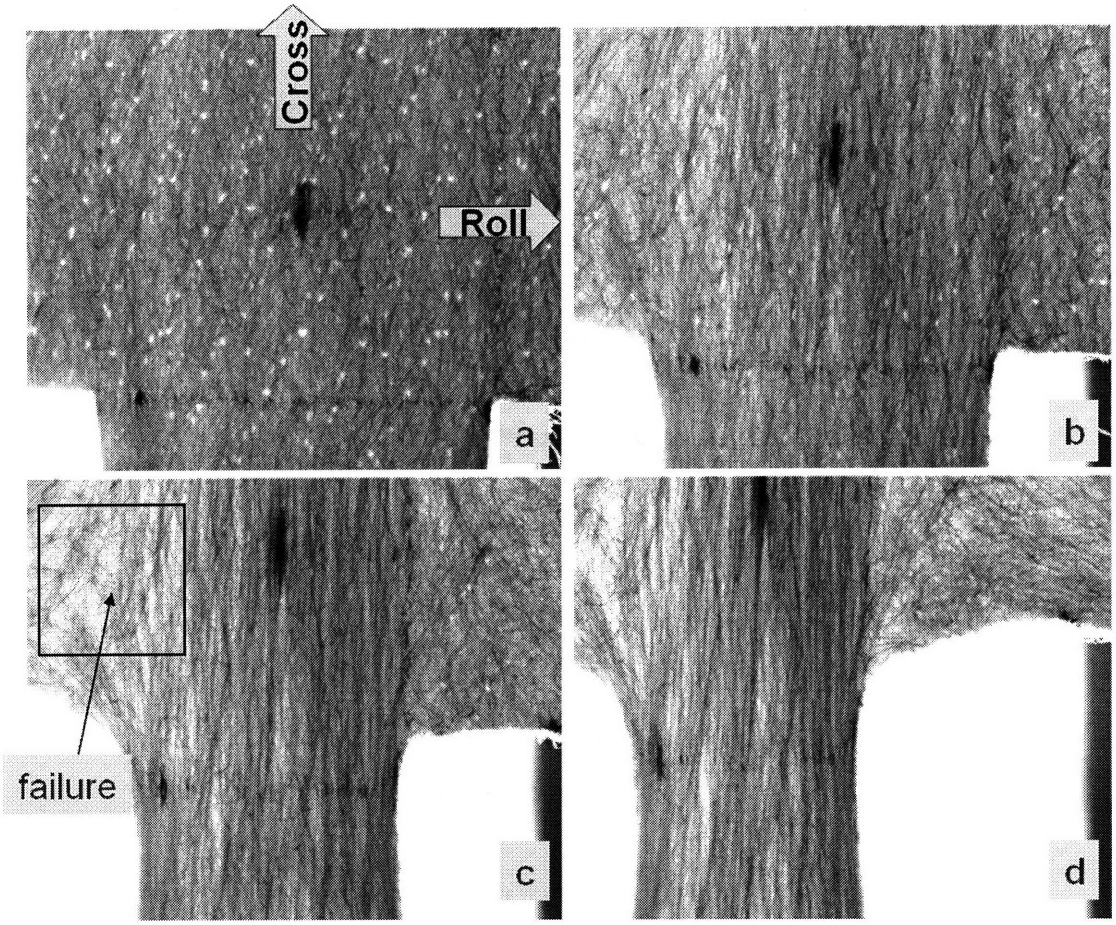

Figure 2-21: Deformed structures of Dyneema Fraglight under equibiaxial stretch with crosshead displacement of (a) 0 mm (reference) (b) 10 mm (c) 20 mm and (d) 30 mm

2.3 Chapter summary

This chapter reviewed our investigation of the morphological properties and the in-plane mechanical response of Dyneema Fraglight fabric. Characterization of the fabric microstructure indicates that Dyneema Fraglight is a web of curly fibers preferentially oriented along the cross direction, and aligned within the plane of the fabric. The investigation on the morphological sources of fabric anisotropy focused on the characterization and quantification of the fiber orientation distribution and junction-to-junction distance distribution.

Uniaxial tensile testing of the fabric reveals that Dyneema Fraglight exhibits an anisotropic response with the cross direction stronger and stiffer than the roll direction, consistent with the observed fabric structure. The deformation mechanisms governing the fabric response under tensile loads include textural evolution by means of reorientation of constituent fibers, fiber stretch and junction unraveling. The results of the cyclic loading tests indicate that the tensile deformation of the fabric is a combination of elastic deformation from fiber stretch, and inelastic deformation from irrecoverable reorientation of fibers, relative fiber slip as well as fiber disentanglement. Experimental observations in uniaxial cyclic loading tests indicate that the fabric response is dominated by inelastic deformation mechanisms, especially irrecoverable textural evolution and junction unraveling. Results from biaxial tensile tests confirm this observation.

Chapter 3

An orthotropic continuum model for the elastic response of distributed fiber networks

"Distributed fiber network" is a term that can be used to describe a class of materials composed by a web of fibers or macromolecules, entangled or bonded, either randomly or systematically, by mechanical or chemical processes. A number of engineering materials can be categorized as a distributed fiber network, including synthetic polymers, elastomers, biological tissues, engineering scaffolds, papers, and nonwoven fabrics. The mechanical response of these fiber network materials is generally very complex: it is highly nonlinear, anisotropic, and governed by elastic mechanisms (e.g., stretching and rotating of the constituent fibers), as well as viscoelastic mechanisms (e.g., fiber creep), and irrecoverable mechanisms (e.g., fiber slip, fiber rupture and bond breakage). To formulate a micromechanics-based continuum model for this class of materials, the fiber network response is typically decomposed into a number of constitutive components, each representing a type of deformation mechanism. A constitutive component may consist of an equilibrium (elastic spring) element, a time-dependent (viscous dashpot) element, or a combination thereof, e.g., a viscoelastic element. This modeling approach has been successfully used in formulating a large number of constitutive models for distributed fiber network materials, including viscoelastic models for elastomers [7], models for thermoplastics [57], models for filled elastomers [26], and models for protein based materials [76]. Even though varied in details and formulations, the models listed above share one common assumption: the fibers within the network are randomly distributed, and therefore, the macroscopic response of the network is assumed to be initially isotropic. Many of these models share a common representation of the underlying *isotropic* network elasticity based on an "eight chain" representation of the macromolecular network structure, with non-Gaussian statistics governing the entropy-driven behavior of individual chains. The eight chain model was initially introduced for elastomeric materials [2], [72] and accurately captures the cooperative nature of network deformation while requiring a minimal number of parameters.

Yet, the macroscopic response of many distributed fiber network materials, such as particle-filled elastomers, nonwoven felts, and biological tissues, can exhibit some directional dependence due to (a) a biased distribution of the constituent fibers, and/or (b) preferential alignment of the inter-fiber junctions/bonds/entanglements. Several attempts have been made to incorporate these morphological sources of anisotropy into constitutive models. The approach followed by Bischoff et al. [12], [13], and by Diani et al. [25] relies on homogenization of the response of an anisotropic representative volume elements, while Gasser et al. [32] employed a tensorial representation of a transversely isotropic fiber network structure in a continuum formulation.

The purpose of this work is to introduce an alternative approach to formulate an anisotropic constitutive relation for the elastic response of distributed fiber networks combining the desirable features of the models proposed in the literature. As in [6], [7], [13] the microstructural properties of the constituent fibers and the microstructural sources of network anisotropy constitute the foundation for the macroscopic response; these microstructural features are captured in a tensorial representation which is embedded (as in [13]) in a continuum formulation. The morphological sources of network anisotropy are represented by a second-rank, symmetric positive-definite fabric tensor derived from the orientation distribution of microstructural features of the network structure. Following the physical interpretation of the morphological source, the structural tensor is incorporated into an orthotropic constitutive model for the elastic response of the distributed fiber network. We compare the proposed formulation with models in the literature and demonstrate how the proposed model can efficiently and effectively capture the morphological sources of mechanical anisotropy and the macroscopic response resulting from the distributed nature of the fiber network.

3.1 Literature review

The mechanical response of distributed fiber networks is governed by the deformation and interactions of the constituent fibers (or macromolecules). A number of constitutive models for fiber networks proposed in the literature ([2], [6], [7], [9], [12]-[13], [19], [25]-[26], [72], and [77]) follow the representative volume element (RVE) approach. In this approach, the fiber network is represented by a spatially periodic volume element (polyhedron), which contains a number of fibers embodying the essence of the microstructure under consideration; the macroscopic response of the network is obtained by homogenization of the RVE response. Notable examples of this approach include the three-, four-, eight- and full- chain models (see [19] for a review of these models). Note that these models were originally developed for isotropic networks, and therefore all chains within the RVE are identical. Among these formulations, the isotropic eight-chain model proposed by Arruda and Boyce [2] (referred to as the "AB-model" in the following) is widely employed because of its simplicity and efficiency. In the AB-model, eight representative chains are joined at the RVE center and directed along the diagonals of a cubic RVE. At each material point, the RVE edges are aligned with the principal stretch directions, so that the chain stretch (identical in all chains) is directly related to the first invariant of the Left Cauchy-Green tensor, $\underline{B} = \underline{F}\underline{F}^T$, where $\underline{F}$ is the macroscopic deformation gradient. As a consequence, the AB-model can be interpreted in a purely continuum framework by introducing the concept of an effective network stretch: $\lambda_{eff} = \sqrt{\frac{tr(\underline{B})}{3}}$, without any reference to the underlying micromechanical RVE representation [2].

Constitutive models development for anisotropic distributed network materials often rely on generalizations of the isotropic models. In the following sections, we discuss in detail three anisotropic models for elastic networks: (a) the directional model by Diani et al. [25], (b) the orthotropic eight-chain model by Bischoff et al. [12], and (c) the transversely isotropic distributed fiber network model by Gasser et al. [32]. The first two models are based on the RVE approach, while the latter incorporates the fiber network anisotropy using a tensorial representation of the network structure.

3.1.1 Directional model

The directional model proposed by Diani et al. [25] (referred to as the D-model in the following) idealizes the network structure through representative volume elements defined by symmetric polyhedra (e.g. a tetrahedron, a cube, an octahedron or a dodecahedron). For each solid, a set of fibers are considered along directions defined by linking the center of the solid to each vertex. Thus, four fibers are defined by a tetrahedron, eight fibers by a cube, six fibers by an octahedron, and twenty fibers by a dodecahedron. Each of the fibers in the RVE can be assigned a *different statistical weight* to reflect the anisotropy in the fiber orientation distribution in the distributed network. For an adequate representation of distributed network anisotropy, higher-order polyhedra are necessary. The macroscopic response of the model is derived through a hyperelastic formulation where the strain energy density is obtained by summing contributions from each fiber. The model enforces an incompressibility constraint, and captures the force-stretch relations for individual fiber using Langevin statistics. This model has been shown to capture with good approximation the uniaxial and biaxial responses of a filled natural rubber [26]. For formulations in which the fibers display a nonlinear response with a limiting (locking) stretch, the response of the model at large stretches tends to be overly stiff, as it tends to be dominated by the stress contributions of the chains aligned with the maximum principal stretch. This model shortcoming is particular significant for higher-order polyhedra, where it mirrors well recognized effects in the full-chain model [77] (Figure 3-1).

3.1.2 Orthotropic eight-chain model

Bischoff et al. [12], [13] proposed an orthotropic hyperelastic model (referred to as the "B-model" in the following) which relies on a rectangular prism RVE with eight identical non-Gaussian chains arranged along its diagonals (Figure 3-2). As in the D-model, the macroscopic response of the network is derived through a hyperelastic formulation where the strain energy density of the RVE is obtained by summing contributions from each chain. The model was originally proposed with a force-stretch relation for the individual chains based on Langevin statistics, and then extended to arbitrary force-stretch relationships in [14]. The B-model is formulated for compressible materials and accounts for additional mechanisms of resistance to volumetric deformation through a distinct isotropic contribution, Ψ_{bulk}, to the RVE elastic

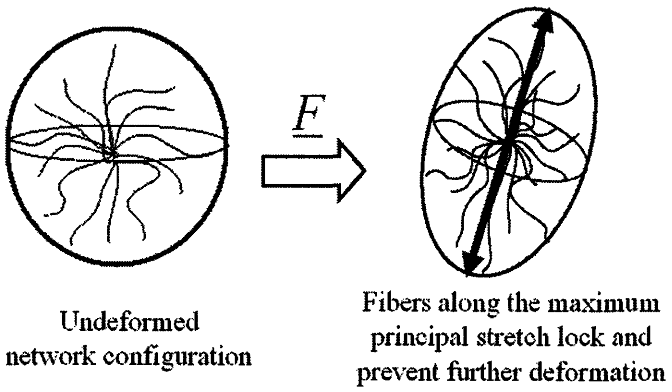

Figure 3-1: Drawback for full-chain models (and for the D-model with higher-order polyhedra): when fibers along the maximum principal stretch reach their limiting extension, the RVE response becomes overly stiff.

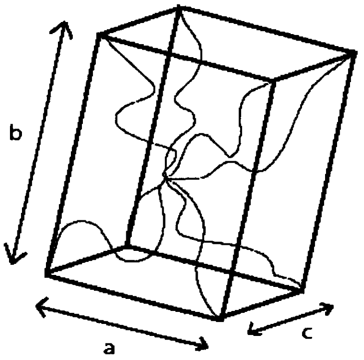

Figure 3-2: Representative volume element of the B-model [12]

strain energy:

$$\Psi_B = \Psi_{chain}\left(\underline{C}, \underline{a}, \underline{b}, \underline{c}\right) + \Psi_{bulk}\left(J\right) \tag{3.1}$$

where Ψ_{chain} is the strain energy due to *entropic* and *repulsion* contributions from the individual chains, $\underline{C}$ is the right Cauchy-Green tensor, $\underline{a}$, $\underline{b}$ and $\underline{c}$ are the orthogonal basis vectors of the RVE $\left(\underline{a} = a\underline{e}_a; \underline{b} = b\underline{e}_b; \underline{c} = b\underline{e}_c\right)$, and $J = \det\left(\underline{F}\right)$ is the ratio of the deformed to the undeformed volume. At each material point, the basis vectors of the RVE are aligned with the principal directions of material anisotropy in the undeformed configuration, and biased to capture the degree of directionality in the material response. The anisotropy of the macroscopic response for the B-model stems from the bias in the RVE dimensions. To visualize this effect, consider a material with preferential chain alignment along a single direction, and a corresponding RVE where $\underline{b}$ is aligned with the preferential direction so that $\underline{b} >> \underline{a}$, $\underline{c}$ (Figure 3-3). Consider a chain behavior characterized by a limiting locking stretch, and the different effects of (1) a macroscopic stretch (λ_b) aligned with the $\underline{b}$ basis vector, and (2) a macroscopic stretch of the same magnitude ($\lambda_a = \lambda_b$) aligned now with the $\underline{a}$ basis vector. It is easy to prove (Figure 3-3) that λ_b will introduce larger chain stretches, and cause the RVE to "lock" at lower levels of macroscopic axial stretch. In other words, the B-model implicitly accounts for the anisotropy of material extensibility, where the "macroscopic locking stretch" depends on the direction of elongation [1].

This feature of the response of the B-model is in good agreement with experimental measurements of distributed fiber network responses [9], [12].

The main shortcomings of the B-model becomes apparent when considering that the symmetry of the RVE is reduced to cubic, and not isotropic [2], in the limiting case of unbiased fiber orientation ($\underline{a} = \underline{b} = \underline{c}$). Note that the representation of the cubic RVE appears identical to the RVE for the isotropic AB model. However, the responses of the cubic B-model and that of the AB-model are identical only when the principal directions of the applied macroscopic stretch are aligned with the basis vectors of the cubic RVE. If the principal stretch directions

---

[1] In this aspect, the B-model differs from the D-model, where the macroscopic limit extensibility is not biased by the anisotropy of fiber distribution.

[2] This can be easily seen by considering the response of the B-model to pure shear and simple shear and by showing that the stress responses do not simply differ by a rotation.

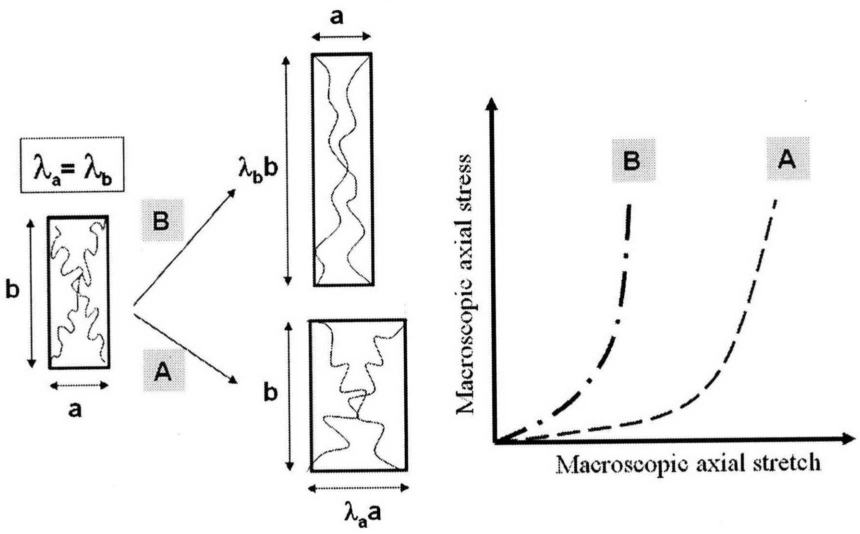

Figure 3-3: The macroscopic extensibility in the B-model is biased by the magnitude of the base vectors

are not aligned with the RVE basis vectors (e.g., the RVE is sheared), the response of the cubic B-model is substantially stiffer, as shown in Figure 3-7 and 3-8. This discrepancy is interpreted in the schematic in Figure 3-4 which illustrates how the shear response of the B-model is dominated by the response of the stretched diagonal chains, while the RVE of the AB-model is oriented with macroscopic stretch and captures the effect of deformation through a uniform chain stretch. The significance of this shortcoming of the B-model is not limited to cases of isotropic or nearly-isotropic chain distributions. Rather, it underlies the limitation of a model in which the entire network response is calculated on the basis of the deformation of eight particular chains. There are no special reasons to assume that these eight chains should be able to embody the response of the entire distributed network.

Notwithstanding these arguments, we note that the B-model exhibits many desirable features and, *in the case of coalignment of macroscopic stretch and RVE orientation*, it is able to capture, with remarkable simplicity of implementation, complex effects in anisotropic distributed elastic networks [12].

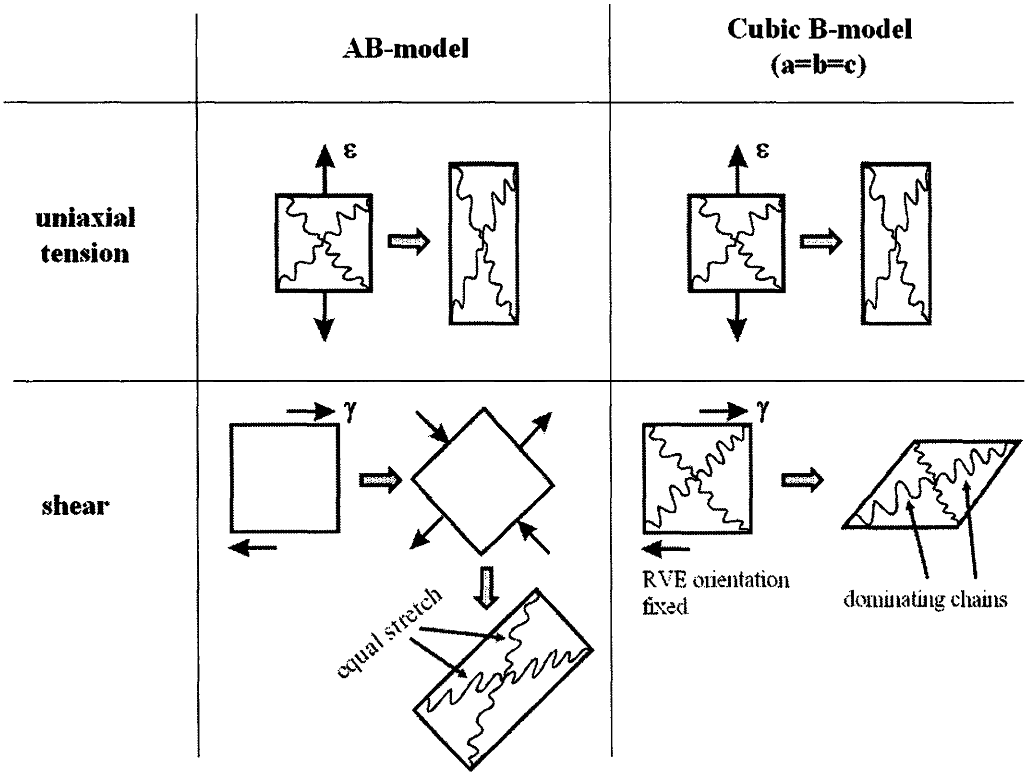

Figure 3-4: Deformation response of the isotropic AB model the cubic B-model. In shear, the AB-RVE is oriented along the principal directions of stretch while the B-RVE is fixed to the material frame. Hence, the shear response of the B-model is controlled by the response of the dominating chains, and not by the average response of all chains in the network.

3.1.3 Transversely isotropic hyperelastic model for distributed fiber network

Gasser et al. [32] recently introduced a transversely isotropic hyperelastic formulation (referred to as the "G-model" in the following) for the elastic layers of arterial walls. The authors proposed a composite model consisting of distributed collagen fibers embedded in a "ground substance". The collagen network was idealized as a transversely isotropic incompressible continuum with an exponential stress-stretch response, while the surrounding ground substance was modeled through an incompressible isotropic neo-Hookean formulation. To capture the distributed nature of the collagen fibers, the density distribution of the fiber orientation was represented by a transversely isotropic, symmetric, positive definite structural tensor. This model was shown to accurately and efficiently capture the elastic response of the arterial layers, but its applicability is limited to transversely isotropic networks.

In summary: the D-model and the B-model represent network anisotropy using biased RVEs: the D-model considers RVEs with unbiased dimensions but biased weights of the representative fibers, while the B-model considers an RVE with biased dimensions and equally-weighted fibers. These RVE approaches only account for the deformation resistance of "representative" network fibers in directions identified by the specific RVE geometry. For *distributed* fiber network materials, this approach might prove inadequate since the effects of the deformation are selectively accounted for only for the "representative fibers" while forgoing the effects of fiber deformation in all other directions. In this regard, the tensorial approach proposed by Gasser et al. is more appealing because it efficiently incorporates the contributions of all fibers. Yet, the current G-model is only limited to a transversely isotropic incompressible network formulation. In this work, the tensorial approach will be generalized to include network compressibility and orthotropic symmetry.

3.2 Sources of Mechanical Anisotropy in Distributed Fiber Networks

Directionality in the macroscopic response of a distributed fiber network may arise from a number of sources, including:

- preferential orientation in the fiber distribution

- biased distribution of junction-to-junction distance (e.g., from needlepunch pattern)
- overlays of multiple families of different constituent fibers.

Here, we consider a distributed network created from entanglements of one family of fibers, and hence, the network anisotropic response arises from the first two sources:

1) *Fiber orientation distribution (FOD)* – This distribution represents the normalized probability of having fibers aligned in each material direction, and gives rise to deformation resistance biased toward the directions of preferential fiber alignment. This morphological property can be measured by a number of image analysis techniques, (see, e.g., [64]-[65], and Jahne [42]).

2) *Orientation distribution of junction-to-junction distance (JJD)*[3] – the normalized distance between two junctions in each material direction. This distribution is related to the anisotropy of the extensibility limits of the network, and gives rise to the stress contributions that are biased in the directions of long junction-to-junction distances (analogously to the schematic interpretation in Figure 3-3). The junctions of distributed fiber networks can be further categorized into two broad classes based on the mechanisms by which junctions are created: patterned junctions created by controlled bonding processes, and random junctions created by spontaneous bonding of structural fibers in their quasi-melt state (e.g., in mats created by electrospinning. The JJD of distributed networks with patterned junctions, as in needlepunched nonwoven fabrics, can be directly measured from the images of the network structure. On the other hand, the JJD of distributed networks with random junctions cannot be easily measured by the currently available image analysis techniques. However, the JJD of the distributed network with random junctions can be related to the FOD of the network because the locations of inter-fiber junctions are statistically biased by the number of fiber intersections, which is related to the fiber orientation distribution[4].

The directionality of morphological sources of anisotropy can be captured in a continuum framework by expressing such morphological sources in terms of orientation distribution functions (or density functions). Following Kanatani [45], an orientation distribution function (ODF) can be represented by a spherical harmonic series;

---

[3] *In this work, 'junctions' are defined by the spatial positions where two or more fibers are inter-connected. The junctions are assumed to be "unyielding", i.e., fiber slippage at junction points is not considered as a deformation mechanism.*

[4] See Appendix A for a relationship between the JJD and the FOD for a simplified network with straight cylindrical inter-penetrable fibers.

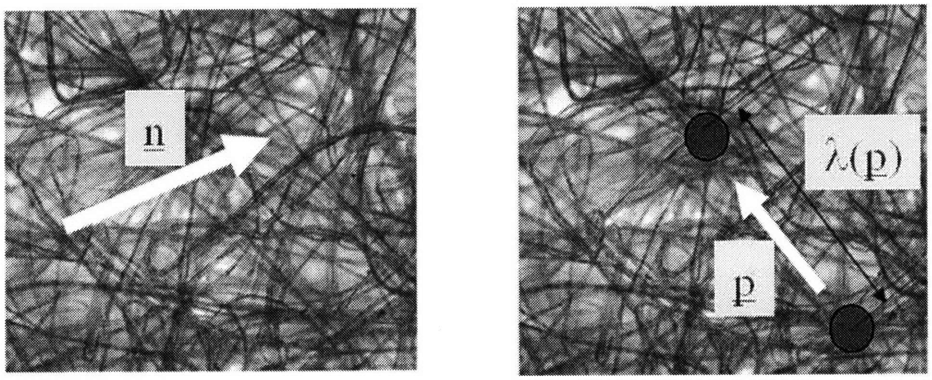

Fiber Orientation Distribution

Junction to Junction Distance Distribution

Figure 3-5: Illustrations of orientation distribution of fiber density and orientation distribution of junction-to-junction distance

$$w\left(\underline{n}\right) = 1 + \underline{W'} : \left(\underline{n} \otimes \underline{n}\right) + \underline{A'} : \left(\underline{n} \otimes \underline{n} \otimes \underline{n} \otimes \underline{n}\right) + HOT\left(\underline{n}^{6}\right), \tag{3.2}$$

where $w\left(\underline{n}\right)$ is the orientation distribution function, $\underline{n}$ is the unit direction, 1 is the scalar first order coefficient representing a uniform distribution (i.e., spherical), $\underline{W'}$ is the deviatoric second-rank symmetric coefficient tensor, $\underline{A'}$ is the deviatoric fourth rank symmetric coefficient tensor, and HOT indicates the higher order terms[5]. Because the ODF is a probability density function, it must satisfy the normalization condition when integrated over all material directions;

$$\frac{1}{4\pi}\int\limits_{4\pi} w\left(\underline{n}\right) d\underline{n} = 1. \tag{3.3}$$

For most materials where the assembly of the fiber network is dominated by random processes (as in the lay-up for electrospun mats), the resulting orientation distribution is not limited to a select number of preferential directions (as in unidirectional composites) but is more "distributed" in nature. For these systems, the orientation distribution function can be approximated to the second order accuracy by an ellipsoidal distribution, represented by a

---

[5] This development applies to distribution functions which are even functions of vector $\underline{n}$, i.e., the distribution for which $w\left(\underline{n}\right) = w\left(-\underline{n}\right)$

second-rank symmetric structural tensor $\underline{W}$. In this case, the orientation distribution function $w\left(\underline{n}\right)$ and the fabric ellipsoid $\underline{W}$ are related by

$$w\left(\underline{n}\right) = 1 + \underline{W'} : \left(\underline{n} \otimes \underline{n}\right) = \underline{W} : \left(\underline{n} \otimes \underline{n}\right). \tag{3.4}$$

Equation 3.4 is only applicable when $\underline{W}$ satisfies the normalization condition $tr\left(\underline{W}\right) = 3$, which is consistent with the normalization condition (3.3)[6]. Note that the second-rank fabric ellipsoid is only capable of representing materials with isotropic, transversely isotropic or orthotropic symmetries.

With the assumption that both the FOD and the JJD can be well approximated to second order accuracy, they can be expressed in terms of their ellipsoidal texture tensors, and these structural measures of material anisotropy can be used to capture the macroscopic response of distributed networks. For distributed networks in which the anisotropy of fiber orientation is combined with random entanglement processes, the combined effects of FOD and JJD are well captured by the microstructural representation of the RVE in Figure 3-3. This representation provides a heuristic interpretation for a corresponding tensorial representation of the network anisotropy through a single "fabric ellipsoid", $\underline{G}_0$.

With reference to the RVE in Figure 3-6, the principal directions of the representative network microstructure are denoted by $\underline{e}_A, \underline{e}_B, \underline{e}_C$ with corresponding junction-to-junction distances A, B, C. Parameters A, B, C represent average values of the actual distances between entanglement/junction points in the material network. The average end-to-end (unstretched) fiber length for each of the 8 fiber segments in the RVE is defined as

$$r_0 = \frac{1}{2}\sqrt{A^2 + B^2 + C^2}, \tag{3.5}$$

with a total end-to-end (unstretched) fiber length in the RVE (along the four diagonals) given by:

$$L = 4\sqrt{A^2 + B^2 + C^2}, \tag{3.6}$$

---

[6] Recall that $\frac{1}{4\pi}\int\limits_{4\pi}\left[\frac{tr(\underline{W})}{3}\left(\underline{I} : \left(\underline{n} \otimes \underline{n}\right)\right) + \underline{W'} : \left(\underline{n} \otimes \underline{n}\right)\right] d\underline{n} = \frac{tr(\underline{W})}{3}$

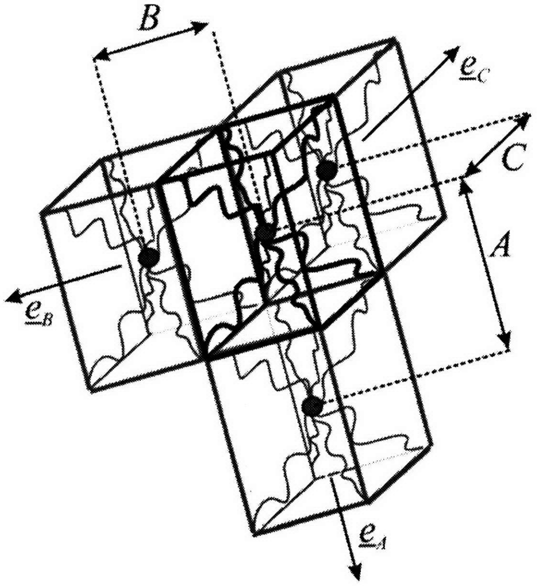

Figure 3-6: Representative Volume Element for distributed orthotropic network

and a number of fiber segments per unit volume:

$$n_0 = \frac{8}{ABC}. \tag{3.7}$$

The fully-extended (locked) fiber length associated with the RVE can be related to L through the fiber locking stretch [7], λ_L, so that a relationship between total fiber length per unit volume ρ_L, an experimentally measurable parameter), and RVE parameters can be obtained as

$$\rho_L = \frac{\lambda_L L}{ABC} = \frac{4\lambda_L\sqrt{A^2+B^2+C^2}}{ABC}. \tag{3.8}$$

To provide a dimensionless representation of the network anisotropy, we introduce a characteristic network length, d_0, defined as the junction-to-junction distance of an equiaxial RVE ($A = B = C = d_0$) with the same value of end-to-end (unstretched) fiber length r_0:

$$r_0 = \frac{1}{2}\sqrt{A^2+B^2+C^2} = \frac{\sqrt{3}}{2}d_0 \rightarrow d_0 = \sqrt{\frac{A^2+B^2+C^2}{3}}, \tag{3.9}$$

---

[7] The fiber locking stretch can be related in nonwoven fabrics to the average fiber curl between junctions.

The normalized junction-to-junction distances along principal directions are then defined as

$$A_0 = \frac{A}{d_0}, \quad B_0 = \frac{B}{d_0}, \quad C_0 = \frac{C}{d_0}. \tag{3.10}$$

We can now introduce a tensorial representation of the network structure in terms of the normalized "fabric ellipsoid", $\underline{G}_0$:

$$\underline{G}_0 = A_0\underline{e}_A \otimes A_0\underline{e}_A + B_0\underline{e}_B \otimes B_0\underline{e}_B + C_0\underline{e}_C \otimes C_0\underline{e}_C. \tag{3.11}$$

The normalization (3.9) results in $tr\,(\underline{G}_0) = 3$, so that $\underline{G}_0$ can be interpreted in terms of the first two terms of the expansion for an orientation distribution function (3.4).

The junction-to-junction distance in direction $\underline{p}$ can be obtained in terms of the normalized fabric ellipsoid $\underline{G}_0$ and the characteristic network length d_0 as:

$$d_0^p = d_0\sqrt{\underline{G}_0 : (\underline{p} \otimes \underline{p})}, \tag{3.12}$$

which provides an average junction-to-junction distance for the network

$$\widehat{d_0^p} = \sqrt{\frac{1}{4\pi}\int\limits_{4\pi} (d_0^p)^2 \, d\underline{p}} = d_0\sqrt{\frac{1}{4\pi}\int\limits_{4\pi} \underline{G}_0 : (\underline{p} \otimes \underline{p}) \, d\underline{p}} = d_0. \tag{3.13}$$

Note that, consistently with the micromechanical representation of the network structure, the end-to-end (unstretched) fiber length in direction $\underline{p}$ scales with the junction-to-junction distance in direction $\underline{p}$ through a geometric factor $\frac{\sqrt{3}}{2}$:

$$r_0^p = \frac{\sqrt{3}}{2} d_0^p = \frac{\sqrt{3}}{2} d_0\sqrt{\underline{G}_0 : (\underline{p} \otimes \underline{p})}, \tag{3.14}$$

which, when averaged over all directions yields back the average end-to-end (unstretched) fiber length r_0:

$$\widehat{r_0^p} = \frac{\sqrt{3}}{2}\widehat{d_0^p} = \frac{\sqrt{3}}{2} d_0 = r_0. \tag{3.15}$$

In the following section we introduce a constitutive formulation for the elastic response of a distributed orthotropic network characterized by the fabric ellipsoid $\underline{G}_0$.

3.3 Anisotropic Elasticity for Orthotropic Distributed Fiber Networks

The proposed formulation is specialized to networks of elastic "fibers" with limited extensibility. This class of material encompasses nonwoven fabrics as well as elastomers and biological materials with macromolecular components such as elastin, collagen, titin, and DNA. The force-stretch relationship for this class of fibers (macromolecules) has been described through a number of formulations including the worm-like-chain model, and the freely-jointed chain model. Most models introduce a measure for the limiting stretch of the fibers, which we will refer to as the "locking stretch" λ_L, and express the force-stretch relations for the fiber in terms of the fiber stretch ratio $\chi = \frac{\lambda_f}{\lambda_L}$, where λ_f is the end-to-end fiber stretch. In order to formulate a continuum model for the network response we introduce the following assumptions:

1) The junctions can be modeled as material points which displace in an affine manner with the continuum. The contravariant structural tensor $\underline{G}_0$ is transformed by the deformation gradient, $\underline{F}$, according to the push-forward operation:

$$\underline{G} = \underline{F}\underline{G}_0\underline{F}^T, \tag{3.16}$$

where $\underline{G}$ represents the junction distribution in the deformed (loaded) configuration.

2) The structural tensor $\underline{G}_0$ in the unloaded configuration does not evolve with deformation and the original network texture is recovered upon unloading.

3) Fibers do not undergo any inelastic deformation, do not rupture and do not slip from the junctions, so that the end-to-end unstretched fiber length, and the number of fiber segments per unit volume are constant.

Within this framework we can define an effective measure of fiber stretch λ_{eff} as follows.

As the network deforms, and the fabric ellipsoid $\underline{G}_0$ is transformed to $\underline{G}$ (Equation 3.16), the end-to-end length of fibers in reference direction $\underline{p}$ can be obtained as

$$r^p = \frac{\sqrt{3}}{2} d^p = \frac{\sqrt{3}}{2} d_0 \sqrt{\underline{G} : (\underline{p} \otimes \underline{p})} = \frac{\sqrt{3}}{2} d_0 \sqrt{\underline{F}\underline{G}_0\underline{F}^T : (\underline{p} \otimes \underline{p})}, \tag{3.17}$$

with an average end-to-end fiber length

$$\begin{aligned} \widehat{r}^p &= \sqrt{\frac{1}{4\pi}\int\limits_{4\pi} \left(r^p\right)^2 d\underline{p}} = \frac{\sqrt{3}}{2} d_0 \sqrt{\frac{1}{4\pi}\int\limits_{4\pi} \left(\underline{F}\underline{G}_0\underline{F}^T : \left(\underline{p}\otimes\underline{p}\right)\right) d\underline{p}} \qquad (3.18a) \\ &= \frac{\sqrt{3}}{2} d_0 \sqrt{\frac{tr\left(\underline{F}\underline{G}_0\underline{F}^T\right)}{3}}. \qquad (3.18b) \end{aligned}$$

An effective stretch can be defined as

$$\lambda_{eff} = \frac{\widehat{r}^p}{\widehat{r}_0^p} = \sqrt{\frac{tr\left(\underline{F}\underline{G}_0\underline{F}^T\right)}{3}}, \qquad (3.19)$$

and an effective fiber stretch ratio can be defined as:

$$\chi_{eff} = \frac{\lambda_{eff}}{\lambda_L} = \sqrt{\frac{tr\left(\underline{F}\underline{G}_0\underline{F}^T\right)}{3\left(\lambda_L\right)^2}}. \qquad (3.20)$$

We can offer an alternative, qualitative interpretation for the derivation of expression (3.20). This interpretation relates to directionality effects on the macroscopic locking stretch for the entire network, as schematically illustrated in Figure 3-3. Consider uniaxial loading of the RVEs in Figure 3-6 along the principal directions of anisotropy. Neglecting all resistance to volumetric compaction, and assuming that all the representative fibers in the RVE can pivot around the junction points, becoming aligned with the loading direction, and stretch to their extensibility limit, the dimensions of the stretched RVE in the loading and transverse directions tend toward $[\lambda_L r_0, 0, 0]$, respectively. This configuration corresponds to macroscopic locking stretches

$$\overline{\lambda}_L^A = \lambda_L \frac{r_0}{A} = \frac{\sqrt{3}}{2}\frac{\lambda_L}{A_0}; \quad \overline{\lambda}_L^B = \lambda_L \frac{r_0}{B} = \frac{\sqrt{3}}{2}\frac{\lambda_L}{B_0}; \quad \overline{\lambda}_L^C = \lambda_L \frac{r_0}{C} = \frac{\sqrt{3}}{2}\frac{\lambda_L}{C_0} \qquad (3.21)$$

in principal directions $\underline{e}_A, \underline{e}_B, \underline{e}_C$, leading to the notion of a direction-dependent macroscopic locking stretch which scales in inverse proportion to the junction-to-junction distance in that direction. The macroscopic locking stretch in direction $\underline{p}$ can be then cast in the form

$$\overline{\lambda}_L\left(\underline{p}\right) \propto \frac{\lambda_L}{\sqrt{\underline{G}_0 : \left(\underline{p}\otimes\underline{p}\right)}}. \qquad (3.22)$$

A macroscopic deformation $\underline{F}$, would lead to an effective stretch ratio in direction $\underline{p}$ biased by the direction-dependent macroscopic locking stretch:

$$\overline{\chi}\left(\underline{p}\right) = \frac{\lambda\left(\underline{p}\right)}{\overline{\lambda}_L\left(\underline{p}\right)} \propto \sqrt{\frac{\left(\underline{FF^T} : \left(\underline{p}\otimes\underline{p}\right)\right)\left(\underline{G}_0 : \left(\underline{p}\otimes\underline{p}\right)\right)}{\left(\lambda_L\right)^2}}, \tag{3.23}$$

so that the relationship (3.20) can be interpreted as an average over all material directions of (3.23), relating (3.20) to the notion of a direction-dependent macroscopic locking stretch for the network. In other words, the directional bias in the macroscopic locking stretch for the network is captured in (3.20) by considering an isotropic macroscopic locking stretch, but biasing the continuum stretch ($\underline{FF^T}$) by the structural tensor $\underline{G}_0$.

In order to formulate a continuum model for the distributed fiber network, we need to select a specific form for the force-stretch relation for individual fibers. A direct comparison between the proposed model (which we will refer to as the JS-model in the following), the D-model, and the B-model predictions is facilitated by selecting the same force-stretch relations, based on Langevin statistics, for the constituent fibers. This formulation is rigorously appropriate only for fibers (macromolecules) with persistence length much lower than the end-to-end length, so that the entropic contribution to elasticity dominates. However, the force-stretch relation corresponding to this formulation has also been shown to be able to *phenomenologically* capture the response of networks of fibers with large persistence length and internal energy-dominated elastic response; examples include applications of this modeling approach to collagenous networks in biological tissues (e.g., [10]) and electrospun PCL mats [27].

The strain energy associated with the stretch of a single fiber segment can then be cast in terms of the end-to-end stretch, λ_f , as (see, e.g., [2]):

$$\psi_{fiber}\left(\lambda_f\right) = \eta\lambda_L^2\left(\frac{\lambda_f}{\lambda_L}\beta\left(\chi\right) + \ln\left[\frac{\beta\left(\chi\right)}{\sinh\beta\left(\chi\right)}\right]\right) + \psi_0, \tag{3.24}$$

where η is a scaling coefficient with units [Joule], λ_L is the locking stretch of the fiber, $\beta\left(\chi\right)$ is the inverse Langevin function defined by $\chi = \frac{\lambda_f}{\lambda_L} = \coth\left(\beta\left(\chi\right)\right) - \frac{1}{\beta(\chi)}$, and ψ_0 is a constant normalizing the strain energy to zero for $\lambda_f = 1$.

In the proposed model, we evaluate the strain energy density $\overline{\Psi}_{fiber}$ associated with the stretching of n_0 fiber segments per unit (reference) volume, in a network with anisotropy captured by the fabric ellipsoid $\underline{G}_0$, by relying on the concepts of effective fiber stretch λ_{eff} (3.19), and effective stretch ratio χ_{eff} (3.20):

$$\overline{\Psi}_{network}\left(\lambda_{eff}\right)=n_0\eta\lambda_L^2\left(\frac{\lambda_{eff}}{\lambda_L}\beta\left(\chi_{eff}\right)+\ln\left[\frac{\beta\left(\chi_{eff}\right)}{\sinh\beta\left(\chi_{eff}\right)}\right]\right)+n_0\psi_0. \tag{3.25}$$

Note that the strain energy in (3.25) is minimized at $\lambda_{eff}=0$ [12], since it does not account for effects that arise from inter-chain repulsion and prevent entropic collapse.

The corresponding macroscopic (network) second Piola-Kirchhoff stress can be obtained by differentiating the strain energy in (3.25) with respect to the right Cauchy-Green tensor:

$$\underline{T}_{network}=\frac{n_0\eta}{tr\left(\underline{G}_0\right)}\frac{\lambda_L}{\lambda_{eff}}\beta\left(\chi_{eff}\right)\underline{G}_0, \tag{3.26}$$

with corresponding Cauchy stress

$$\underline{\sigma}_{network}=\frac{n_0\eta}{Jtr\left(\underline{G}_0\right)}\frac{\lambda_L}{\lambda_{eff}}\beta\left(\chi_{eff}\right)\underline{FG_0F}^T, \tag{3.27a}$$

where $J=det(F)$ is the volumetric Jacobian of the deformation.

The stress expressions in Equations (3.26 and 3.27a) only account for contributions due to the stretch of individual fibers and, in agreement with the minimization condition for the corresponding strain energy (3.25), yield a stress-free configuration only for $\lambda_{eff}=0$.

To enforce equilibrium conditions in the reference configuration (and recover stability for deformations at constant λ_{eff}, additional contributions reflecting the repulsion of individual chains must be added to the strain energy density $\left(\overline{\Psi}_{repulsion}\right)$ and to the network stress $\left(\underline{T}_{repulsion}\right)$ [11], [12]. A tensorial forms of $\underline{T}_{repulsion}$ consistent with the formulations proposed in [11], [12] can be cast as:

$$\underline{T}_{repulsion}=-\frac{n_0\eta}{tr\left(\underline{G}_0\right)}\lambda_L\beta_0\underline{U}^{-1}\underline{G}_0\underline{U}^{-1}, \tag{3.28}$$

where $\beta_0=\beta\left(\frac{1}{\lambda_L}\right)$ and $\underline{U}$ is the right stretch tensor defined by $\underline{U}^2=\underline{C}$.

By combining the contribution from individual fibers 3.27a and the repulsion term 3.28 we can obtain an expression for the macroscopic (network) second Piola-Kirchhoff stress:

$$\underline{T}_{JS} = \underline{T}_{network} + \underline{T}_{repulsion} = \frac{n_0\eta}{tr\left(\underline{G}_0\right)}\left[\frac{\lambda_L}{\lambda_{eff}}\beta\left(\chi_{eff}\right)\underline{G}_0 - \lambda_L\beta_0\underline{U}^{-1}\underline{G}_0\underline{U}^{-1}\right], \tag{3.29}$$

with corresponding Cauchy stress:

$$\underline{\sigma}_{JS} = \frac{\mu}{Jtr\left(\underline{G}_0\right)}\left[\frac{\lambda_L}{\lambda_{eff}}\beta\left(\chi_{eff}\right)\underline{F}\underline{G}_0\underline{F}^T - \lambda_L\beta_0\underline{R}\underline{G}_0\underline{R}^T\right]. \tag{3.30}$$

where $\mu = n_0\eta$ is a scaling modulus with units of [Pa].

Note that, for materials in which additional mechanisms of resistance to volumetric deformation are present (as in the case of an elastic network embedded in an hydrated ground substance), the stress expressions (3.29, 3.30) might need to be augmented by isotropic terms allowing increased control over the compressibility of the material model. A number of alternative formulations for these (energetic) contributions are reviewed in [11].

For the special case of deformations in which the fiber network is simply stretched (with macroscopic stretches $\lambda_A, \lambda_B, \lambda_C$) along the principal directions of material anisotropy $\underline{e}_A, \underline{e}_B, \underline{e}_C$, the deformation gradient can be expressed as:

$$\underline{F} = \lambda_A\ \underline{e}_A \otimes \underline{e}_A + \lambda_B\ \underline{e}_B \otimes \underline{e}_B + \lambda_C\ \underline{e}_C \otimes \underline{e}_C. \tag{3.31}$$

Under these conditions, the JS-model provides a form of the macroscopic stress identical to the form provided by the network component of the B-model [12][8], with Cauchy stress:

$$\underline{\sigma}_{JS} = \sigma_{AA}\ \ \underline{e}_A \otimes \underline{e}_A + \sigma_{BB}\ \underline{e}_B \otimes \underline{e}_B + \sigma_{CC}\ \underline{e}_C \otimes \underline{e}_C, \tag{3.32}$$

and principal components [9]:

---

[8] Not including the ad-hoc isotropic bulk contribution, $B\ sinh(J-1)$, which is added in [12] to account for possible additional mechanisms of resistance to bulk deformation.

[9] Note that the magnitude of the base vectors in the B-model (a, b, c) are related to the $\underline{G}_0$ principal values (A_0, B_0, C_0) through a scaling factor $\frac{2}{\sqrt{3}}\lambda_L$.

$$\sigma_{AA} = \frac{\mu A_0^2}{Jtr\left(\underline{G}_0\right)}\left[\frac{\lambda_L}{\lambda_{eff}}\beta\left(\chi_{eff}\right)\lambda_A^2 - \lambda_L\beta_0\right]; \tag{3.33a}$$

$$\sigma_{BB} = \frac{\mu B_0^2}{Jtr\left(\underline{G}_0\right)}\left[\frac{\lambda_L}{\lambda_{eff}}\beta\left(\chi_{eff}\right)\lambda_B^2 - \lambda_L\beta_0\right]; \tag{3.33b}$$

$$\sigma_{AA} = \frac{\mu C_0^2}{Jtr\left(\underline{G}_0\right)}\left[\frac{\lambda_L}{\lambda_{eff}}\beta\left(\chi_{eff}\right)\lambda_C^2 - \lambda_L\beta_0\right]. \tag{3.33c}$$

It is then not surprising that under (tensile) uniaxial loading along principal material directions the JS-model yields predictions identical to the B-model, as illustrated in Figure 3-7. For convenience of illustration, a single measure of anisotropy, α, is introduced ($\alpha = A_0/B_0; C_0 = 1$), and model predictions for the macroscopic axial stress-stretch response along the $\underline{e}_A$ and $\underline{e}_B$ directions are compared for increasing levels of anisotropy (α=[1., 1.5, 2., 2.5]). Predictions in figure 3-7 have been obtained for model parameters [μ = 1MPa, and λ_L =2]. Note that under this mode of deformation both the JS-model and the B-model recover the isotropic AB-model response for $\alpha = 1$.

Conversely, model predictions for the JS-model and the B-model differ for deformations with directions of principal stretch which are not co-aligned with the principal directions of anisotropy. This effect is illustrated in Figure 3-8, which compares model predictions in simple shear for the same levels of anisotropy considered in figure 3-7. Figure 3-8 compares model predictions for the shear stress σ_{AB} in response to an imposed deformation $\underline{F} = \underline{1} + \gamma_{AB}\underline{e}_A \otimes \underline{e}_B$, where $\underline{1}$ is the 2nd rank identity tensor. The general trends of resistance to shear deformation are consistent between the two models: the material becomes more shear-compliant for increasing levels of anisotropy. The B-model predictions are generally stiffer, as the shear response is dominated by the stretch of two of the diagonal chains, as schematically illustrated in Figure 3-4. Also, as previously discussed, the B-model predictions do not recover the isotropic AB-model prediction for an equiaxial RVE ($\alpha = 1$), while the JS-model predictions corresponding to $\alpha = 1$ recover the isotropic solution.

In order to compare the JS-model predictions with predictions of the D-model, we introduce an approximate incompressibility constraint by augmenting the stress expression in 3.30 with

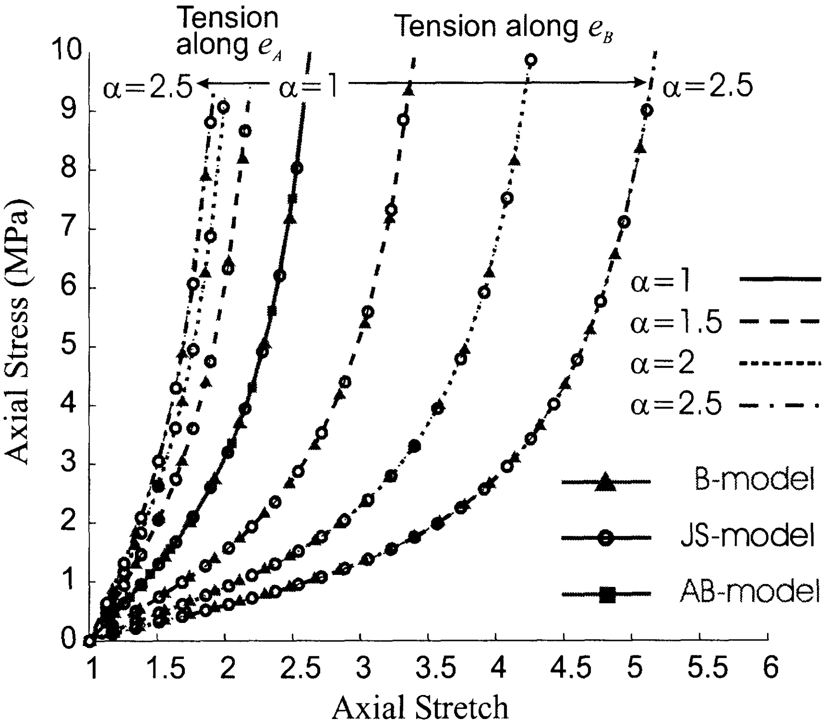

Figure 3-7: Responses of the B-model and the JS-model under uniaxial tension for different levels of orthotropy. Response of the AB-model reflects the isotropic case.

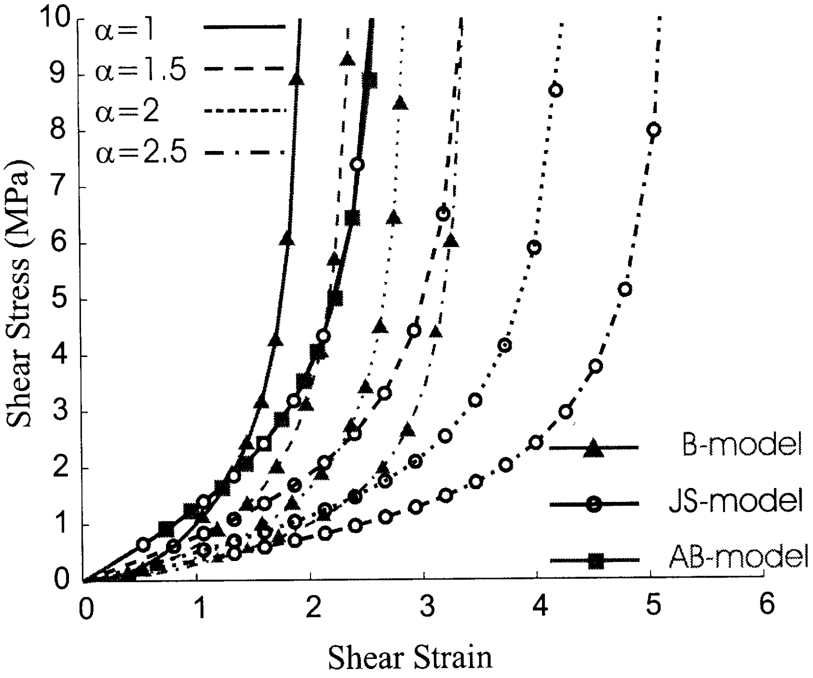

Figure 3-8: Responses of the B-model and the JS-model under simple shear for different levels of orthotropy. Response of the AB-model reflects the isotropic case.

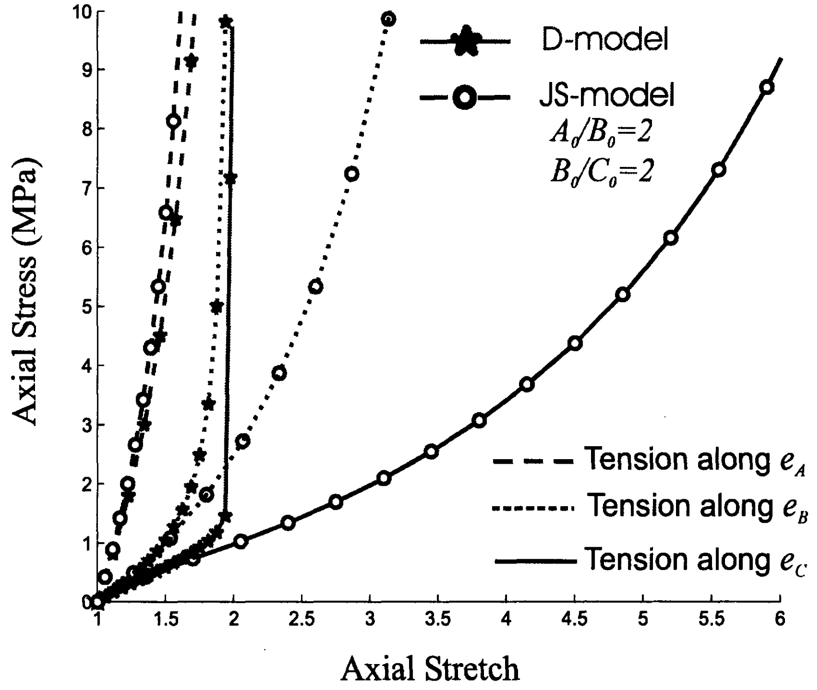

Figure 3-9: Comparisons between D- and JS-models under uniaxial tension with equivalent stiffness in the low-stretch regime

a hydrostatic contribution to the Cauchy stress:

$$\underline{\sigma}_h = K\,(J-1)\,\underline{1}. \tag{3.34}$$

with $K >> \mu$. Note that the contribution of the hydrostatic term 3.34 enforces incompressibility through a "penalty" approach, which becomes less effective as the network stretch approaches its extensibility limit.

Predictions of the D-model are dependent on the specific polyhedron selected to represent the RVE. For this comparison we have selected the simple 14-chain model proposed in [25] to fit the anisotropic response of calendered rubber specimens. The force-stretch relations for the component fibers in the JS-model and D-model are based on the same Langevin statistics, so we can select identical levels of locking stretch, $\lambda_L = 2$, and macroscopic moduli, $\mu = 1MPa$ A direct correlation between anisotropy measures in the two models cannot be determined since they rely on different micromechanical representations/interpretation of the sources of anisotropy. The D-model RVE is primarily designed to capture the effects of fiber orientation distribution, biasing the stress in the direction of increased fiber density and it does not account for the directional dependence of the network extensibility limit. This is apparent in Figure 3-9, which compares model predictions in uniaxial loading along the $\underline{e}_A$ and $\underline{e}_B$ principal directions. The JS model predictions are obtained for $[A_0/B_0 = \alpha; B_0/C_0 = 2]$. The bias in fiber density for the D-model has been selected so as to provide a good fit between model predictions in the low-stretch regime. However, as evident in Figure 3-9, model predictions diverge at large stretches, as the D-model predicts identical extensibility limits for the network in all material directions.

Remarks

1) To be consistent with the tenets of continuum mechanisms, the presented constitutive relation in Equation 3.30 must satisfy (a) objectivity and (b) material symmetry. An objective constitutive relation must remain invariant under a change in frame of the observer. To demonstrate the objectivity of the presented constitutive relation, we consider a reference frame rotated by an arbitrary rigid body rotation $\underline{Q}$, and consider the corresponding deformation gradient $\underline{F}^+ = \underline{Q}\ \underline{F}$, so that the Cauchy stress in the rotated frame becomes:

$$\underline{\sigma}_{JS}^+ = \frac{\mu}{J^+ tr\left(\underline{G}_0\right)} \left[\frac{\lambda_L}{\lambda_{eff}^+} \beta\left(\chi_{eff}^+\right) \underline{Q}\underline{F}\underline{G}_0\underline{F}^T\underline{Q}^T - \lambda_L \beta_0 \underline{Q}\underline{R}\underline{G}_0\underline{R}^T\underline{Q}^T \right]. \tag{3.35}$$

where + denotes quantities in the rotated frame. Note that $J^+ = J$,

$$\lambda_{eff}^+ = \sqrt{\frac{tr\left(\underline{F}^+\underline{G}_0\underline{F}^{+T}\right)}{3}} = \sqrt{\frac{tr\left(\underline{F}^{+T}\underline{F}^+\underline{G}_0\right)}{3}} = \sqrt{\frac{tr\left(\underline{F}^T\underline{F}\underline{G}_0\right)}{3}} = \lambda_{eff}, \tag{3.36}$$

and $\chi_{eff}^+ = \chi_{eff}$ so that

$$\underline{\sigma}_{JS}^+ = \underline{Q}\underline{\sigma}_{JS}\underline{Q}^T. \tag{3.37}$$

verifying objectivity.

The symmetry requirement states that the an orthotropic constitutive law must, and its corresponding Cauchy stress measure, must remain unchanged under orthotropic transformations, $\underline{\widetilde{Q}}$, of the reference configuration.

Because $\underline{G}_0$ is the second-rank symmetric tensor representing the orthotropy of the material, it is invariant under the transformation $\underline{\tilde{Q}}$:

$$\underline{\tilde{G}}_0 = \underline{\tilde{Q}}\underline{G}_0\underline{\tilde{Q}}^T = \underline{G}_0. \tag{3.38}$$

The Cauchy stress $\underline{\tilde{\sigma}}_{JS}$ can then be expressed in terms of the deformation gradient $\underline{\tilde{F}} = \underline{F}\underline{\tilde{Q}}$ and the structural tensor $\underline{\tilde{G}}_0$ as:

$$\underline{\tilde{\sigma}}_{JS} = \frac{\mu}{\tilde{J}tr\left(\underline{G}_0\right)}\left[\frac{\lambda_L}{\tilde{\lambda}_{eff}}\beta\left(\tilde{\chi}_{eff}\right)\underline{F}\underline{\tilde{Q}}\underline{G}_0\underline{\tilde{Q}}^T\underline{F}^T - \lambda_L\beta_0\underline{R}\underline{\tilde{Q}}\underline{G}_0\underline{\tilde{Q}}^T\underline{R}^T\right]. \tag{3.39}$$

where ˜ denotes quantities related to the transformed reference configuration. Note that $\tilde{J} = J$

,

$$\tilde{\lambda}_{eff} = \sqrt{\frac{tr\left(\underline{\tilde{F}}\underline{G}_0\underline{\tilde{F}}^T\right)}{3}} = \sqrt{\frac{tr\left(\underline{F}\underline{\tilde{Q}}\underline{G}_0\underline{\tilde{Q}}^T\underline{F}^T\right)}{3}} = \sqrt{\frac{tr\left(\underline{F}\underline{G}_0\underline{F}^T\right)}{3}} = \lambda_{eff}, \tag{3.40}$$

and $\tilde{\chi}_{eff} = \chi_{eff}$ so that

$$\underline{\tilde{\sigma}}_{JS} = \underline{\sigma}_{JS}. \tag{3.41}$$

satisfying the symmetry requirements.

2) Even though the current model is formulated based on a force-stretch relation for the constituent fibers derived from Langevin statistics, the concept of effective stretch, and effective stretch ratio can be employed in alternative formulations relying on different models for the response of individual fibers, e.g., the wormlike-chain model [56], and exponential Hart-Smith model [38] [10].

3) The model has eight independent material parameters: μ is a modulus-like parameter, λ_L captures the nonlinearity of the stress-strain response, and the six independent components of the fabric ellipsoid $\underline{G}_0$ represent the anisotropy of the distributed network.

---

[10] Appendix B presents another application of the effective stretch formulated from an exponential force-stretch relation.

3.4 Chapter summary

We presented a new approach to formulate a microstructurally-based orthotropic continuum models for the elastic response of distributed fiber networks in a framework motivated by experimental studies of nonwoven fabrics. For distributed networks in which the anisotropy of fiber orientation is combined with random entanglement processes, we proposed to capture the combined effects of fibers and junctions orientation distributions using a single tensorial representation of the network anisotropy (fabric ellipsoid), $\underline{G}_0$.

The fabric ellipsoid can be interpreted in terms of a micromechanical representation of a volume element of the network. This representation guided the derivation of the concept of an "*effective stretch*" of the network to be employed in the constitutive formulation. The concept of effective stretch was used in conjunction with a force stretch-relation for single fibers based on Langevin statistics to formulate a continuum orthotropic elastic model for the macroscopic response of the distributed network. The proposed model, termed JS-model, was shown to capture effects related to the distributed nature of the junctions and fiber orientations, and was favorably compared to the eight-chain orthotropic model proposed by Bischoff et al [12] and the directional model proposed by [25]. Though motivated by a mechanistic interpretation of the deformation mechanisms in nonwoven fabrics, the proposed framework is applicable to any materials with distributed network structures.

Chapter 4

A Continuum Model for Needlepunched Nonwoven Fabrics

The experimental results of the Dyneema Fraglight suggest that the governing deformation mechanisms of the fabric can be categorized into two parts: (1) an elastic part from re-orienting and stretching of constituent fibers, and (2) an inelastic part from time-dependent and irrecoverable mechanisms including permanent evolution of the web structure, and damage accumulated from inter-fiber friction and inter-fiber compaction. The two parts of deformation contribute to the overall deformation, and gives rise to the complex nonlinear elastic-inelastic behavior of this material. To account for the effects of each type of deformation mechanisms, we propose a constitutive model for nonwoven fabrics that consists of two constitutive components: a nonlinear spring representing the resistances to elastic deformation mechanisms, and a non-linear viscous dashpot representing the resistances to inelastic deformation mechanisms. The two constitutive components are connected in series, as shown by a rheological representation in Figure 4-1, to reflect the coupled effect of both types of deformations.

A full three-dimensional constitutive model following this rheological representation will be developed based on continuum mechanic framework. The discussion begins with a review on the general framework of finite deformation kinematics, kinetics, mechanical work, and dissipation inequality (the second law of thermodynamics), followed by a specialization of the framework to nonwoven fabrics. For additional reference on the theory of continuum mechanics, see Holzapfel

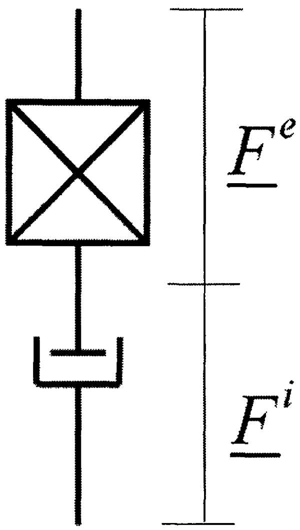

Figure 4-1: Rheological representation of the proposed fabric model

[41].

4.1 Continuum mechanics framework

4.1.1 Kinematics

A continuum body is assumed to deform in an affine manner, i.e., the deformations at the structural level follow a macroscopic deformation defined by a deformation gradient $\underline{F}$. Physically, the deformation gradient $\underline{F}$ serves as a one-to-one mapping function of a material point $\underline{X}$ in the reference state to its current (deformed) location $\underline{x}$;

$$\underline{F} = \frac{d\underline{x}}{d\underline{X}}. \tag{4.1}$$

The ratio of the deformed to the reference volume is given by $J = det(\underline{F})$. To relate the elastic and inelastic contributions to the overall deformation, the macroscopic deformation gradient $\underline{F}$ is multiplicatively decomposed into elastic and inelastic components consistent with the Kroner-Lee decomposition [41]:

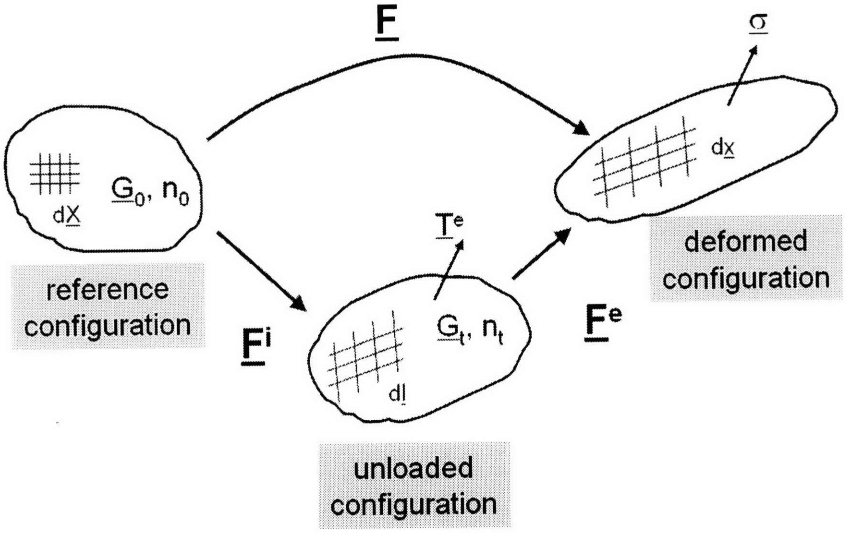

Figure 4-2: Multiplicative decomposition of the deformation gradient

$$\underline{F} = \underline{F}^e \underline{F}^i. \tag{4.2}$$

$\underline{F}^i$ represents a deformation of segments $d\underline{X}$ in the reference state to segments $d\underline{l} = \underline{F}^i d\underline{X}$ in the relaxed state due to dissipative mechanisms, and $\underline{F}^e$ represents a deformation of segments $d\underline{l}$ in the relaxed state to segments in the deformed configuration $d\underline{x} = \underline{F}^e d\underline{l}$ due to elastic mechanisms, see Figure 4-2. Hence, the inelastic deformation gradient representing the relaxed configuration can be obtained by elastically unloading the body to a stress free state. We define elastic and inelastic volumetric changes by

$$J^e = det\left(\underline{F}^e\right), \; J^i = det\left(\underline{F}^i\right), \text{ and } J^i J^e = J. \tag{4.3}$$

The right and left elastic and inelastic polar decompositions of $\underline{F}$ are given by

$$\underline{F}^e = \underline{R}^e \underline{U}^e = \underline{V}^e \underline{R}^e \text{ and } \underline{F}^i = \underline{R}^i \underline{U}^i = \underline{V}^i \underline{R}^i \tag{4.4}$$

where $\underline{R}^e$ and $\underline{R}^i$ are the elastic and inelastic rotations, $\underline{U}^e$, $\underline{V}^e$, $\underline{U}^i$ and $\underline{V}^i$ are the symmetric right and left stretch tensors for elastic and inelastic deformations, respectively.

The right Cauchy-Green tensor for the elastic deformation are defined by

$$\underline{C}^e = \underline{F}^{e^T} \underline{F}^e = \underline{U}^{e^2}. \tag{4.5}$$

The rate at which the material deforms is defined by a velocity gradient:

$$\underline{L} = \underline{\dot{F}}\underline{F}^{-1}. \tag{4.6}$$

From Equation 4.2, the velocity gradient can be decomposed into elastic and inelastic parts:

$$\underline{L} = \underline{L}^e + \underline{F}^e \underline{L}^i \underline{F}^{e^{-1}}, \tag{4.7}$$

where

$$\underline{L}^e = \underline{\dot{F}}^e \underline{F}^{e^{-1}}, \text{ and } \underline{L}^i = \underline{\dot{F}}^i \underline{F}^{i^{-1}}. \tag{4.8}$$

The velocity gradients can be further decomposed into stretch and spin:

$$\begin{aligned}
\underline{L} &= \underline{D} + \underline{W};\ \underline{D} = \frac{1}{2}\left(\underline{L} + \underline{L}^T\right);\ \underline{W} = \frac{1}{2}\left(\underline{L} - \underline{L}^T\right); && \text{(4.9a)}\\
\underline{L}^e &= \underline{D}^e + \underline{W}^e;\ \underline{D}^e = \frac{1}{2}\left(\underline{L}^e + \underline{L}^{eT}\right);\ \underline{W}^e = \frac{1}{2}\left(\underline{L}^e - \underline{L}^{eT}\right); && \text{(4.9b)}\\
\underline{L}^i &= \underline{D}^i + \underline{W}^i;\ \underline{D}^i = \frac{1}{2}\left(\underline{L}^i + \underline{L}^{iT}\right);\ \underline{W}^i = \frac{1}{2}\left(\underline{L}^i - \underline{L}^{iT}\right). && \text{(4.9c)}
\end{aligned}$$

where $\underline{D}$'s are the symmetric stretching tensors and $\underline{W}$'s are the skew-symmetric spin tensors. From Equation 4.8, the rate of change of the inelastic deformation gradient becomes

$$\underline{\dot{F}}^i = \underline{L}^i \underline{F}^i. \tag{4.10}$$

Eq 4.10 can be employed in a discretized explicit integration scheme to evolve the inelastic deformation gradient at each time increment; the elastic portion of the deformation gradient is then obtained from

$$\underline{F}^e = \underline{F}\underline{F}^{i^{-1}}. \tag{4.11}$$

4.1.2 Kinetics

Deformation gives rise to interactions between neighboring material points in the interior of the body. One of the consequences of such interactions is stress, a kinetic measure that describes the effects of external forces (tractions) onto the body. Following Cauchy's stress theorem, the external surface traction on a body in the current configuration, $\underline{t}$, is related to Cauchy stress, $\underline{\sigma}$, a symmetric second-order tensor describing the effects of the traction at every points inside the body, by:

$$\begin{aligned} \int\limits_{\partial\Omega} \underline{t}\; ds &= \int\limits_{\partial\Omega} \underline{\sigma}\underline{n} ds && \text{(4.12a)} \\ &= \int\limits_{\Omega} \operatorname{div}(\underline{\sigma})\, dv && \text{(4.12b)} \end{aligned}$$

where $\underline{n}$ is the direction of the outward surface normal, $\int\limits_{\partial\Omega} ds$ is the external surface of the body Ω, and $\int\limits_{\Omega} dv$ is its volume [1]. Following the kinematic description in Figure 4-2, the stress measures in the reference and the relaxed configurations can be obtained by the pull-back operation on the Cauchy stress;

$$\underline{T} = J\underline{F}^{-1}\underline{\sigma}\underline{F}^{-T} \text{ and } \underline{T}^e = J^e\underline{F}^{e^{-1}}\underline{\sigma}\underline{F}^{e^{-T}}, \tag{4.13}$$

where $\underline{T}$ is the symmetric second Piola-Kirchhoff stress defined in the reference configuration, and $\underline{T}^e$ is the equivalent measure defined in the relaxed configuration.

4.1.3 Rate of Mechanical Work

With reference to [41], the rate of internal mechanical work can be expressed in terms of the contraction between the Cauchy stress tensor and its conjugate rate of deformation integrated

---

[1] Eq 4.12a transforms to Eq 4.12b using divergence theorem.

over the entire volume in the current configuration;

$$W_{int} = \int \underline{\sigma} : \underline{D}\, dv. \tag{4.14}$$

Following the elastic-inelastic decomposition in Figure 4-2, the rate of internal mechanical work can be defined in the relaxed configuration by:

$$\begin{aligned} W_{int} &= \int \underline{\sigma} : \underline{D}\, dv = \int \underline{\sigma} : sym\left(\underline{L}^e + \underline{F}^e \underline{L}^i \underline{F}^{e^{-1}}\right) dv && (4.15a) \\ &= \int J^e \left(\underline{\sigma} : \underline{D}^e\right) dv^i + \int J^e \left(\underline{F}^{e^T} \underline{\sigma F}^{e^{-T}} : \underline{L}^i\right) dv^i && (4.15b) \\ &= \int \frac{1}{2}\left(\underline{T}^e : \dot{\underline{C}}^e\right) dv^i + \int \left(\underline{C}^e \underline{T}^e : \underline{L}^i\right) dv^i. && (4.15c) \end{aligned}$$

where $dv^i = J^{e^{-1}} dv$ is the differential volume defined in the relaxed configuration, and $\dot{\underline{C}}^e = 2\underline{F}^{e^T} \underline{D}^e \underline{F}^e$. The first term in Eq 4.15c denotes the rate of work done by the elastic deformation $\underline{F}^e$, while the second term denotes the work done by the inelastic deformation $\underline{F}^i$. For the system to satisfy the 2nd law of thermodynamics, the work done by the inelastic deformation must be dissipative, i.e.,

$$\underline{\Xi} : \underline{L}^i \geq 0. \tag{4.16}$$

Eq (4.16) is known as the local dissipation inequality, and the quantity $\underline{\Xi} = \underline{C}^e \underline{T}^e$ is commonly referred to as the Mandel stress.

4.2 Application to nonwoven fabrics

Needlepunched nonwoven fabrics can be treated as a continuum by means of homogenization of the network structure. Clearly, this approach is only appropriate for applications in which the characteristic length of the problem is much larger than the characteristic length of the fiber network, $d_{0.}$ In order to formulate a continuum model for the network response we introduce the following assumptions:

1) The junctions in nonwoven fabrics can be modeled as material points which displace in

an affine manner with the continuum.

2) The fabric texture can be captured through a single structural tensor $\underline{G}_t$ which evolves with time in an affine manner with the inelastic deformation $\underline{F}^i$. The fabric anisotropy in the unloaded configuration at time t can then be described by the fabric ellipsoid:

$$\underline{G}_t = \underline{F}^i(t)\,\underline{G}_0\underline{F}^{iT}(t). \tag{4.17}$$

3) the elastic response of the network can be obtained as proposed in the JS-model using the evolving structural tensor $\underline{G}_t$ in place of the structural tensor in the reference configuration, $\underline{G}_0$.

4) Fibers do not undergo any inelastic deformation, do not rupture and do not slip from the junctions, so that the number of fiber segments, the total fiber length in $\int\limits_{\Omega} dv$, and the average end-to-end unstretched length of fiber segments are considered constant.

We introduce the spectral representation of the network structure $\underline{G}_t$ as

$$\underline{G}_t = A_t\ \underline{e}_{t,A} \otimes A_t\ \underline{e}_{t,A} + B_t\ \underline{e}_{t,B} \otimes B_t\ \underline{e}_{t,B} + C_t\ \underline{e}_{t,C} \otimes C_t\ \underline{e}_{t,C}. \tag{4.18}$$

Analogously to the expressions 3.9, and 3.10 which apply in the reference configuration, the average end-to-end (unstretched) fiber length r_t in the unloaded configuration at time t can be expressed as:

$$r_t = \frac{1}{2} d_t \sqrt{A_t^2 + B_t^2 + C_t^2}, \tag{4.19}$$

where the characteristic network length, d_t is defined as the junction-to-junction distance of an equiaxial RVE with the same value of end-to-end (unstretched) fiber length r_t.

As a consequence of the 4th constitutive assumption $r_t = const = r_0$, the following condition is obtained:

$$\sqrt{A_t^2 + B_t^2 + C_t^2} = const = \sqrt{A_0^2 + B_0^2 + C_0^2}, \tag{4.20}$$

or, equivalently,

$$tr\left(\underline{G}_t\right) = tr\left(\underline{G}_0\right) = 3. \tag{4.21}$$

As the total number of fiber segments in $\int\limits_{\Omega} dv$, is constant and the volume in the unloaded configuration scales with the volumetric jacobian of the inelastic deformation, the number of fiber segments per unit volume, n_t, in the unloaded configuration evolves as:

$$n_t = \frac{1}{J^i} n_0. \tag{4.22}$$

Following the 3rd constitutive assumption, the 2nd Piola Kirchoff stress in the unloaded configuration is obtained as:

$$\underline{T}^e = \frac{n_t \eta}{tr\left(\underline{G}_t\right)} \frac{\lambda_L}{\lambda^e_{eff}} \left[\beta^e_{eff} \underline{G}_t - \beta_0 \underline{U}^{e^{-1}} \underline{G}_t \underline{U}^{e^{-T}}\right], \tag{4.23a}$$

where the elastic effective stretch is defined by $\lambda^e_{eff} = \sqrt{\frac{tr\left(\underline{F}^e \underline{G}_t \underline{F}^{eT}\right)}{tr\left(\underline{G}_t\right)}}$. The macroscopic Cauchy stress (i.e., stress in the current configuration), $\underline{\sigma}$, is calculated from 4.13, and is given by

$$\begin{aligned} \underline{\sigma} &= \frac{1}{J^e} \underline{F}^e \underline{T}^e \underline{F}^{e^T} && (4.24) \\ &= \frac{n_t \eta}{J^e tr\left(\underline{G}_t\right)} \frac{\lambda_L}{\lambda^e_{eff}} \left[\beta^e_{eff} \underline{F}^e \underline{G}_t \underline{F}^{e^T} - \beta_0 \underline{R}^e \underline{G}_t \underline{R}^e\right]. && (4.25) \end{aligned}$$

where n_t is given by 4.22. Using 4.3, and following the notation $\mu = n_0 \eta$ introduced in Chapter 3, the Cauchy stress can be expressed as:

$$\underline{\sigma} = \frac{\mu}{J tr\left(\underline{G}_t\right)} \frac{\lambda_L}{\lambda^e_{eff}} \left[\beta^e_{eff} \underline{F}^e \underline{G}_t \underline{F}^{e^T} - \beta_0 \underline{R}^e \underline{G}_t \underline{R}^e\right]. \tag{4.26}$$

To complete the constitutive formulation a framework for the evolution of the inelastic component of the deformation must be prescribed.

The experimental results from the uniaxial cyclic loading tests demonstrate that most of the fabric deformation is accommodated by irrecoverable mechanisms, as illustrated by the small elastic recovery in each loading cycle. Dominating inelastic mechanisms include irrecoverable evolution of the network structure, and damage accumulated from inter-fiber friction, and fiber slip from junction points. Consistently with the 4th constitutive assumption, the current formulation does not include effects related to fiber damage. The irrecoverable evolution of the network anisotropy is demonstrated by the tendency of constituent fibers to permanently align along the direction of applied load. For irrecoverable alignment to occur, the constituent fibers must overcome two types of resistances: (1) inter-fiber friction that provides resistance to relative sliding of the component fibers past each other, as the network realigns, and (2) a "volume exclusion" component which results from resistance to compaction at high levels of fiber volume fractions. It can be observed in the experiment that the 'rate' of structural evolution decreases as the fiber network becomes aligned along the tensile loading direction. The re-orientation of the network eventually terminates when the volumetric Jacobian of the inelastic deformation reaches a lower limit, related to the fiber volume fraction in the reference configuration.

Following the 2nd constitutive assumption, and 4.10, the rate of evolution of the structural tensor $\underline{G}_t$ and the inelastic velocity gradient in the unloaded configuration are related by:

$$\begin{aligned}
\dot{\underline{G}}_t &= \dot{\underline{F}}^i \underline{G}_0 \underline{F}^{i^T} + \underline{F}^i \underline{G}_0 \dot{\underline{F}}^{i^T} && \text{(4.27a)}\\
&= \underline{L}^i \underline{F}^i \underline{G}_0 \underline{F}^{i^T} + \underline{F}^i \underline{G}_0 \underline{F}^{i^T} \underline{L}^{i^T} && \text{(4.27b)}\\
&= \underline{L}^i \underline{G}_t + \underline{G}_t \underline{L}^{i^T}. && \text{(4.27c)}
\end{aligned}$$

In order to derive a relation motivated by the underlying physical mechanisms of texture evolution we cast the flow relationships in terms of the rate of change, $\dot{\underline{G}}_t$, of the structural tensor $\underline{G}_t$. This allows us to incorporate with ease the condition 4.21, which, in rate form, can be recast as

$$tr\left(\dot{\underline{G}}_t\right) = 0. \tag{4.28}$$

The constitutive prescription for the rate of change of the structural tensor $\underline{G}_t$ must be cast in an objective framework by introducing a relationship between an objective measure of the driving stress and the co-rotational (Jaumann) rate, $\overset{\nabla}{\underline{G}}_t$, of $\underline{G}_t$ [41],

$$\overset{\nabla}{\underline{G}_t} = \dot{\underline{G}}_t - \underline{\omega}\underline{G}_t + \underline{G}_t\underline{\omega}, \tag{4.29}$$

where $\underline{\omega}$ is a skew-symmetric tensor representing the structural spin. Because the fabric ellipsoid is taken to transform in an affine manner with the inelastic deformation, the structural spin is equivalent to the spin of the unloaded configuration of the continuum, i.e., $\underline{\omega} = \underline{W}^i$. The rotation associated with the relaxed configuration can be arbitrarily chosen (see e.g., Dafalias [24], Avaras [3]); in this formulation we consider a *spinless* relaxed configuration ([18], [28]), i.e., we prescribe:

$$\underline{W}^i = \underline{0}. \tag{4.30}$$

Consequences of this constitutive choice are

(1) the structural spin identically vanishes, $\underline{\omega} = \underline{0}$,

(2) the time derivative of the fabric ellipsoid is objective $\overset{\nabla}{\underline{G}_t} = \dot{\underline{G}}_t$, and

(3) the inelastic velocity gradient is symmetric $\underline{L}^i = \underline{D}^i$, so that 4.27c can be recast in the form:

$$\dot{\underline{G}}_t = \underline{D}^i\underline{G}_t + \underline{G}_t\underline{D}^i. \tag{4.31}$$

Note that 4.31 implicitly defines $\underline{D}^i$ in terms of $\dot{\underline{G}}_t$ and $\underline{G}_t$, so that, with the constitutive prescription 4.30, $\dot{\underline{F}}^i$ is univocally determined by prescribing $\dot{\underline{G}}_t$.

In general terms, a flow rule controlling the evolution of the fabric tensor can then be cast in the form:

$$\dot{\underline{G}}_t = \dot{\gamma}\underline{N}, \tag{4.32}$$

with $\dot{\gamma}$ being a scalar measure of the magnitude of the rate of evolution, and $\underline{N}$ its tensorial direction. Note that, consistently with 4.28, the tensor $\underline{N}$ must be deviatoric. Physically, we expect $\dot{\gamma}$ to scale with the magnitude of a "driving stress" and the direction $\underline{N}$ to be aligned to the direction of the stress deviator.

In order to identify an appropriate stress measure driving the evolution of $\underline{G}_t$, we consider now the dissipation constraint 4.16, which, for symmetric $\underline{L}^i$, becomes

$$\underline{\Xi} : \underline{D}^i \geq 0. \tag{4.33}$$

As 4.31 defines $\underline{D}^i$ only implicitly, we introduce an approximate measure for $\underline{D}^i$

$$\widetilde{\underline{D}}^i = \frac{1}{4}\left(\dot{\underline{G}}_t \underline{G}_t^{-1} + \underline{G}_t^{-1}\dot{\underline{G}}_t\right), \tag{4.34}$$

and impose the constraint:

$$\underline{\Xi} : \left(\dot{\underline{G}}_t \underline{G}_t^{-1} + \underline{G}_t^{-1}\dot{\underline{G}}_t\right) \geq 0, \tag{4.35}$$

or, equivalently,

$$\left(\underline{\Xi}\,\underline{G}_t^{-1} + \underline{G}_t^{-1}\underline{\Xi}\right) : \dot{\underline{G}}_t \geq 0. \tag{4.36}$$

We introduce

$$\underline{T}_{flow} = \frac{1}{2}\left(\underline{\Xi}\,\underline{G}_t^{-1} + \underline{G}_t^{-1}\underline{\Xi}\right), \tag{4.37}$$

as the stress measure driving the evolution of the fabric ellipsoid. Phenomenologically, this form also captures observable effects of the fabric anisotropy on structural evolution. To gain an intuitive understanding of this effect, consider a fabric ellipsoid $\underline{G}_t$ with $A_t >> B_t = C_t$, corresponding to a fiber network with a high degree of alignment along the $\underline{e}_A$ axis. Now consider two uniaxial loading configuration: (1) the first with the axial loading direction aligned with the $\underline{e}_A$ axis and (2) the second with the loading direction aligned with the $\underline{e}_B$ axis. For equal levels of axial stress in the two loading configurations, the rate of inelastic network realignment for configuration (2) will be substantially higher than the rate for configuration (1). Relationship 4.37 captures this effect, as for configuration (1) the driving stress will scale with $\frac{1}{A_t}$ and for configuration (2) the driving stress will scale with $\frac{1}{B_t}$.

We can therefore define the direction of $\dot{\underline{G}}_t$ as:

$$\underline{N} = \frac{dev\left(\underline{T}_{flow}\right)}{\left|dev\left(\underline{T}_{flow}\right)\right|}, \tag{4.38}$$

where $dev\left(\underline{T}_{flow}\right)$ is the deviator of the driving stress, and introduce a measure for the magnitude of the driving stress:

$$\tau = \frac{\left|dev\left(\underline{T}_{flow}\right)\right|}{\sqrt{2}}. \tag{4.39}$$

We propose a constitutive relationship for $\dot{\gamma}$ in the form:

$$\begin{aligned}
\dot{\gamma} &= \dot{\gamma}_0 \left(\frac{\tau - \tau_0}{S_t}\right)^m \left(\det \underline{G}_t - v \det \underline{G}_0\right);\ (\tau - \tau_0)\,\&\,(\det \underline{G}_t - v \det \underline{G}_0) > 0 && \text{(4.40a)}\\
\dot{\gamma} &= 0 \qquad ;(\tau - \tau_0) \leq 0 \text{ or } \{\det \underline{N} < 0\&\ \ (\det \underline{G}_t - v \det \underline{G}_0) = 0\} && \text{(4.40b)}
\end{aligned}$$

where $\dot{\gamma}$ is a dimensional constant with units [1/s]. In the following we provide a physical interpretation for the two factors in relationship 4.40:

$$\begin{aligned}
f_1 &= \left(\frac{\tau - \tau_0}{S_t}\right)^m && \text{(4.41a)}\\
f_2 &= \left(\det \underline{G}_t - v \det \underline{G}_0\right). && \text{(4.41b)}
\end{aligned}$$

The first term, f_1, is meant to capture the (nonlinear) dependence of the rate of structural evolution on the magnitude of the driving stress. This term relates to the contribution to the resistance to texture evolution arising from inter-fiber friction. The constitutive parameter τ_0 represents an initial (threshold) resistance to structural evolution corresponding to initial barriers to inter-fiber sliding[2]. The constitutive parameter m captures the nonlinearity of the dependence of the evolution rate on the driving stress. The factor S_t represents the material flow strength at time t. Experimentally, the resistance to network realignment increases with inelastic deformation. This effect is captured by introducing an evolution law for the strength parameter:

$$\dot{S}_t = \alpha \dot{\gamma}, \tag{4.42}$$

---

[2] In nonwoven fabrics these effects are related to surface treatments, coating, starching, etc.

so that

$$S_t = S_0 + \int_0^t \alpha\dot{\gamma}dt, \tag{4.43}$$

where S_0 and α are a material parameters, with S_0 representing the initial flow strength.

The second term, ${f_2}^3$, is meant to capture "volume exclusion" effects which result from resistance to compaction at high levels of fiber volume fractions. This term is cast in the simplest phenomenological form resulting in a complete cessation of structural evolution when the fiber network reaches a maximum level of compaction. Physically, the material parameter v is expected to scale with the initial volume fraction of fibers f_f in the reference configuration, with $1 > v > f_f$, reflecting the fact that the fiber network can never reach 100% compaction.

For the applications presented in this work, we only considered in-plane tensile loading and in-plane deformation of nonwoven fabric sheets with in-plane dimensions much larger than the specimen thickness. By direct imaging of the fabric structure 2-2 it is apparent that most of the constituent fibers are aligned in-plane. Consistently with typical fabrication processes for this kind of nonwovens[4], the thickness direction is one of the three principal directions of anisotropy. The associated principal value for the structural tensor $\underline{G}_t$ is usually an order of magnitude smaller than the principal values associated with the in-plane principal directions. Experimentally we note that the evolution of the fabric thickness (and of the corresponding component of the structural tensor which evolves in an affine manner with the continuum) with in-plane deformation is minimal. For efficiency of implementation, we therefore introduce a modified (2D) version of the proposed evolution law for the structural tensor $\underline{G}_t$, where we impose $C_t = C_0$ and $\underline{e}_C = \underline{e}_{0,C}$ at all t, and only consider the evolution of the planar component of the structural tensor:

$$\underline{G}_t^{2D} = A_t \; \underline{e}_{t,A} \otimes A_t \; \underline{e}_{t,A} + B_t \; \underline{e}_{t,B} \otimes B_t \; \underline{e}_{t,B}. \tag{4.44}$$

---

[3] Note that this term can also be written in terms of an inelastic volumetric jacobian J^i and a constant $\det \underline{G}_0$ by $(\det \underline{G}_t - v \det \underline{G}_0) = \det \underline{G}_0 \left(J^{i^2} - v\right)$.

[4] According to the manufacturer, and the parallel study on this fabric by Chocron et al. [23], the process to obtain this material is to cut short fibers of around 5cm, comb and stack them in several *layers*, and needle punched the layers to add structural rigidity.

For in-plane loading conditions, the Cauchy stress can be expressed as

$$\underline{\sigma} = \sigma_1\ \underline{e}_1^\sigma \otimes \underline{e}_1^\sigma + \sigma_2\ \underline{e}_2^\sigma \otimes \underline{e}_2^\sigma + 0\ \underline{e}_{t,C} \otimes \underline{e}_{t,C}. \tag{4.45}$$

where $\underline{e}_1^\sigma$ and $\underline{e}_2^\sigma$ are the principal stress direction in the $\underline{e}_A - \underline{e}_B$ plane.

These loading conditions, combined with the condition that the thickness direction is a principal direction of anisotropy[5], lead to a driving stress $\underline{T}_{flow}$ with non-zero components only in the plane of the fabric. We therefore introduce a 2D measure of the driving stress

$$\underline{T}_{flow}^{2D} = T_1^{2D}\ \underline{e}_1^T \otimes \underline{e}_1^T + T_2^{2D}\ \underline{e}_2^T \otimes \underline{e}_2^T. \tag{4.46}$$

with direction

$$\underline{N}^{2D} = \frac{dev\left(\underline{T}_{flow}^{2D}\right)}{\left|dev\left(\underline{T}_{flow}^{2D}\right)\right|}, \tag{4.47}$$

and magnitude

$$\tau^{2D} = \frac{\left|dev\left(\underline{T}_{flow}^{2D}\right)\right|}{\sqrt{2}}, \tag{4.48}$$

The rate of evolution of the planar structural tensor is then expressed as

$$\dot{\underline{G}}_t^{2D} = \dot{\gamma}\underline{N}^{2D}, \tag{4.49}$$

with

$$\dot{\gamma} = \dot{\gamma}_0 \left(\frac{\tau^{2D} - \tau_0}{S_t}\right)^m \left(\det \underline{G}_t - v \det \underline{G}_0\right)\ ;\ \left(\tau^{2D} - \tau_0\right) \,\&\, \left(\det \underline{G}_t - v \det \underline{G}_0\right) > 0 \tag{4.50a}$$

$$\dot{\gamma} = 0 \quad ;\ \left(\tau^{2D} - \tau_0\right) \leq 0 \ \text{ or } \left\{\det \underline{N} < 0 \text{ and } \left(\det \underline{G}_t - v \det \underline{G}_0\right) = 0\right\} \tag{4.50b}$$

---

[5] In this case all transverse shear components of the deformation gradients vanish.

Remarks

(1) The proposed formulation does not take into account two important factors in the evolution of textural anisotropy.

The first relates to processes of damage, breakage, and slip of individual fibers from junction points. These effects are limited in materials where the junctions are created by chemical or thermal bonding processes, but are pervasive in nonwovens in which the junctions are created by physical entanglement (e.g., needlepunching). Possible avenues to include these effects in the proposed constitutive framework, includes the introduction of an evolution equation for the average unloaded end-to-end length of fibers between junctions, which, in the current formulation would correspond to an evolution condition for $tr(\underline{G}_t)$, and a modified equation for the evolution of n_t, to ensure conservation of the total fiber length.

The second relates to the form of the resistance to compaction. In the proposed formulation, these effects are accounted for by the term f_2 in equation 4.41b and the corresponding condition on $\dot{\underline{G}}_t$, which sets the rate of change of $\underline{G}_t$ to zero when the fiber fraction reaches a maximum compaction level. These terms are isotropic in nature and do not capture the effects of anisotropy on the resistance to compaction. An extended formulation could account for these effects by introducing a tensorial back-stress, coaligned with the $\underline{G}_t$ tensor, reflecting the increased resistance to evolution along directions of high compaction. As a simpler alternative to this approach we can introduce an additional condition on the evolution of the principal values of $\underline{G}_t$, selectively arresting components of $\dot{\underline{G}}_t$ along principal directions for which a maximum compaction has been reached (while allowing continued evolution in the transverse plane following the 2D formulation presented above).

(2) This constitutive model requires a total of 13 parameters to completely describe the mechanical response of nonwoven fabrics:

- six parameters for the components of the fabric ellipsoid in the reference configuration: $\underline{G}_0$
- two parameters for the elastic component: μ, λ_L
- five parameters for the inelastic component: $m, \tau_0, S_0, \alpha, v$

Determination of the model parameters and its effect on the model response will be discussed in the following chapter.

4.2.1 Algorithm and Implementation

The constitutive model outline above has been implemented in a commercially available implicit finite element code ABAQUS/Standard via a user material subroutine UMAT. For this finite element code, the deformation gradient of each material point at an instantaneous time t is given as an input, and the time-integration algorithm in UMAT outputs the corresponding stress at each material point.

A time-integration algorithm for the finite element code UMAT is given as follows;

For each state of deformation, given

- deformation gradient of the current time step $\underline{F}_{t+dt}$
- structural tensor of the previous time step $\underline{G}_t$
- structural tensor flow rate of the previous time step $\dot{\underline{G}}_t$

Integration Procedure

1) explicitly update the structural tensor for the current time step $\underline{G}_{t+dt} = \underline{G}_t + \dot{\underline{G}}_t dt$
2) solve for the symmetric inelastic stretch $\underline{D}^i_t$ from (4.31)
3) obtain the deformation measures at time $t + dt$

    calculate $\underline{F}^i_{t+dt}$ from $\underline{F}^i_{t+dt} = \underline{F}_t + \underline{D}^i_t \underline{F}^i_t dt$ and $\underline{F}^e_{t+dt}$ from 4.11

4) obtain the network response $\underline{\sigma}_{t+dt}$ from 4.26
5) calculate the flow stress $\underline{T}_{flow}$ from 4.13 and 4.37
6) calculate the magnitude and direction of the flow rate from 4.40, 4.38
7) calculate the structural flow rate $\dot{\underline{G}}_{tt+dt}$ from 4.32

4.3 Chapter summary

This chapter presents a systematic approach for formulating a microstructurally-based anisotropic elastic-inelastic continuum model for nonwoven fabrics motivated by the fabric network structure and its underlying deformation mechanisms. For nonwoven fabrics in which the anisotropy of fiber orientation is combined with random entanglement processes, we proposed to capture the combined effects of fibers and junctions orientation distributions using a single tensorial representation of the network anisotropy (fabric ellipsoid). We relied on this structural measure to construct constitutive relations for the elastic and inelastic responses of nonwoven fabrics. The proposed model consists of a nonlinear elastic component representing the resistances to recoverable deformation mechanisms, and a non-linear inelastic component representing the resistances to irrecoverable deformation and texture evolution. This model requires 13 parameters to completely describe the fabric behavior: six of which define the network anisotropy at the reference state, two parameters capture the elastic response, and the remaining parameters control the evolution of the fabric texture.

Chapter 5

Model Validation and Verification

The constitutive model for needlepunched nonwoven fabrics formulated in the previous chapter is validated against the experimental findings presented in Chapter 2. We first discuss an approach to determine the model parameters from the fabric responses under uniaxial cyclic loadings along the principal material directions. With the fitted parameters, the model is used to simulate the fabric responses under (1) uniaxial monotonic loading along the off-principal directions, (2) 2-step uniaxial loading, and (3) equibiaxial tensile loading. Additional experimental data on the uniaxial tensile response of rectangular fabric strips is also presented as additional test for model validation. In comparing the model predictions to the experimental data, particular attention is given to the model ability to predict the complex nonlinear elastic-inelastic response as well as the evolution of fabric texture. The chapter concludes with a discussion on the model sensitivity to changes in the values of model parameters.

5.1 Determination of model parameters

The proposed fabric model requires 13 constitutive parameters to completely describe the fabric behavior:

- six parameters for the components of the fabric ellipsoid in the reference configuration: $\underline{G}_0$

- two parameters for the elastic response: μ, λ_L

- five parameters for the inelastic response: $m, \tau_0, S_0, \alpha, \upsilon$

The fabric ellipsoid is a tensorial measure of material anisotropy representing the combined effects of anisotropic fiber orientation distribution (FOD) and the resulting orientation distribution of junction-to-junction distances (JJD). Physically, the components of the fabric ellipsoid are directly related to the orientation distribution of junction-to-junction distances of the fabric texture. However, difficulties arise when measuring the JJD of the network with random junctions, e.g., Dyneema Fraglight, because of the limitations in the current image analysis techniques. As a result, the components of the fabric ellipsoid are currently determined by fitting the model simulations to the fabric response under uniaxial cyclic loadings along the principal material directions.

The two parameters for the elastic modeling component control the stiffness and the limiting stretch of the model response. The modulus-like parameter μ controls the stiffness at small deformation, whereas the locking stretch λ_L controls the nonlinearity of the response, particularly the transition from a compliant response at small deformation to a stiff response as the stretch of the fibers in the network reaches the extensibility limit described by the locking stretch λ_L. As it will be illustrated in Section 5.3, the locking stretch λ_L also controls the volumetric response of the model. Therefore, in selecting values for the elastic parameters of the model, the axial stiffness of the fabric response guides the selection of fitting values for μ, and λ_L, while the volumetric response is also taken into consideration in selecting an optimal λ_L value.

The three parameters for the inelastic component, including the initial barrier to flow τ_0, the initial flow strength S_0, and the linear coefficient to the evolution of flow strength α, are obtained by fitting the simulation predictions to the load-unload portions of the fabric response under uniaxial cyclic loading. The parameter v scales with the initial volume fraction of fibers, and directly controls the termination of the textural evolution. This parameter must be selected such that the volumetric response of the model matches with the level of compaction of the fabric texture observed in the experiment. The rate sensitivity parameter m was included in the model to extend its applicability to a broad range of strain rates. However, an investigation of strain rate effects was not a primary objective for this stage of model development, where all tests are conducted at similar quasi-static displacement rates. Within this limited range of application, we found that the inelastic constitutive response of the fabric could be well approximated by a quasi-linear dependence of the texture evolution rate on the driving stress. Therefore, we selected a value $m = 1.1$ for the rate sensitivity parameter. As further discussed in section 5.3, additional experimental investigation conducted on a broader range of strain rates might provide useful information to select a more appropriate value for this parameter.

In summary, all parameters can be obtained by fitting the simulation predictions to the fabric responses under uniaxial cyclic loadings along the in-plane principal directions (roll and cross). The relative stiffnesses of the two data sets can be fitted to obtain the modulus-like parameter μ, the locking stretch λ_L, as well as the in-plane components of $\underline{G}_0$. The out-of-plane component of $\underline{G}_0$ can be used as a free parameter to fit the volumetric response of the material. All other parameters for the inelastic component are obtained by fitting the load-unload response of these two data sets.

5.2 Model validation against experimental findings

The proposed fabric model is implemented in a commercially available implicit finite element code ABAQUS/Standard via a user material subroutine UMAT. The following model simulations were performed using eight-node brick elements (C3D8). Because the fabric thickness is not provided by the manufacturer, an averaged fabric thickness of 1.1 mm will be assumed for all simulations.

5.2.1 Simulations of fabric response under uniaxial tensile loads

To determine fitting values for the model parameters, two simulations are created to replicate the uniaxial cyclic loading test of the Dyneema Fraglight along the in-plane principal directions (R and C). The fitted model prediction and the corresponding experimental results are shown together in Figure 5-1, and the model parameters obtained from these simulations are presented in Table 5.1. Consistently with the notations used throughout this text, the $\underline{e}_A$-direction denotes the compliant in-plane direction (i.e. R-direction), the $\underline{e}_B$-direction denotes the stiff in-plane direction (i.e., C-direction) and the $\underline{e}_C$-direction denotes the out-of-plane direction of the fabric.

Good agreements between the fitted model predictions and the experiments in Figure 5-1 demonstrate the capability of the proposed model to capture the nonlinear elastic-inelastic

$\mu = 1e6$ Pa	$\lambda_L = 1.21$	
$G_{AA} = 0.654$	$G_{BB} = 2.307$	$G_{CC} = 0.039$
$G_{AB} = 0$	$G_{AC} = 0$	$G_{BC} = 0$
$\dot{\gamma}_0 = 0.0029$ 1/s	$m = 1.1$	$\tau_0 = 1e4$ Pa
$S_0 = 1e4$ Pa	$\alpha = 2.5e3$ Pa	$v = 0.25$

Table 5.1: Fitted model parameters obtained from uniaxial loading tests along principal directions (Roll = GAA, Cross = GBB)

response of the Dyneema Fraglight. In particular, the model captures the reorientation and stretch of the fiber network described by a compliant response at small strain followed by an increase in stiffness at large strain, respectively. The model also captures the increasing stiffness in each successive load-unload cycle. The inelastic mechanisms especially the irrecoverable evolution of network structure are also captured successfully, as indicated by a small elastic recovery in the unloading path. Note that the model over-predicts the stiffness of the fabric response in the roll direction at large deformation. This discrepancy arises because the deformation mechanism in this range is dominated by junction unraveling and fiber rupture; two of the inelastic mechanisms that are not considered in the current formulation.

To investigate the predictive capability of the proposed model to capture the effect of texture anisotropy, a series of simulations corresponding to the uniaxial monotonic loading tests of fabric strip along the roll (R), cross (C), needlepunch run (P), and perpendicular to the needlepunch run (X) directions are generated using the model parameters in Table 5.1. The input fabric ellipsoids for the simulations of the P- and X-directions are obtained by rotating the fabric ellipsoid in Table 5.1 by 30 degrees with respect to the C- and R-directions, respectively. The load per unit width and nominal strain plots of these simulations are shown to be in good agreements with their respective experimental findings until the effects of fiber slippage and junction unraveling dominate the fabric responses, see Figure 5-2.

In addition to the uniaxial tensile tests of the dogbone specimens, additional uniaxial tensile tests were conducted on rectangular fabric strips of 50.4 mm (2in) width and 101.6 mm (6in) gauge length using standard pincer grips. Because of the lateral constraint imposed by the standard pincer grips, the fabric specimen undergoes a complex mode of deformation described by a combination of tensile deformation due to the applied load and shear deformation induced by the grip constraint. The specimens are loaded at a nominal rate of 0.01 s^{-1} until failure.

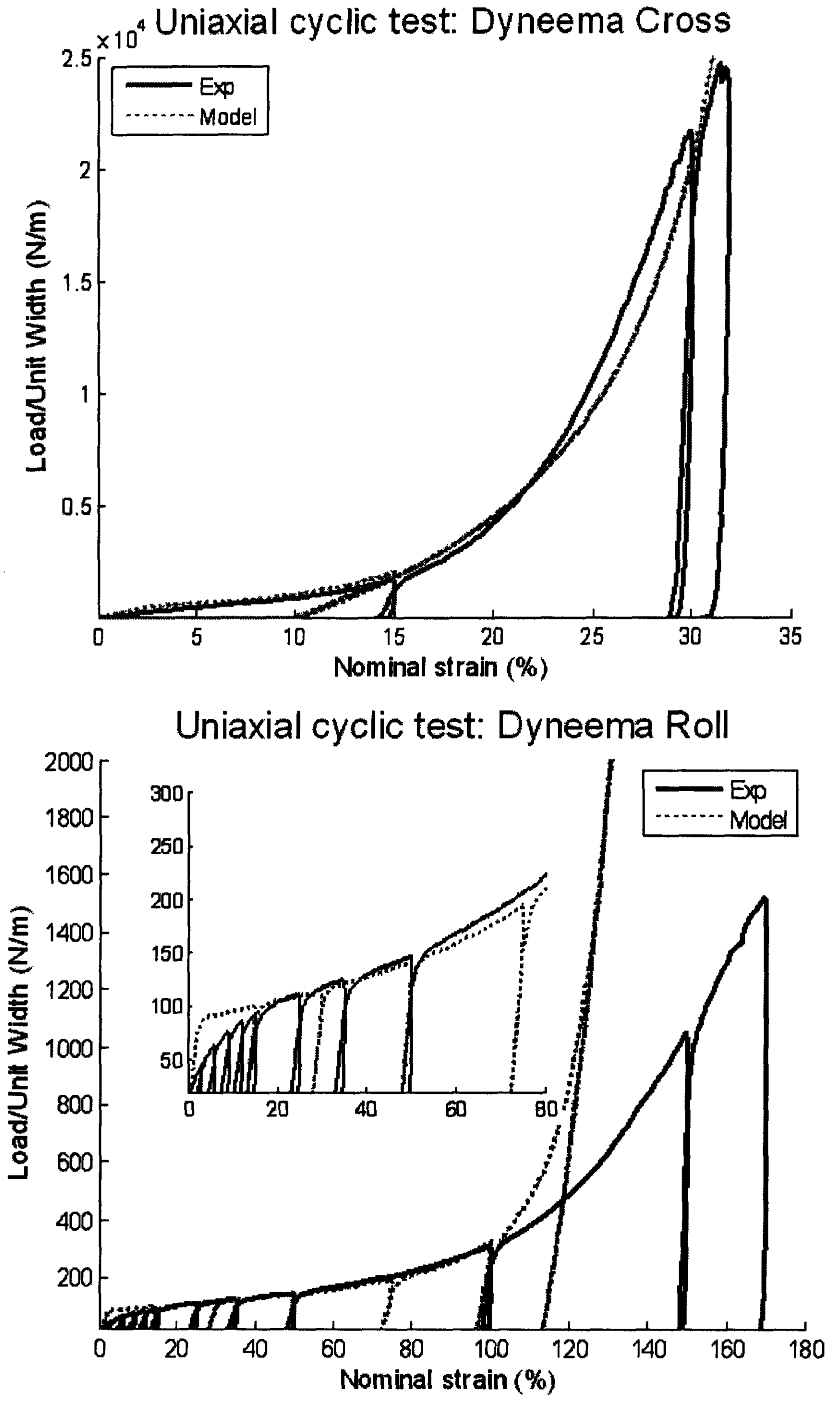

Figure 5-1: Fitted simulation prediction with the experimental data of the uniaxial cyclic loading test of the Dyneema Fraglight

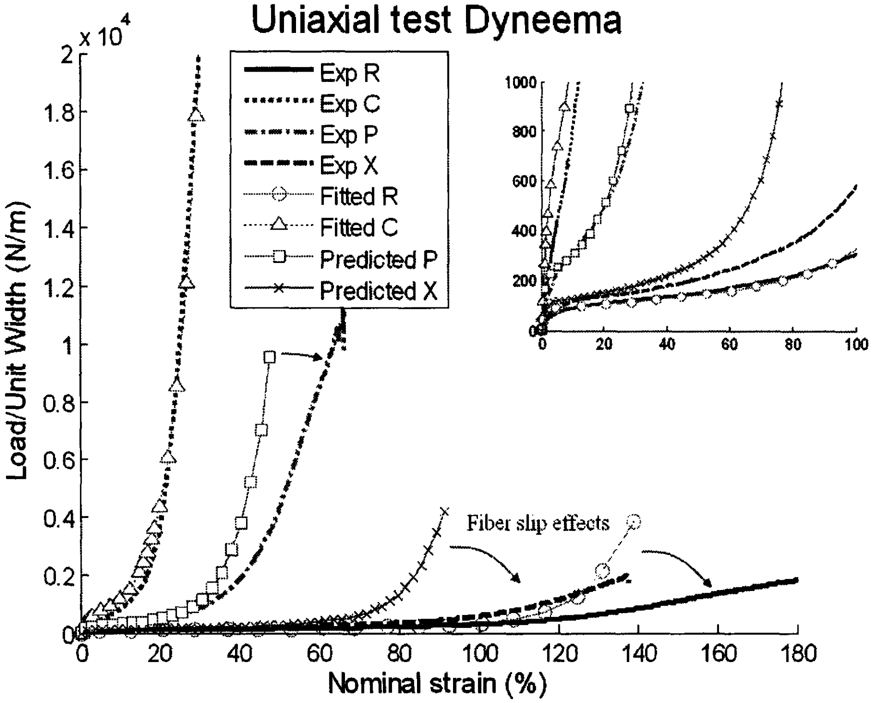

Figure 5-2: Model prediction of uniaxial monotonic loading tests along the C-, R-, P- and X-directions

An optical extensometer system is used to observe the deformation mechanisms of the fabric structure. These uniaxial strip tests are primarily used for validation of the model, especially in regards to the ability to capture the macroscopic deformation (deformed shape) as well as the evolution of fabric texture.

The model simulations of the rectangular fabric strip tests along the C-, R-, P- and X-directions are shown in Figure 5-3 to 5-6, respectively. In each of these figures, a set of three images is presented for each level of axial strain: the left image represents the fabric texture recorded from the experiment, the middle image shows the deformed shape of the simulation, and the right image shows the fabric texture predicted by the model. The fabric texture is represented by vector plots of the principal eigenvectors and eigenvalues of the fabric ellipsoids. The length of the eigenvectors indicates the relative magnitudes of the eigenvalues of the fabric ellipsoid in each principal direction. Because the fabric ellipsoids are related to the fiber orientation, the length of these vectors can be associated with the preferential alignment of the constituent fibers. Note that the images only illustrate half of the fabric strip because of the symmetric boundary condition. Therefore, the top edges of these images represent the center of the specimen, and the bottom edges represent the constrained boundary imposed by the grips.

Figure 5-3 to 5-6 show good agreements of the deformed shapes predicted by the model and the experimentally observed fabric configuration. The simulation along the C-direction shows a noticeable level of lateral contraction especially at the centerline of the specimen, in agreement with the experimental observation. On the other hand, the simulation prediction of the fabric response along the R-direction shows a uniform stress distribution throughout the fabric strip, except for a small region near the constrained boundary. The model also captures the development of lateral contraction at the centerline of the fabric strip as deformation progresses. The model appears to over-predict the lateral contraction in the R-direction at large deformation. This discrepancy arises because the effects of junction unraveling, which is experimentally identified as the dominant mechanism at this range of deformation, are not accounted for in the current formulation.

To validate the model capability in capturing the deformed shape, the lateral contractions of the centerline of the fabric strip from the experiments and the simulations are measured and compared. Figure 5-7 shows good agreements between the model predictions and the

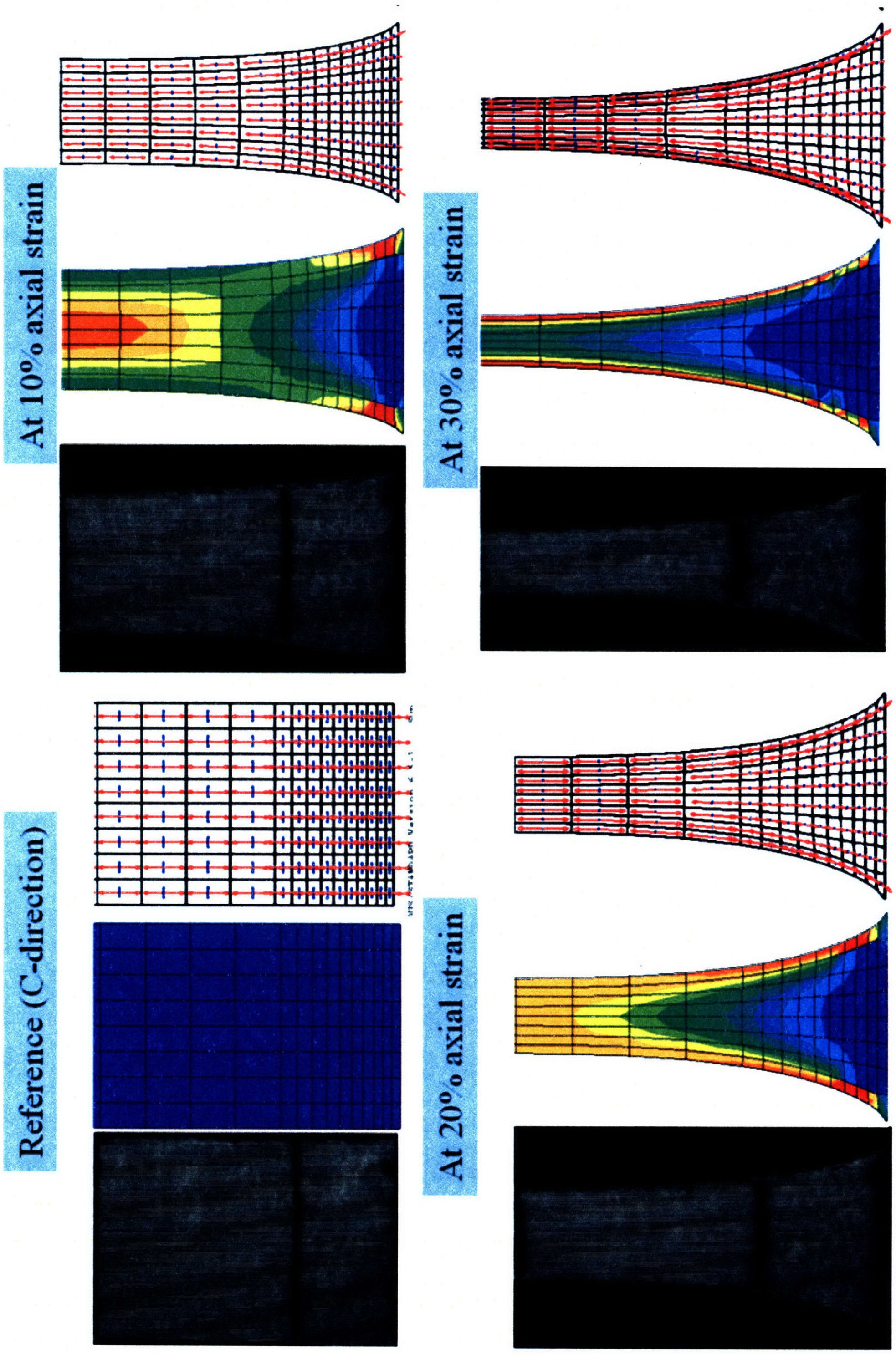

Figure 5-3: Model prediction of the deformed shape and the textural evolution of rectangular fabric strip under uniaxial tension along the C-direction

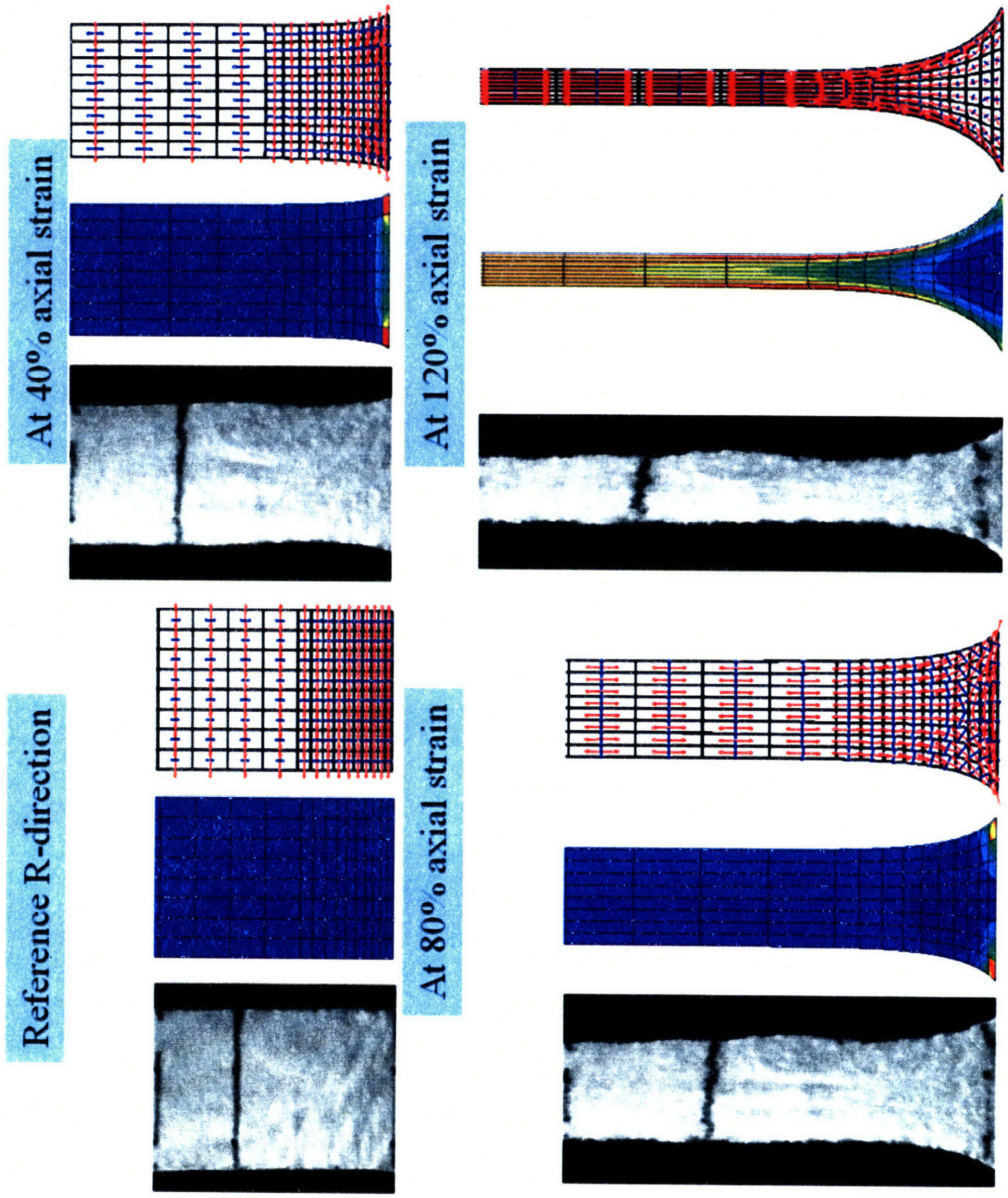

Figure 5-4: Model prediction of the deformed shape and the textural evolution of rectangular fabric strip under uniaxial tension along the R-direction

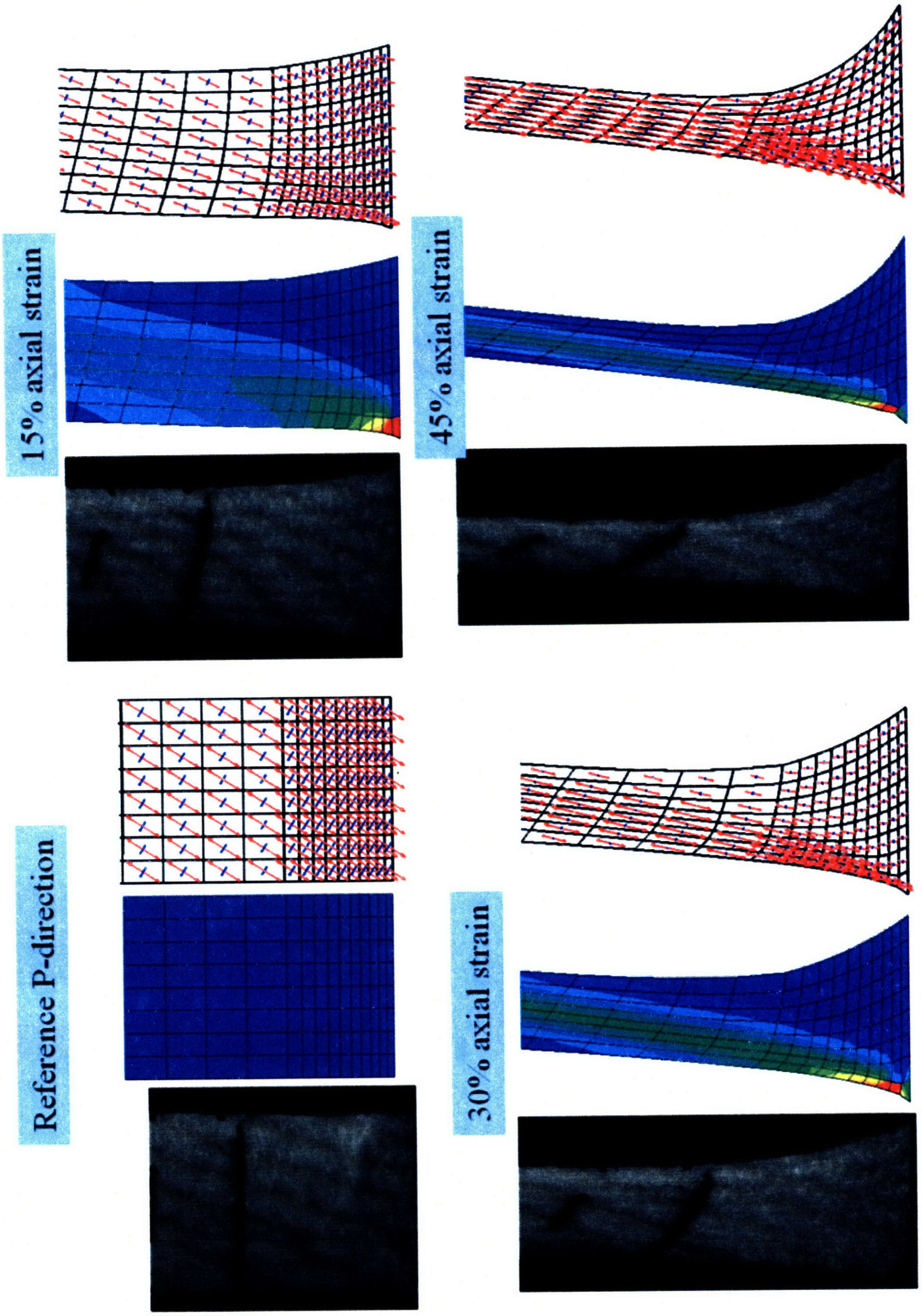

Figure 5-5: Model prediction of the deformed shape and the textural evolution of rectangular fabric strip under uniaxial tension along the P-direction

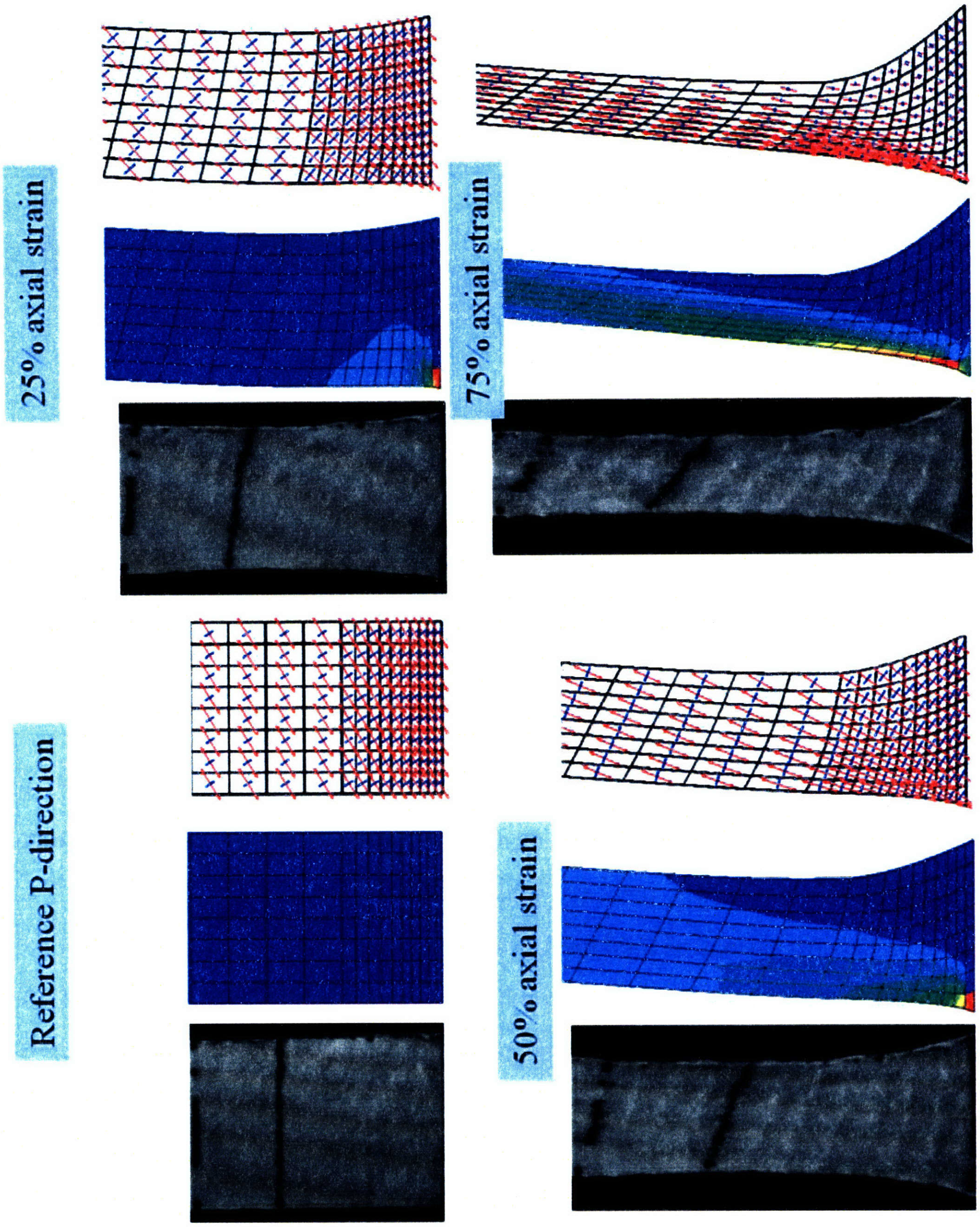

Figure 5-6: Model prediction of the deformed shape and the textural evolution of rectangular fabric strip under uniaxial tension along the X-direction

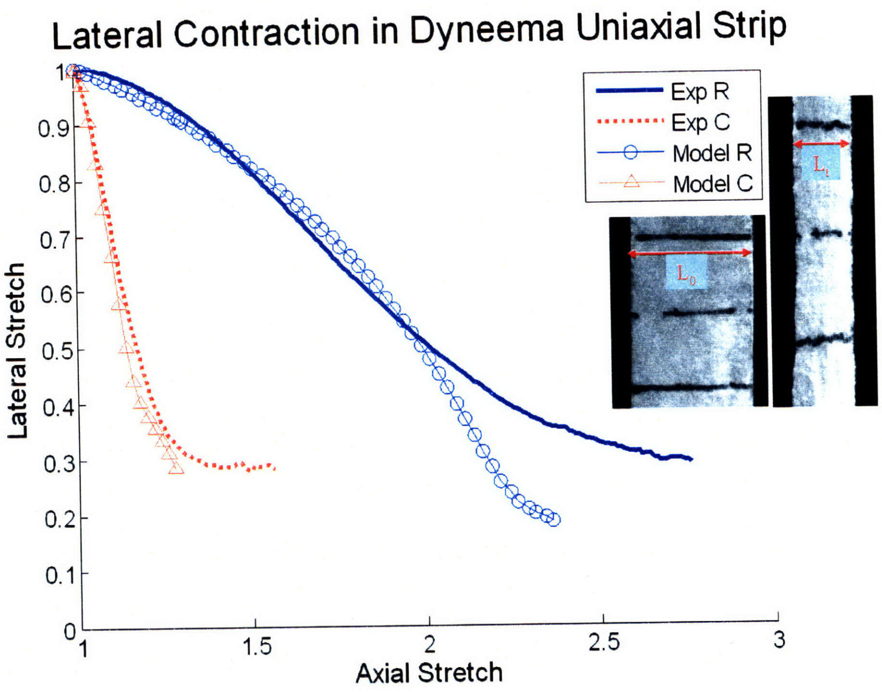

Figure 5-7: Experimental measurements and simulation predictions of the lateral contraction of the centerline in the rectangular strip specimen under uniaxial loading along the R- and C-directions

corresponding experimental measures of the lateral contraction of the centerline of the fabric strips, indicating that the model can accurately capture the macroscopic deformation of the fabric when loaded along the principal material directions.

The model simulations of the fabric loaded along the off-principal directions (i.e., P and X) indicate that the fabric deforms by a combination of tensile and shear deformations. The non-uniform stress distribution due to the combined tensile-shear effects can be observed in Figure 5-5 and 5-6. The model also predicts the regions of stress concentration near the constrained boundary, which is consistent with the effects of the lateral constraint imposed by the grips in the experiment.

Analogous to the lateral contraction of the centerline in the tests along the principal directions, the rotation of the centerline in the tests along the off-principal directions can be measured from the fabric images and the simulations. Figure 5-8 shows that the experimental data indicates larger differences between P- and X-directions than predicted by the model.

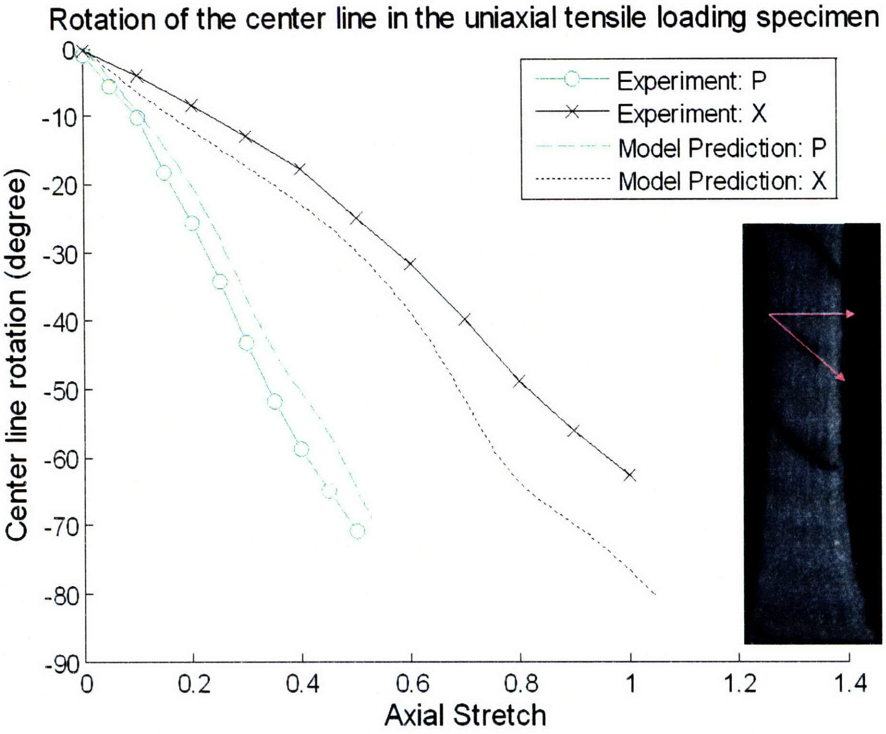

Figure 5-8: Experimental measurements and simulation predictions of the rotation of the centerline in the rectangular strip specimen under uniaxial loading along the P- and X- directions

This discrepancy can be attributed to fiber slip effects, or more possibly, to the approximations introduced by reducing the FOD and JJD to the second-order representation (Figure 2-5).

Figure 5-3 to 5-6 also demonstrate the capability of the model in capturing the evolution of fabric texture. At the reference state, the fabric texture along the principal directions is indicated by the fabric ellipsoid eigenvectors initially aligned with the loading direction. In comparison, the fabric texture along the off-principal directions (i.e., P and X) are indicated by a uniform distribution of rotated eigenvectors. In the simulation of the fabric strip test along the C-direction, the model predicts a highly anisotropic fabric texture biased along the loading direction. On the other hand, the model prediction of the uniaxial strip test along the R-direction illustrates an evolution of the fabric texture from one initially biased against the loading direction to a texture biased along the loading direction as the deformation progresses. At 120% axial strain along the R-direction, the model predicts a fabric texture that is almost

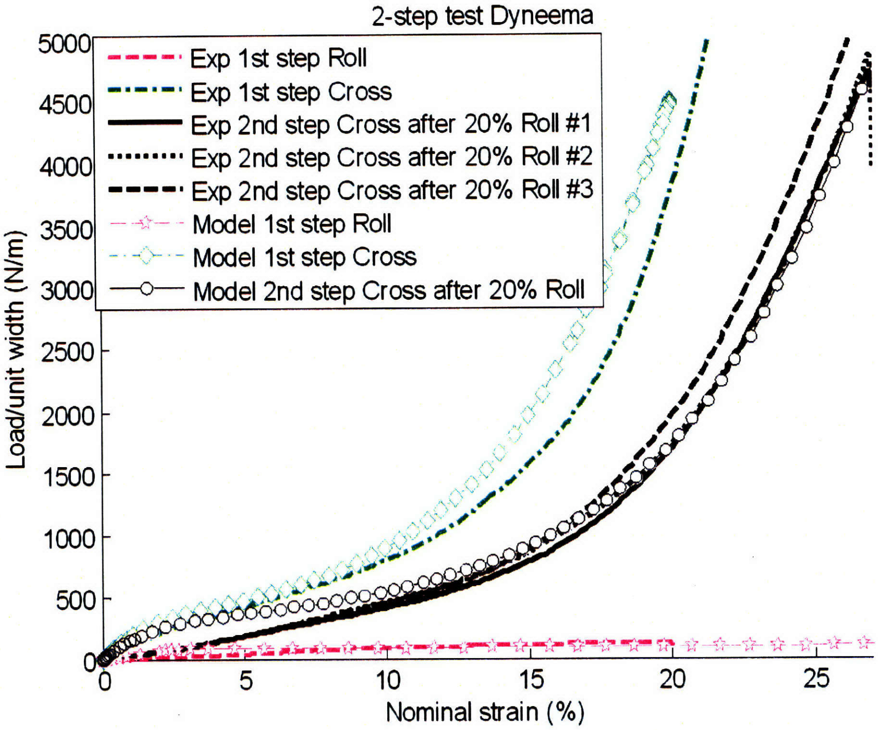

Figure 5-9: Model prediction of two-step uniaxial tensile experiment

completely aligned with the loading direction. The simulation predictions of both loading cases are in good agreements with the experimental observation.

The simulations of the fabric strips loaded along the off-principal directions show an evolution of the fabric texture that is accommodated by *stretching and reorienting* of the fabric ellipsoids. As the fabric ellipsoids re-orient along the load, the fabric undergoes shear deformation contributed by the biased alignment of the fabric texture with respect to the loading direction. Note that the rotation of the eigenvectors is accomplished by inelastic sliding and not by rigid body rotation, as evident when considering that the eigenvectors rotate counterclockwise while the material lines (mesh line) rotate clockwise.

The model capability in the macroscopic response of the Dyneema Fraglight is further validated by comparing the model simulation predictions and the experimental data of the two-step monotonic uniaxial loading tests. Recall that the fabric specimens in the two-step loading test have the same aspect ratio as those in the uniaxial monotonic loading tests. Therefore, the

	JJD from SSF model (G_{AA}:G_{BB})	JJD from the fabric simulation
Undeformed	1:1.9733	(fitted) 1:1.9365
after 20% Roll	1:1.6897	(predicted) 1:1.5594

Table 5.2: Comparison of the JJD obtained from the simplified straight fiber model and the JJD predicted by the simulation

simulation of the fabric response in the first loading step is identical to the simulation predictions of the monotonic loading tests. The simulation for the second loading step is carried out by using as starting level for the state variables (the fabric ellipsoid $\underline{G_t}$ and the flow strength S_t) the evolved values for these quantities obtained at the end of the first loading step. To be consistent with the test protocol, we simulated the model response in the first step along the roll direction up to 20% axial strain, and in the second step along the cross direction to 30% axial strain. The simulation predictions after the 2nd step is plotted together with the experimental data in Figure 5-9[1]. Good agreements between the model predictions and the experimental data in both loading steps confirms the model ability to predict the macroscopic response of this material under uniaxial tensile loadings.

Recall that the fabric texture after first loading step was thoroughly analyzed in Section 2.1.1. To validate the model ability to capture the evolving fabric texture, Table 2.4 is restated here with an additional column representing the ratio of the in-plane components of the fabric ellipsoid predicted by the model. The results in Table 5.2 indicate that the JJD approximated from the simplified straight fiber model exhibits the same trend as the JJD predicted by the model.

5.2.2 Simulations of fabric response under biaxial tensile loads

The proposed model is used to simulate the fabric response under equibiaxial tensile stretch using the fitted parameters from the simulations of uniaxial tensile tests. Figure 5-10 shows the schematic of the simulation for the biaxial tensile tests. The simulation results in Figure 5-11 show good agreements between the model predictions and the corresponding experimental data,

---

[1] Note that in predicting the 2-step uniaxial test, the model parameter corresponding to the resistance to network evolution, τ_0, has been changed to 1e2 instead of the fitted value of 1e4. This change was necessary because the fitted value was obtained from the experiments performed two years prior to the 2-step experiment, and the response of nonwoven fabrics, particularly the junction strength, are known to be degrading with time.

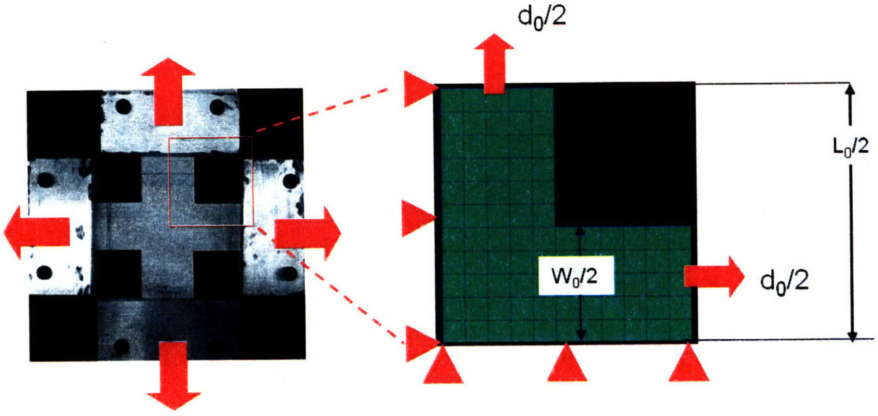

Figure 5-10: Biaxial tensile test configuration and model simulation

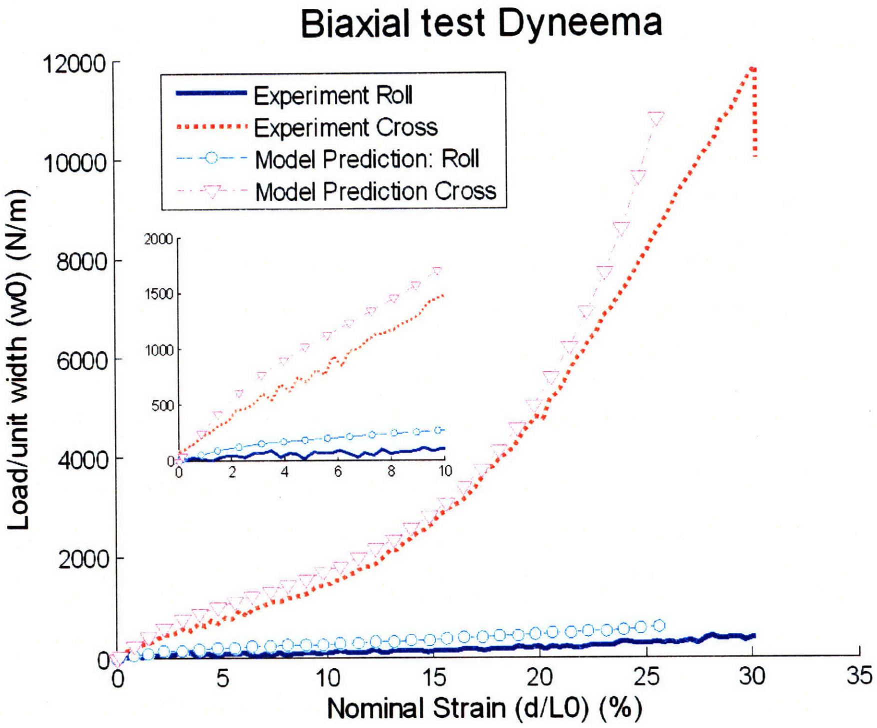

Figure 5-11: Experimental result and model prediction of equibiaxial tensile stretch experiment

especially the nonlinear anisotropic responses along both loading directions. Slight discrepancies of the model prediction at large displacement along both loading directions arise from the exclusion of fabric failure mechanisms, such as junction unraveling and fiber rupture, in the proposed model.

The model capability to capture the macroscopic deformed shape and the evolution of the fabric texture under biaxial tensile stretch is illustrated by a set of three images at each level of deformation in Figure 5-12 and 5-13. These figures show that the model can predict the macroscopic deformed shapes as well as the evolution of the fabric texture under biaxial tensile loading. In the reference state, the fabric texture is represented by a uniform fabric ellipsoid biased along the cross direction. As the deformation progresses, the fabric ellipsoids in the cruciform legs are stretched along their respective loading directions, while those at the center of the cruciform exhibit preferential alignment along the cross (stiff) direction. The fabric ellipsoids at the boundary of the roll direction and the center of the cruciform specimen undergo both rotation and stretch, resulting in a biased fabric texture similar to the constrained boundary of the uniaxial tensile simulations along the off-principal directions. This complex texture evolution predicted by the model is in good agreement with the deformed fabric texture observed in the experiment.

The model is further validated for its capability to capture the evolution of the fiber orientation. Figure 5-14 shows a series of images illustrating the fabric texture at each level of deformation. In this figure, the images in the first row represent the experimentally observed fabric texture. The images in the second row represent the contour plots of fiber orientation obtained by the image analysis algorithm for fiber orientation distribution ([42], section 2.1.1). The images in the third row represent the contour plots of the principal values of the fabric ellipsoid with respect to the cross direction ($\underline{e}_B \cdot \underline{G}\underline{e}_B$). In the contour plots of this figure, the green (light) area corresponds to the preferential alignment of the fibers along the roll direction, while the red (dark) area represents a preferential alignment of the fibers along the cross direction. Figure 5-15 shows the model prediction of the fiber orientation distribution and the experimentally observed fabric texture after 30mm crosshead displacement (d_0). Good agreements between the model prediction of the fiber orientation and the fiber orientation distribution measured from the experiment confirm the model capability to capture the evolution

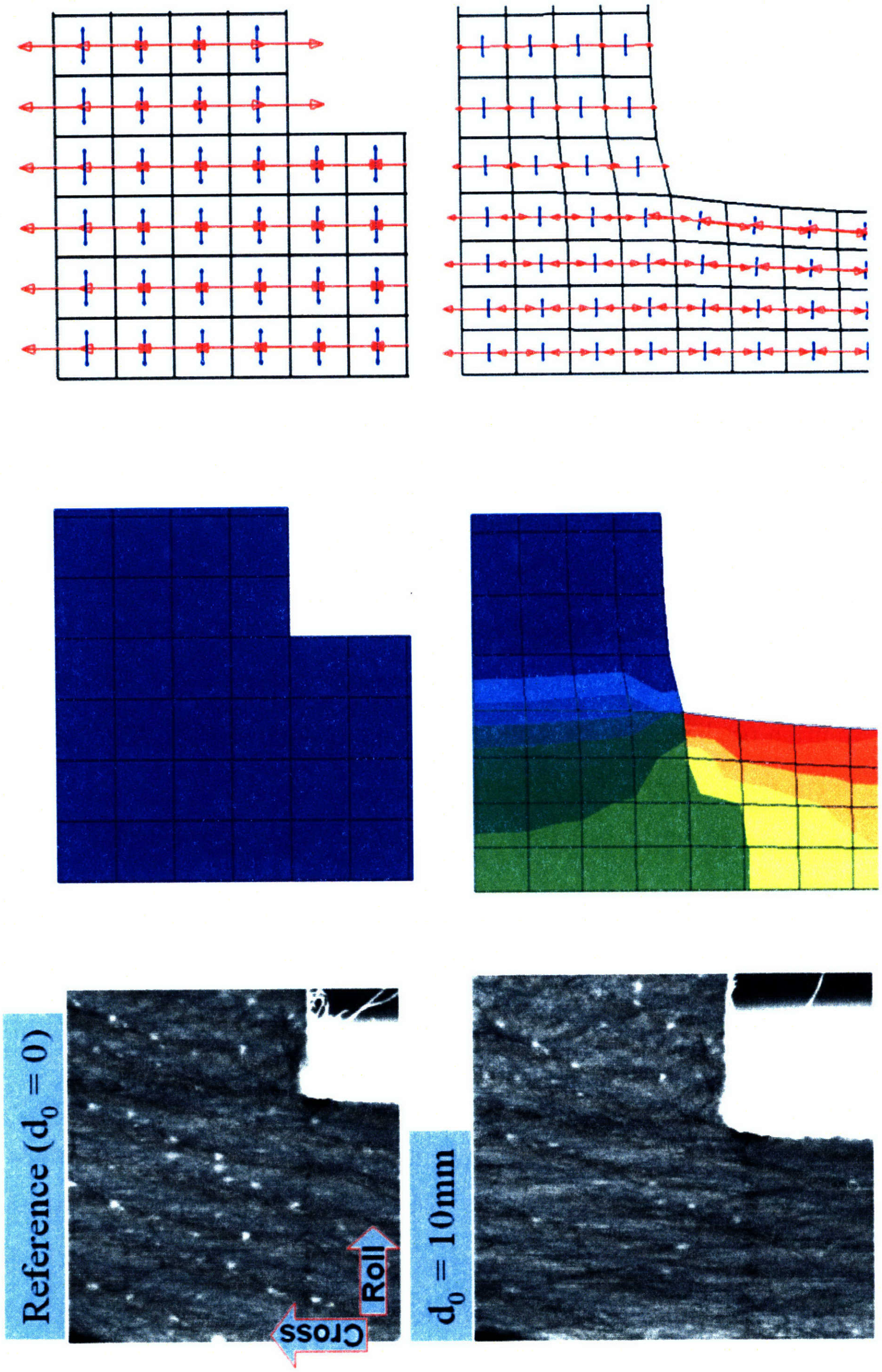

Figure 5-12: Model prediction of fabric texture under equibiaxial stretch (1)

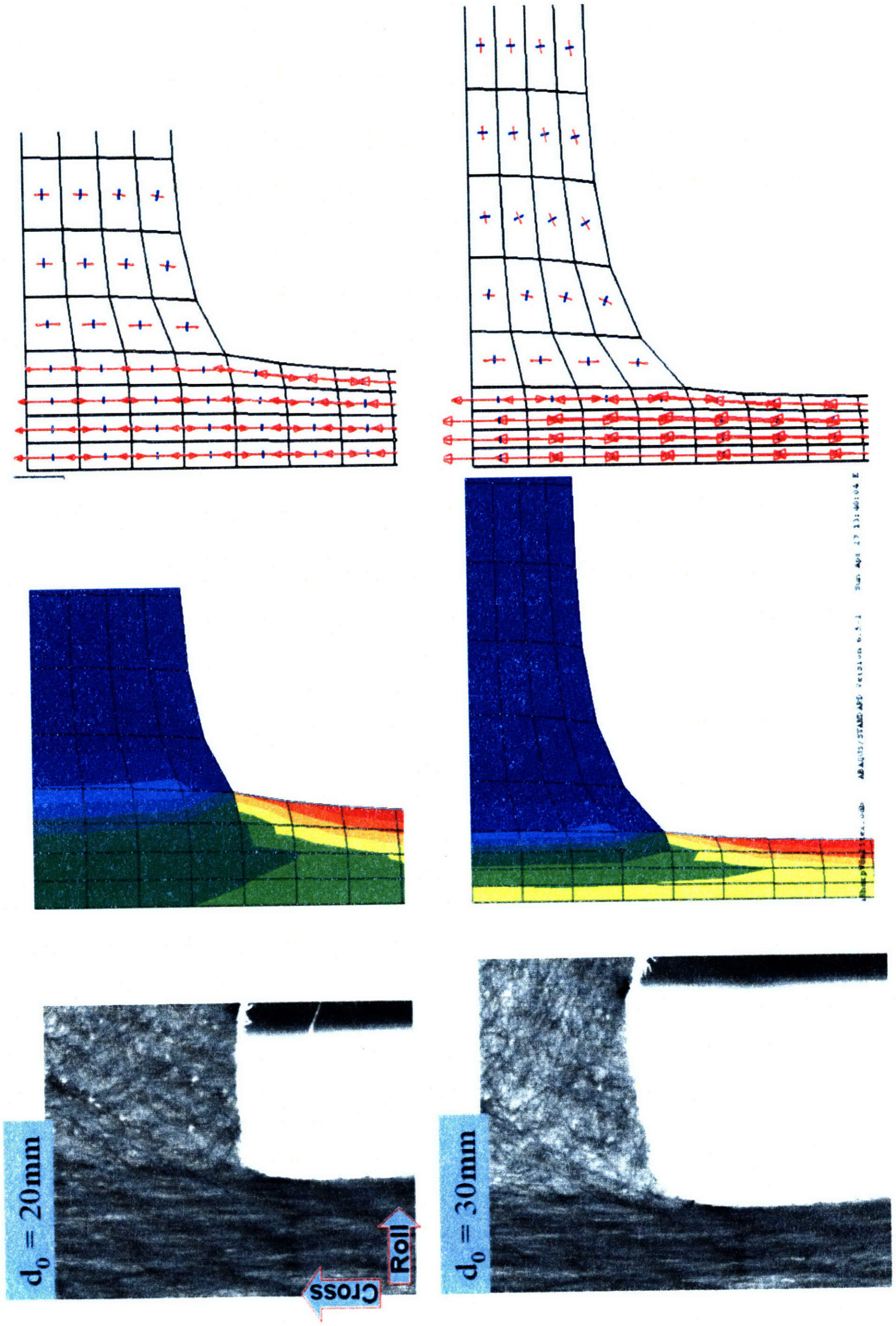

Figure 5-13: Model prediction of fabric texture under equibiaxial stretch (2)

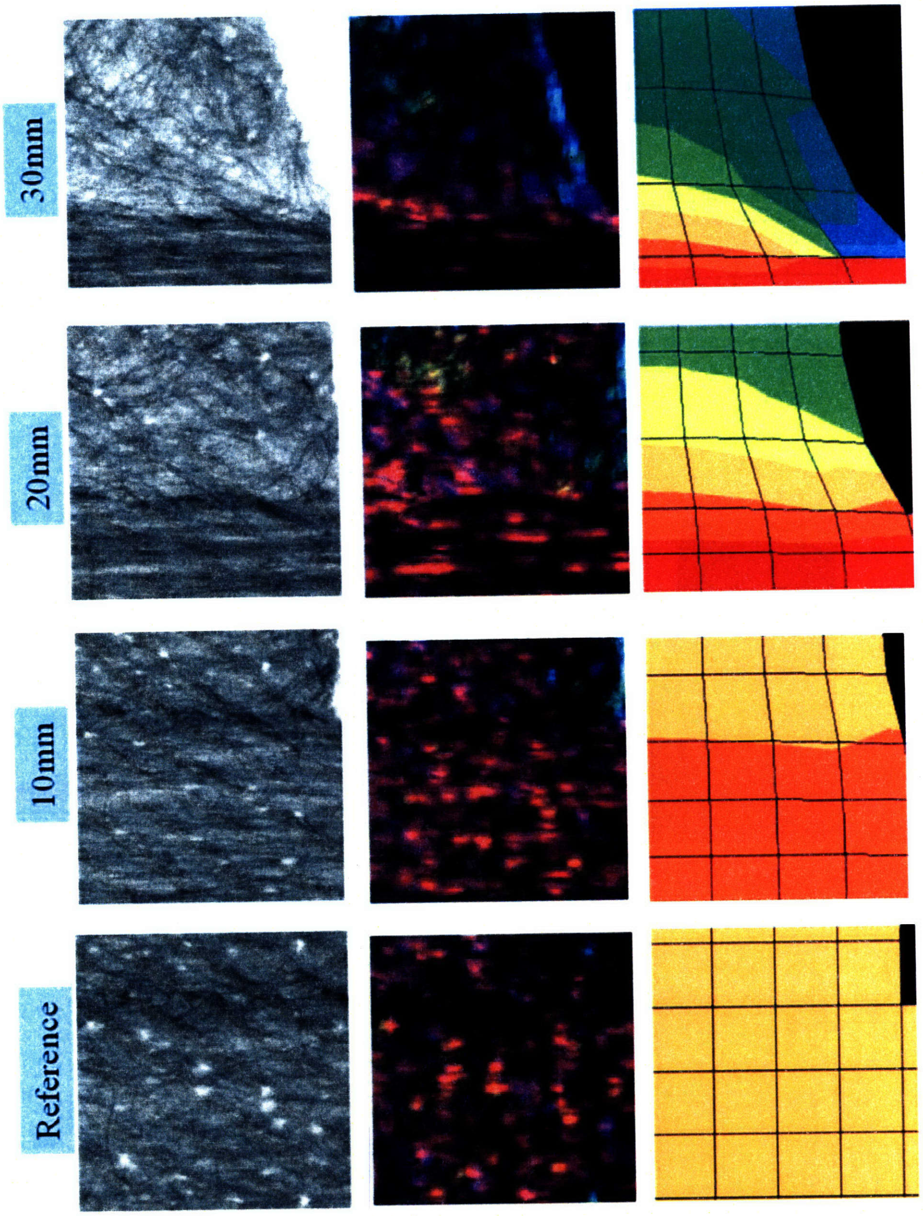

Figure 5-14: Evolution of fiber orientation distribution in the fabric under biaxial tensile loading

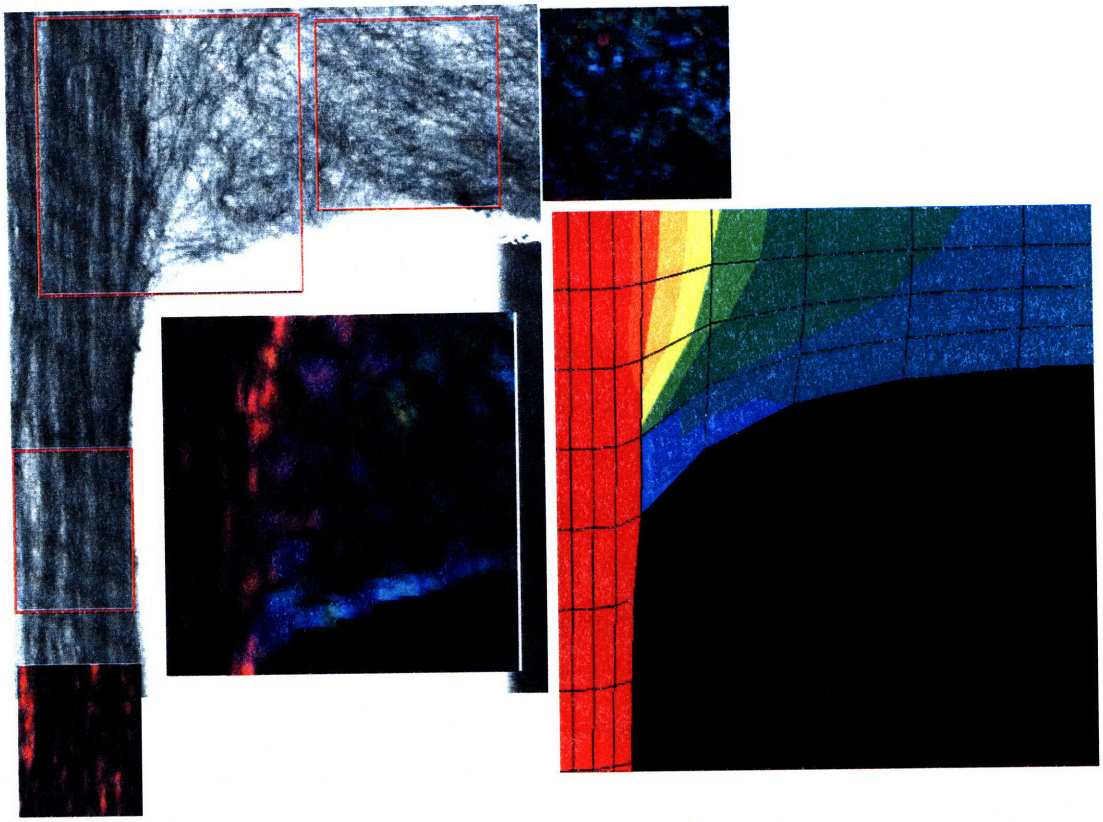

Figure 5-15: Fiber orientation distribution observed in the experiment and the corresponding model prediction

of fabric texture.

5.3 Sensitivity analysis

To investigate the effects on the model behavior due to variations in each material parameter, the model is analyzed using a sampling-based sensitivity analysis. Recall that the proposed constitutive model requires 13 parameters to completely describe the fabric behavior: μ, and λ_L control the nonlinear stress-strain response, m, τ_0, S_0, α,and v specify the structural evolution as well as the load-unload behavior, and six components of the fabric ellipsoid in the reference state $\underline{G}_0$ describe the orthotropic network texture. The sensitivity analysis is performed by perturbing each of the model parameters in Table 5.1, and studying its effect on the model response under uniaxial tensile simulation. Each parameter controls different aspects of the model response, and therefore, the sensitivity analysis focuses on part of the model response where the effects of the parameter dominate. The sensitivities of μ, λ_L, and v are analyzed from the model response under monotonic loading along the in-plane principal directions. The volume response for variations in λ_L and v under this loading condition is also evaluated because these two parameters directly affect the volumetric response of the model. For the remaining inelastic parameters (m, τ_0, S_0, α), the analyses focus on the load-unload response of the model under uniaxial cyclic loading along the in-plane compliant direction, because the deformation in this case is dominated by inelastic mechanisms, particularly the evolution of fabric texture. The model sensitivity on the components of the fabric ellipsoid in the reference state is investigated by comparing the model response under uniaxial monotonic loading at different levels of anisotropy.

5.3.1 Model sensitivity to the parameters of the elastic component

The two parameters for the elastic component control the stiffness of the model response. The modulus-like parameter μ controls the stiffness at small deformation, whereas the locking stretch λ_L controls the nonlinearity of the response, particularly the transition from a compliant response at small deformation to a stiff response as the stretch of the fibers in the network reaches the extensibility limit described by the locking stretch λ_L. The model sensitivity due to variations in the modulus-like parameter μ is shown in Figure 5-16 for the uniaxial response along the in-plane stiff ($\underset{\sim}{e}_B$) direction and along the in-plane compliant ($\underset{\sim}{e}_A$) direction. Similar plots for the locking stretch are presented in Figure 5-17. Note that a perturbation in μ produces a proportionated change in the axial stiffness (i.e, increasing $\mu \rightarrow$ increasing axial stiffness), whereas a perturbation in the locking stretch causes an adverse shift in the nonlinear transition of the model response (i.e., increasing $\lambda_L \rightarrow$ decreasing axial stiffness). The effects of these parameters are discernible at large deformation where the contribution of the elastic component dominates that of the inelastic component.

In addition to the axial stiffness, a variation in the locking stretch leads to a change in the model volumetric response. Figure 5-18 shows a plot of the volumetric strain and axial strain with various degrees of locking stretch. The result shows that a decreasing locking stretch results in an increasing bulk compressibility. The results from Figure 5-17 and 5-18 indicate that the locking stretch not only controls the nonlinearity of the axial stiffness, but also governs the bulk response of the model.

5.3.2 Model sensitivity to the parameters of the inelastic component

Recall from Equation 4.40 that the magnitude of the rate of evolution of fabric texture, $\dot{\gamma}$, can be physically interpreted as a combination of two contributions:

$$f_1 = \left(\frac{\tau - \tau_0}{S_t}\right)^m \tag{5.51a}$$

$$f_2 = \left(\det \underset{\sim}{G}_t - v \det \underset{\sim}{G}_0\right). \tag{5.51b}$$

The f_1 term relates to the contribution to the resistance to texture evolution arising from inter-fiber friction. This term captures the nonlinear dependence of the rate of structural evolution on the magnitude of the driving stress, and its contribution can be directly related to the load-unload behavior of the model. Therefore, the model sensitivities to the four parameters τ_0, S_0, α, and m controlling the magnitude of the f_1 term can be described by examining the model response under uniaxial cyclic loading.

The constitutive parameter τ_0 represents an initial (threshold) resistance to structural evo-

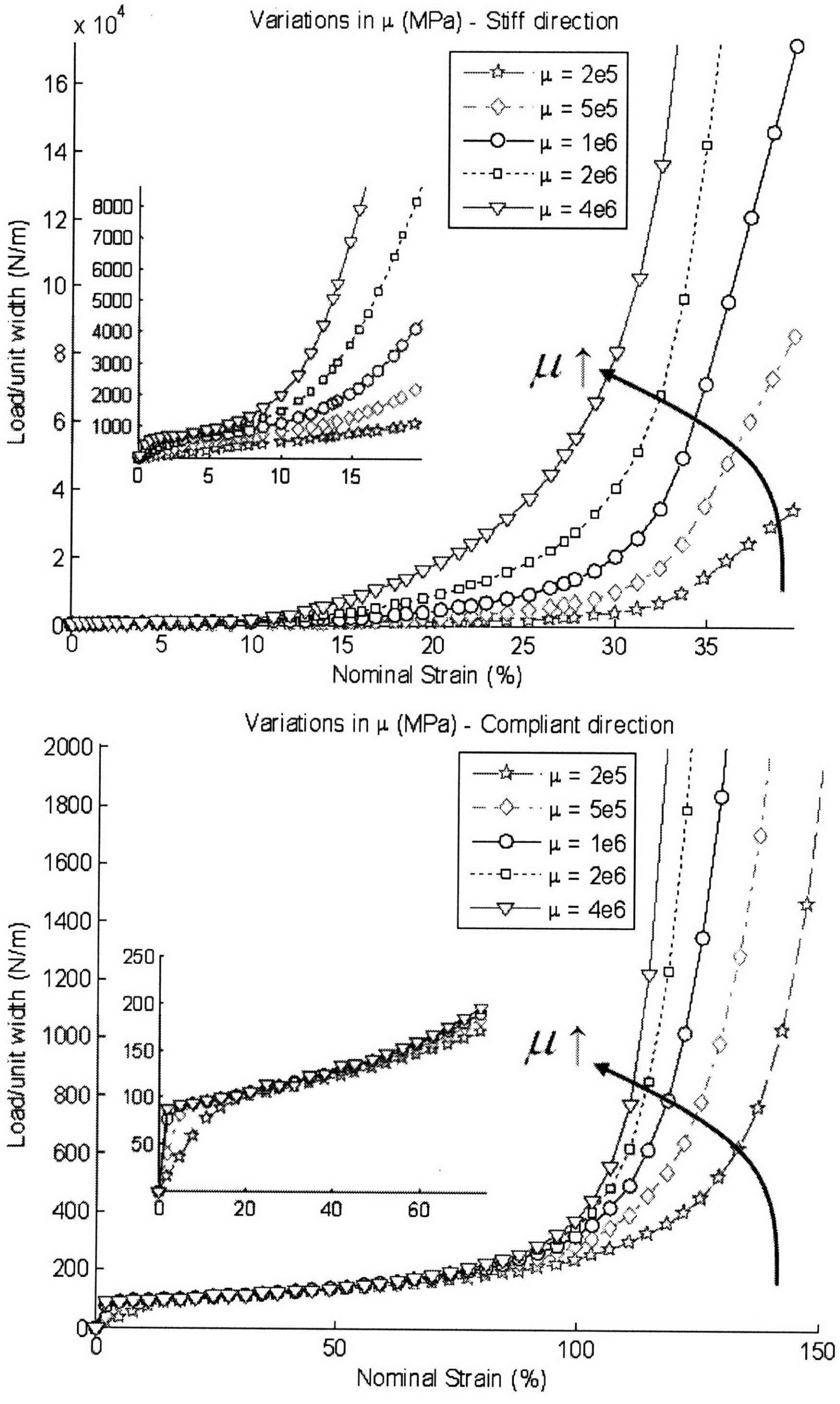

Figure 5-16: Model sensitivity due to variations in μ

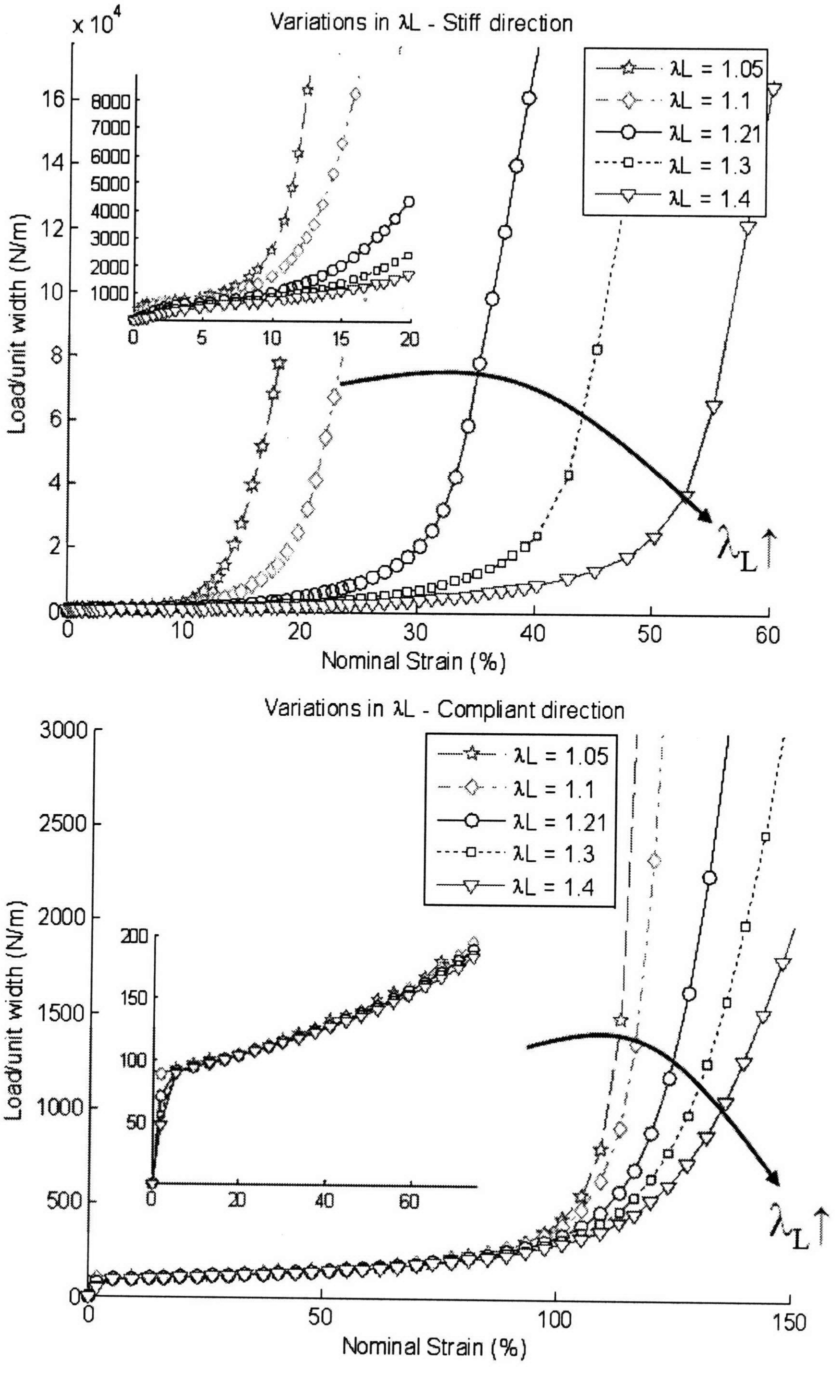

Figure 5-17: Model sensitivity due to variations in λ_L

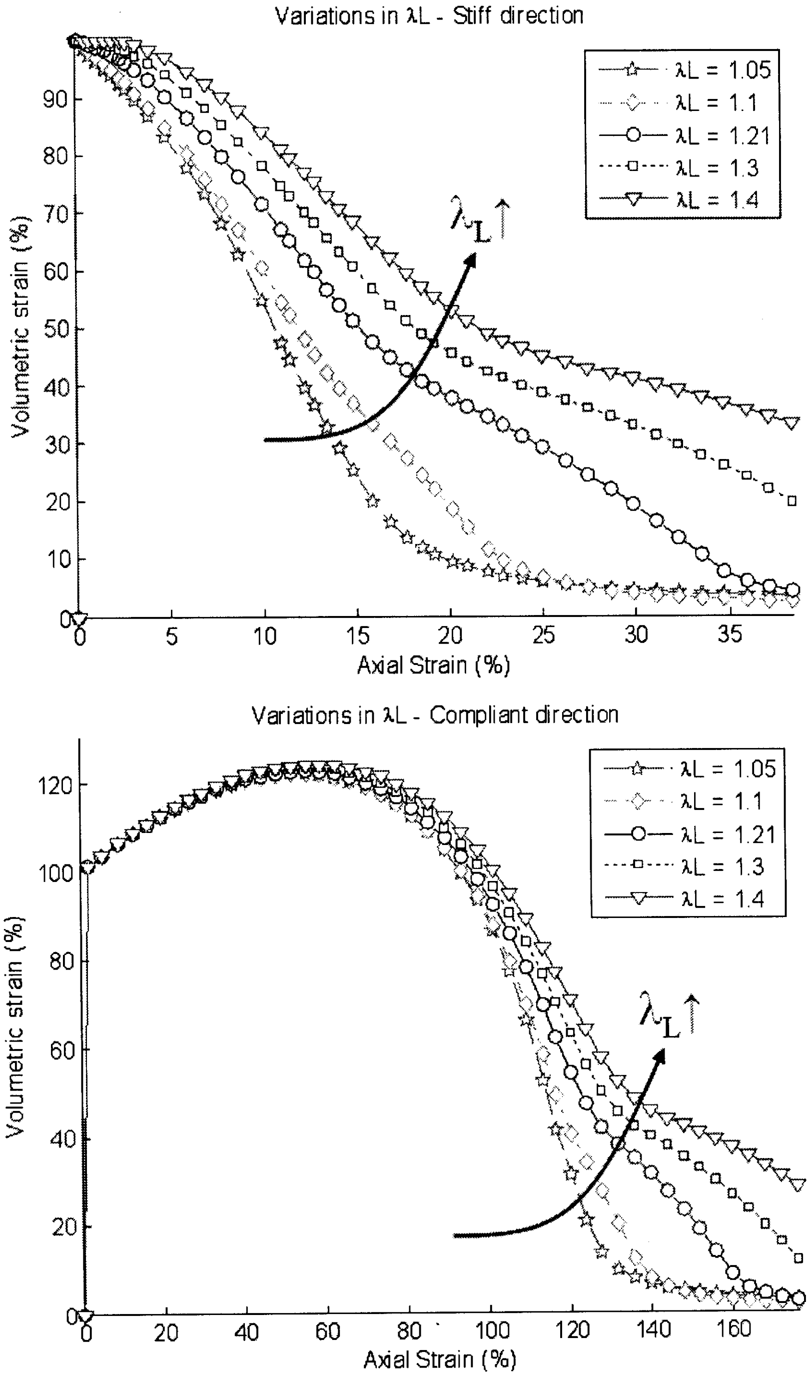

Figure 5-18: Volumetric effect due to variations in λ_L

lution corresponding to initial barriers to inter-fiber sliding. As shown in Figure 5-20, the parameter τ_0 controls the onset of textural evolution. Note that a variation in τ_0 does not directly influence the load-unload behavior, because the rate of the structural evolution is controlled by the flow strength S_t, the strain rate-sensitivity parameter m, and the difference between the magnitude of the driving stress the threshold resistance $(\tau - \tau_0)$.

The initial flow strength S_0 and the coefficient to the rate of flow strength α directly control the material flow strength S_t. Because the flow strength S_t inversely scales with the rate of the textural evolution, an increase in either S_0 or α results in a decrease in the structural evolution rate. Consequently, the model response exhibits an increase in the axial stiffness as the contribution to the overall deformation from the inelastic component decreases. Figure 5-21 shows that the initial flow strength S_0 governs the load-unload behavior as well as the onset of the textural evolution. In comparison, Figure 5-22 shows that the coefficient to the rate of the flow strength α directly scales with the axial stiffness when the model response is dominated by the inelastic deformation.

The constitutive parameter m captures the nonlinearity of the dependence of the evolution rate on the driving stress. To illustrate the effects of m, two simulations of the uniaxial cyclic loading tests along the in-plane compliant direction are created using the parameters in Table 5.1 with two variations: (1) $m = 2$ and $\tau_0 = 7e3$, and (2) $m = 4$ and $\tau_0 = 5e3$. Figure 5-19 shows that the model predicts overly similar responses for both sets of parameters when simulating at a loading nominal strain rate of 0.01 s^{-1}. However, when simulating loading at a nominal strain rate of 0.1 s^{-1}, the simulation predictions of the two sets diverge, and the simulation of set (1) appears to be stiffer than that of set (2). In another word, the constitutive parameter m reflects the dependence of the model response on the rate of deformation. The model response is highly sensitive to the rate of deformation for low values of m, and becomes less sensitive as m increases.

The f_2 term in the magnitude of the rate of evolution is designed to capture the volume exclusion effect. The contribution of the f_2 term is independently controlled by the constitutive parameter v, which specifies the termination of the structural evolution when the fiber network reaches a maximum level of compaction. In contrast to the f_1 term, the f_2 term primarily serves as a scaling factor to the rate of the structural evolution and does not contribute to

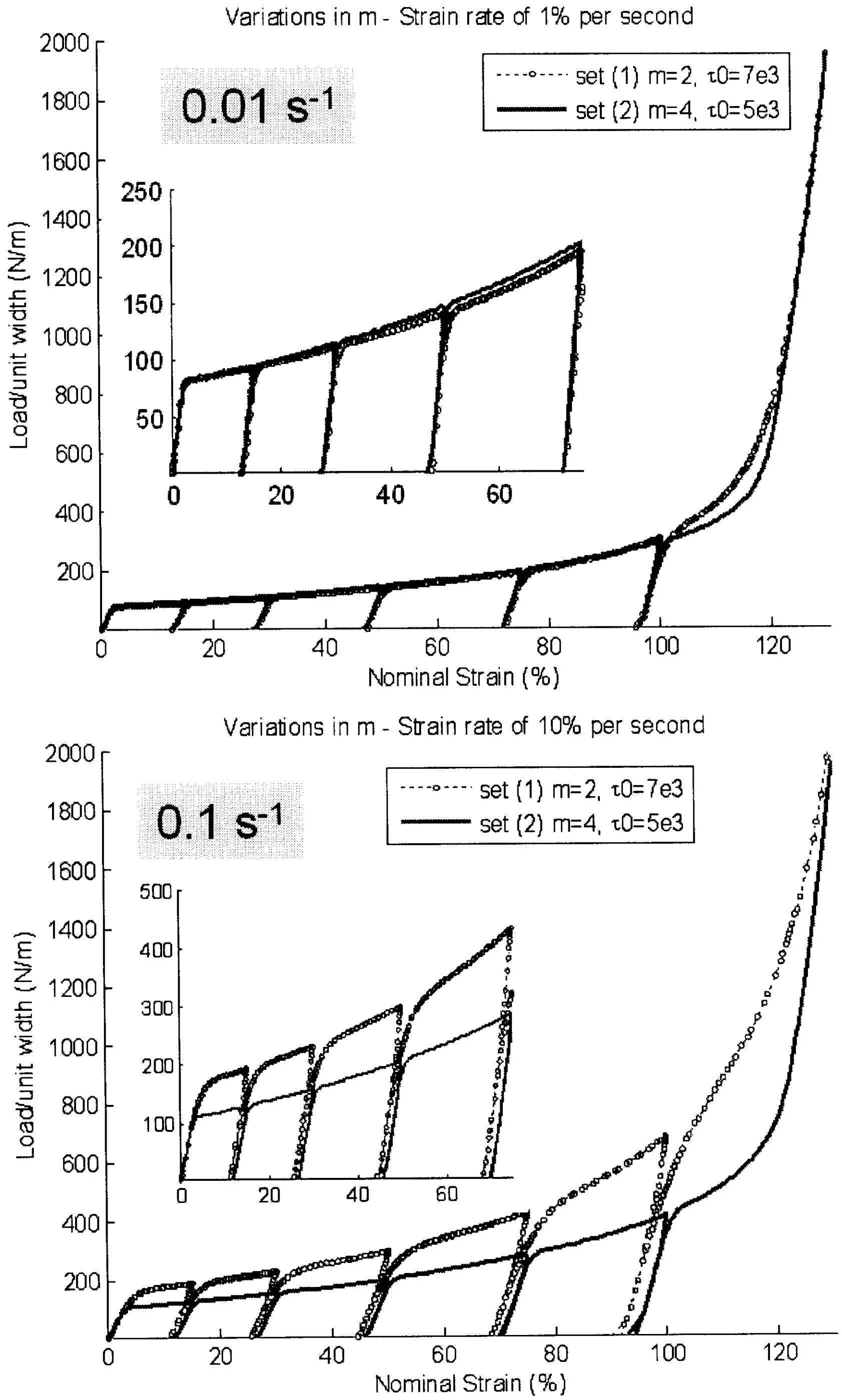

Figure 5-19: Model sensitivity due to variations in m

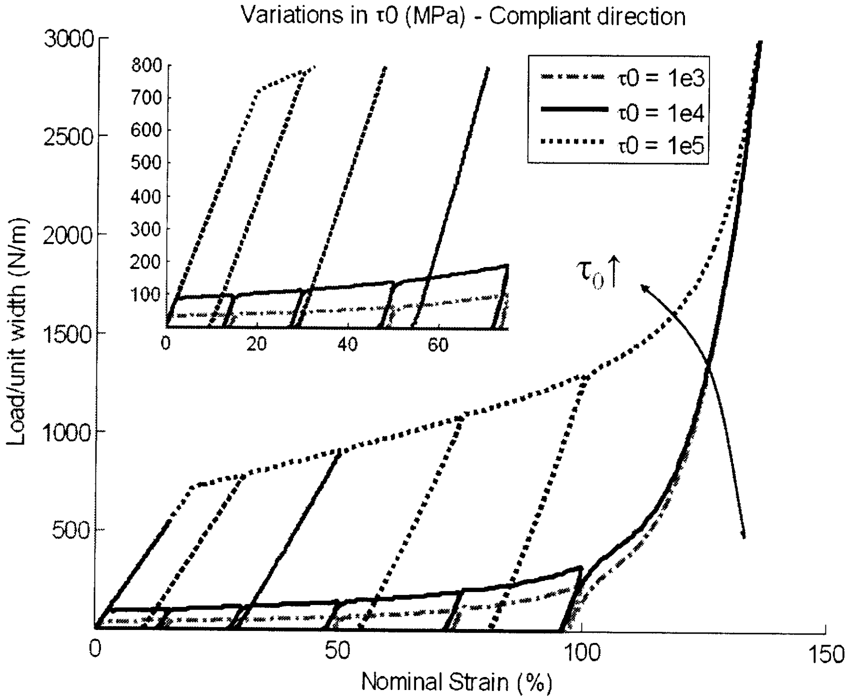

Figure 5-20: Model sensitivity due to variations in τ_0

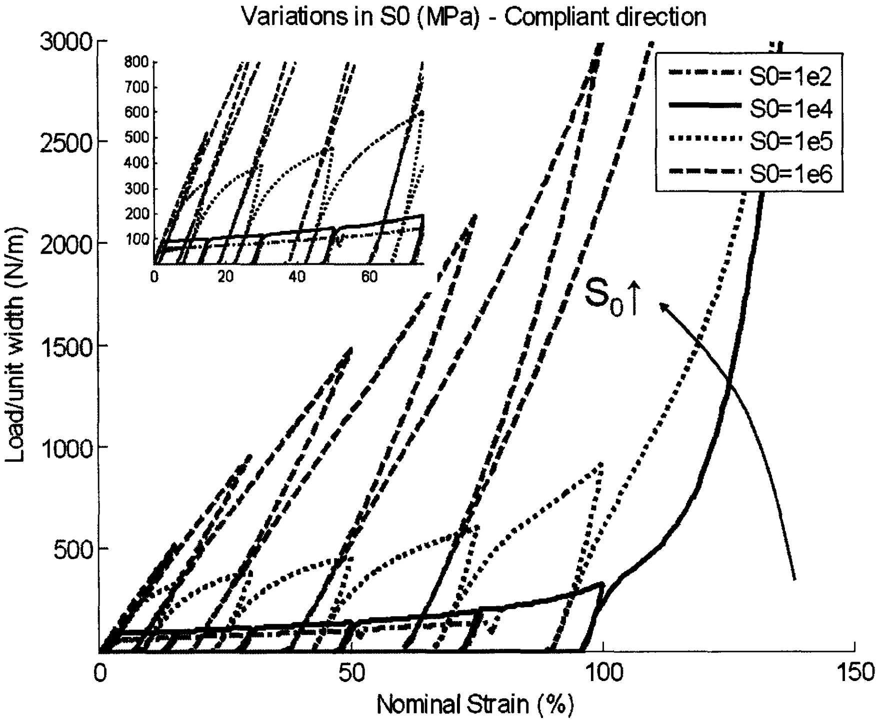

Figure 5-21: Model sensitivity due to variations in S_0

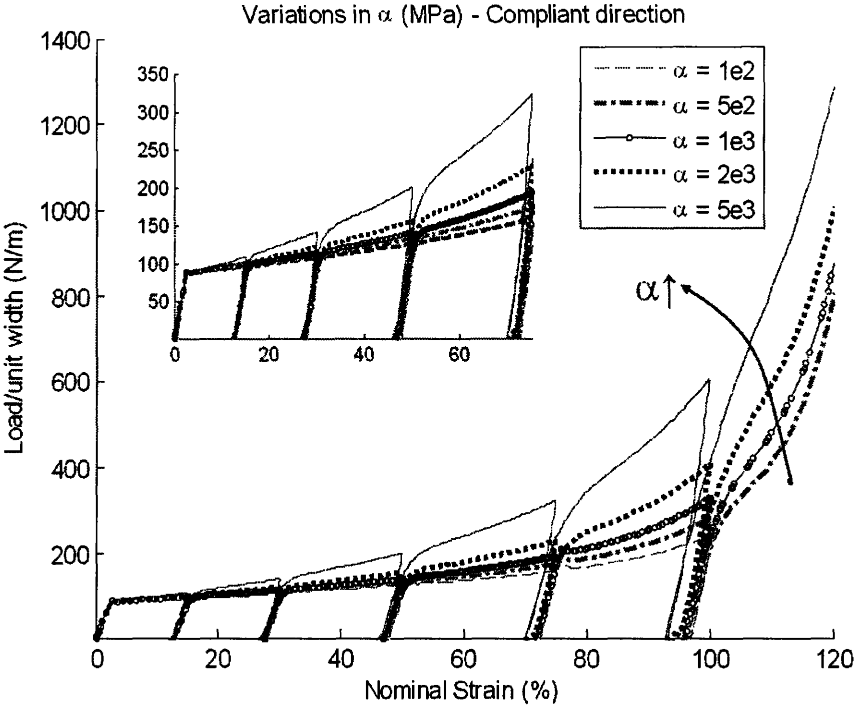

Figure 5-22: Model sensitivity due to variations in α

the load-unload behavior of the model. Therefore, the model sensitivity to v can be captured by considering by the model response under uniaxial monotonic loading along the in-plane principal directions. Figure 5-23 and 5-24 show the axial responses and the corresponding volumetric responses of the model due to the variations in v. As v increases, the structural evolution terminates at a lower level of compaction. As a result, the contribution from the elastic component, which directly controls both axial and bulk responses, increasingly dominates the model response as v approaches unity.

5.3.3 Model sensitivity to the components of the fabric ellipsoid

The model sensitivity to the components of fabric ellipsoid can be described by the variations in (1) principal in-plane eigenvalues (A_0^2 and B_0^2), and (2) principal out-of-plane eigenvalue (C_0^2). All other variations of the components of the fabric ellipsoid can be related to the variations of these two cases. For convenience of illustration, two measures of anisotropy, ξ and ζ are introduced: $\xi = B_0^2/A_0^2$ represents the ratio of the in-plane principal components, and $\zeta = A_0^2/C_0^2$ represents the ratio of the in-plane compliant to the out-of-plane component. The model sensitivity to the in-plane components is performed by increasing the level of in-plane anisotropy [$\xi = 1, 2, 3, 3.75, 5$], while constraining the out-of-plane anisotropy to a constant ($\zeta = 1$). Figure 5-25 shows the effect of various degrees of anisotropy due to the variations of the in-plane components of the fabric ellipsoid. Note that for the special case of in-plane isotropy ($\xi = 1$), the model responses along the $\underset{\sim}{e}_A$- and $\underset{\sim}{e}_B$-directions coincide as expected.

The sensitivity analysis on the principal out-of-plane component is performed by varying the degrees of in-plane to out-of-plane anisotropy, [$\zeta = 1, 16, 32, 160$] while keeping the in-plane anisotropy constant ($\xi = 3.75$). Figure 5-26 shows the model sensitivity to the variations in ζ. As ζ increases, the relative magnitude of the in-plane components to the out-of-plane component increases, resulting in an increase in the in-plane stiffnesses.

The effects of the variations in the principal components of the fabric ellipsoid can be analogously compared to the effects of the variations in the locking stretch. While a variation in the locking stretch λ_L affects the model response in all directions, a variation in one of the principal components of the fabric ellipsoid results in a change in the axial stiffness in that particular direction *relative* to the other directions.

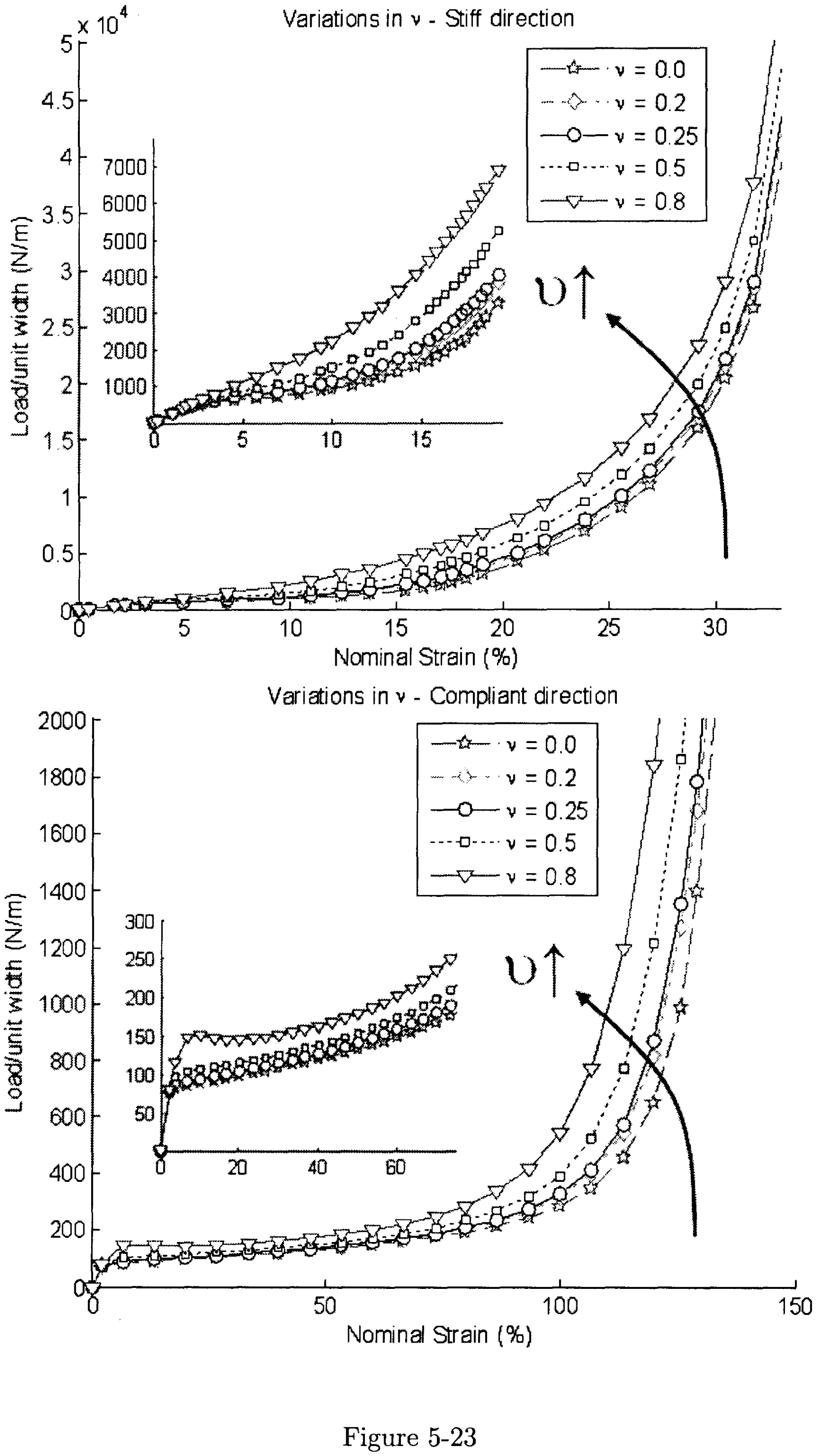
Variations in ν - Stiff direction
x 10^4
Load/unit width (N/m)
Nominal Strain (%)
ν = 0.0
ν = 0.2
ν = 0.25
ν = 0.5
ν = 0.8
υ↑
0, 0.5, 1, 1.5, 2, 2.5, 3, 3.5, 4, 4.5, 5
0, 5, 10, 15, 20, 25, 30
1000, 2000, 3000, 4000, 5000, 6000, 7000
0, 5, 10, 15
Variations in ν - Compliant direction
Load/unit width (N/m)
Nominal Strain (%)
ν = 0.0
ν = 0.2
ν = 0.25
ν = 0.5
ν = 0.8
υ↑
0, 200, 400, 600, 800, 1000, 1200, 1400, 1600, 1800, 2000
0, 50, 100, 150
50, 100, 150, 200, 250, 300
0, 20, 40, 60

Figure 5-23

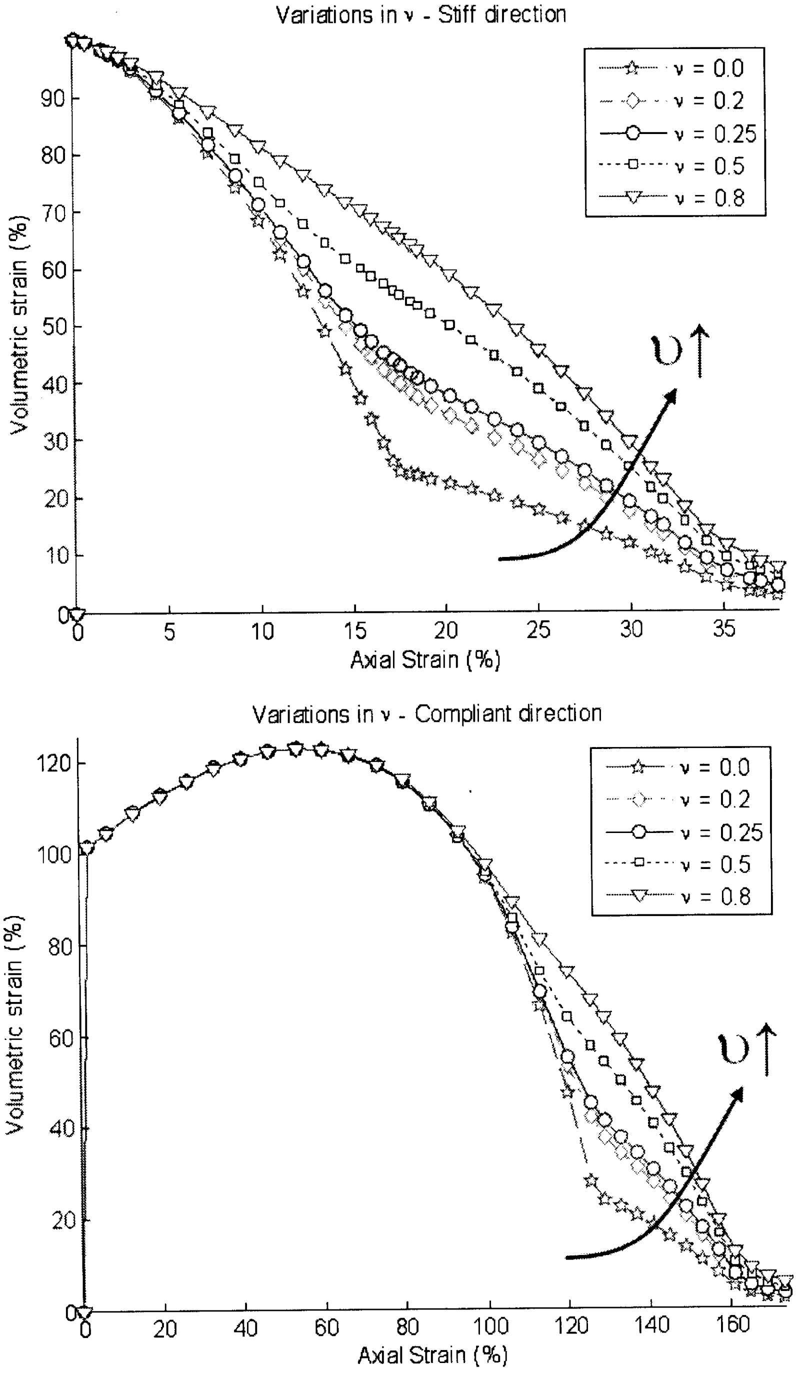
Variations in ν - Stiff direction
Volumetric strain (%)
Axial Strain (%)
0
10
20
30
40
50
60
70
80
90
0
5
10
15
20
25
30
35
ν = 0.0
ν = 0.2
ν = 0.25
ν = 0.5
ν = 0.8
υ↑
Variations in ν - Compliant direction
Volumetric strain (%)
Axial Strain (%)
0
20
40
60
80
100
120
0
20
40
60
80
100
120
140
160
ν = 0.0
ν = 0.2
ν = 0.25
ν = 0.5
ν = 0.8
υ↑

Figure 5-24

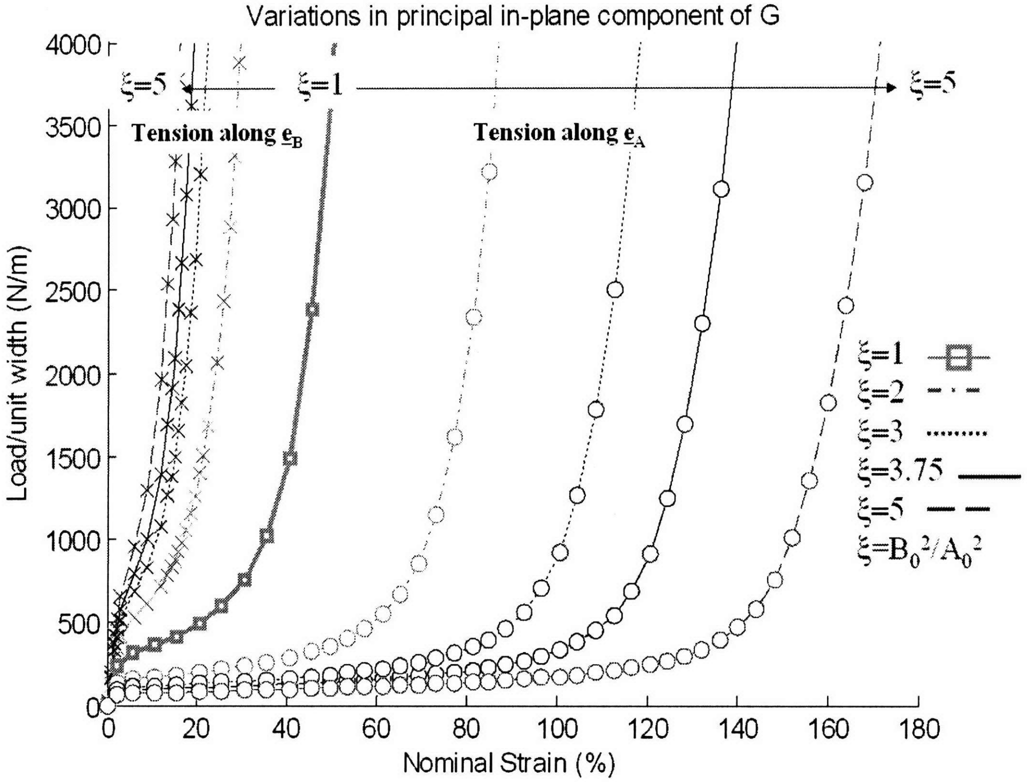

Figure 5-25: Model sensitivity due to variations in principal in-plane components of $\underline{G}$ ($\xi = B_0^2/A_0^2$)

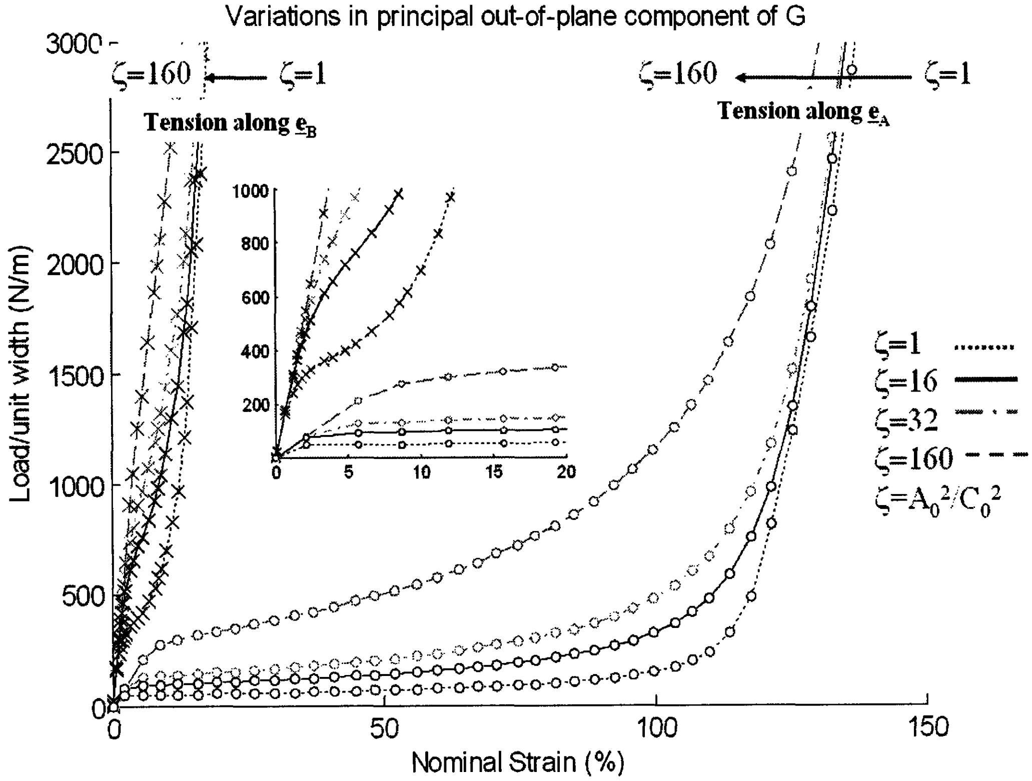

Figure 5-26: Model sensitivity due to variations in principal out-of-plane component of $\underline{G}$

5.4 Chapter Summary

This chapter presents the validation of the proposed fabric model against the response of Dyneema Fraglight. Direct comparisons between the model simulations and the corresponding experimental data show that the model can capture the complex nonlinear anisotropic elastic-inelastic response of this material. Specifically, the model was shown to capture the load-unload behavior due to irrecoverable textural evolution and damage accumulated from inter-fiber friction and inter-fiber compaction. The model was also shown to accurately predict the macroscopic deformed shape and the evolution of the fabric texture under in-plane tensile-dominated modes of deformation.

The model sensitivity to the variations in the model parameters was investigated using the sampling-based sensitivity analysis. The results show that for the model parameters in Table 5.1, the contribution of the inelastic component dominates the model response until the structural evolution terminates after reaching the maximum compaction level. The model response after the termination of inelastic flow is controlled by the elastic component of the model. The analyses also show that the stress-stretch response of the model depends on all parameters, whereas the volumetric response is dominated by λ_L, v and $\underline{G}_0$. The load-unload response of the model is controlled by the following parameters: m, τ_0, S_0, α. The components of the fabric ellipsoid $\underline{G}_0$ control the anisotropic response of the model. In addition to the verification of the effects of each model parameter, the sensitivity analysis confirms that the 13 constitutive parameters are independent, and represent a minimal set of parameters required to describe the fabric deformation mechanisms under consideration.

Chapter 6

Concluding Remarks

6.1 Summary of Accomplishments

This thesis presents a systematic approach to characterize the mechanical response of needlepunched nonwoven fabrics and to formulate a continuum model for this class of materials based on the experimental observation and the material underlying mesostructure. A web of high strength polyethelene fibers manufactured by DSM "Dyneema Fraglight" was selected as the representative material. A number of mechanical characterization techniques have been employed on Dyneema Fraglight in order to analyze the fabric network structure, and to investigate the fabric deformation mechanisms under in-plane tensile-dominated modes of deformation. In characterizing the fabric structure, attention was given to quantifying the morphological sources of fabric anisotropy. The fabric structure was characterized via optical microscopy and its fiber orientation distribution was measured using an image analysis technique.

Uniaxial tensile testing of the fabric revealed that this material exhibits an anisotropic response biased toward the direction of preferential alignment of constituent fibers. The deformation mechanisms governing the fabric response under tensile loads include textural evolution by means of reorientation of constituent fibers, fiber stretch and junction unraveling. The results of the cyclic loading tests indicate that the tensile deformation of the fabric is a combination of elastic deformation from fiber stretch, and inelastic deformation from irrecoverable reorientation of fibers, relative fiber slip as well as fiber disentanglement. Experimental observations in uniaxial cyclic loading tests indicate that the fabric response is dominated by inelastic deformation mechanisms, especially irrecoverable textural evolution and junction unraveling. Results from biaxial tensile tests confirm this observation.

Motivated by the fabric network structure and the underlying deformation mechanisms, a constitutive model for needlepunched nonwoven fabrics was developed with a microstructurally-based continuum framework. The proposed model consists of two constitutive components: a nonlinear element representing the resistance to elastic deformation mechanisms, and a nonlinear viscous element representing the resistance to inelastic deformation mechanisms. For nonwoven fabrics in which the anisotropy of fiber orientation is combined with random entanglement processes, we propose to capture the combined effects of fibers and junctions orientation distributions using a single tensorial representation of the network anisotropy (fabric ellipsoid). An orthotropic elastic model (JS model) for the distributed network is then formulated based on this structural measure and deformation mechanisms of the network structure. The proposed elastic model was shown to capture effects related to the distributed nature of the orientation of fibers and junctions, particularly the contributions due to fiber stretch, and recoverable reorientation of the fibers. It was also favorably compared to the other existing anisotropic models for distributed networks. Though motivated by a mechanistic interpretation of the nonwoven fabrics, the proposed elastic formulation can be used to model different classes of anisotropic network materials, such as biological tissues, and tissue engineering scaffolds.

An inelastic component of the model was proposed to capture mechanisms including irrecoverable textural evolution and other dissipative effects. Experimental characterizations identified the irrecoverable evolution of fabric texture as the dominating inelastic mechanism. Consequently, the inelastic component was prescribed in terms of an evolution law for the network texture (fabric ellipsoid). The proposed evolution law accounts for mechanisms of resistance to inelastic deformation including resistance to inter-fiber sliding and resistance to volume compaction. The driving stress for the evolution of the fabric texture was defined in terms of a macroscopic stress measure biased against the fabric ellipsoid to capture observable effects of the fabric anisotropy on structural evolution. The proposed fabric model requires 13 parameters to completely describe the fabric behavior: six of which define the network anisotropy at the reference state, two parameters capture the elastic response, and the remaining parameters control the evolution of the fabric texture.

The proposed fabric model was validated against the experimental results of tests on Dyneema Fraglight under uniaxial and equibiaxial tensile loadings. Direct comparisons between the model simulations and the corresponding experimental data show that the model can capture the complex nonlinear anisotropic elastic-inelastic response of this material. Specifically, the model was shown to capture the load-unload behavior due to irrecoverable textural evolution and damage accumulated from inter-fiber friction and inter-fiber compaction. The model was also shown to accurately predict the macroscopic deformed shape and the evolution of the fabric texture under in-plane tensile-dominated modes of deformation. Generally good agreement between the model simulation predictions and the experimental results confirm that the proposed constitutive model can be effectively and efficiently used to predict the complex behavior of needlepunched nonwoven fabrics.

6.2 Recommendations for future work

As discussed previously, the proposed formulation does not take into account two important factors in the evolution of textural anisotropy. The first area relates to processes of damage, breakage, and slip of individual fibers from junction points. These effects are limited in materials where the junctions are created by chemical or thermal bonding processes, but are pervasive in nonwovens in which the junctions are created by physical entanglement (e.g., needlepunching). Possible avenues to include these effects in the proposed constitutive framework, include the introduction of an evolution equation for the average unloaded end-to-end length of fibers between junctions. In the current formulation these effects can be captured by an evolution condition for $tr(\underline{G}_t)$, and a modified equation for the evolution of n_t, to ensure conservation of the total fiber length.

The evolution law for the fabric ellipsoid can also be improved. Currently, the evolution of the fabric ellipsoid accounts for the resistance to compaction using the term f_2 in equation 4.41b and the corresponding condition on $\dot{\underline{G}}_t$, which sets the rate of change of $\underline{G}_t$ to zero when the fiber fraction reaches a maximum volumetric compaction level. These terms are isotropic in nature and do not capture the effects of anisotropy on the resistance to compaction. An extended formulation could account for these effects by introducing a tensorial back-stress, coaligned with the $\underline{G}_t$ tensor, reflecting the increased resistance to evolution along directions of high compaction:

$$\underline{T}_{driving} = \underline{T}_{flow} - \underline{T}_{back}\left(\underline{G}_t\right). \tag{6.52}$$

Physically, this backstress represents the effects of the flow resistance due to the compaction of neighboring fibers. Therefore, the constitutive form of the backstress may be derived from the micromechanics-based models for inter-fiber contact (see, for example, Komori et al. [47], Lee [52], and Pan [60], among others).

The effects of the rate of deformation on the response of Dyneema Fraglight have not been addressed in the current work. As a preliminary study of the strain rate effects on the mechanical response of this material, additional uniaxial cyclic loading tests along the R-direction were performed at three nominal strain rates of 0.001 s^{-1}, 0.01 s^{-1} and 0.05 s^{-1}. Figure 6-1 shows comparable responses for the three loading rates, indicating a low degree of rate sensitivity for the considered range of strain rates. To demonstrate the model capability to capture strain rate effects, this limited set of experimental data are fitted by varying the parameter m, which controls the rate sensitivity of the model response, with all other parameters as presented in Table A.1. An acceptable fitting of the model prediction can be obtained by choosing $m = 8$, see Figure 6-1. Note that the experimental response of large strains seems to present a larger degree of rate sensitivity. As fiber disentanglement plays a critical role in increasing fabric compliance at large stretches, it is not surprising that an increase in deformation rate will limit the extent of fiber slippage from junctions, and therefore, result in an increase in asymptotic stiffness. These effects will need to be incorporated in the constitutive formulation for the evolution of the $\underline{G}_t$. More extensive studies over a broader range of deformation rates are needed to properly characterize the strain rate dependence of the fabric response.

In this microstructurally-based continuum model for nonwoven fabrics, some of the model parameters are directly connected to the characteristics of the network structure. For example, the locking stretch λ_L, which represents the extensibility limit of the network, can be physically related to the curliness of the constituent fibers, and the modulus-like parameter μ can be related to the stiffness of the fibers. The parameter representing the maximum compaction limit υ is expected to scale with the initial volume fraction of fibers. Though exact relationships between

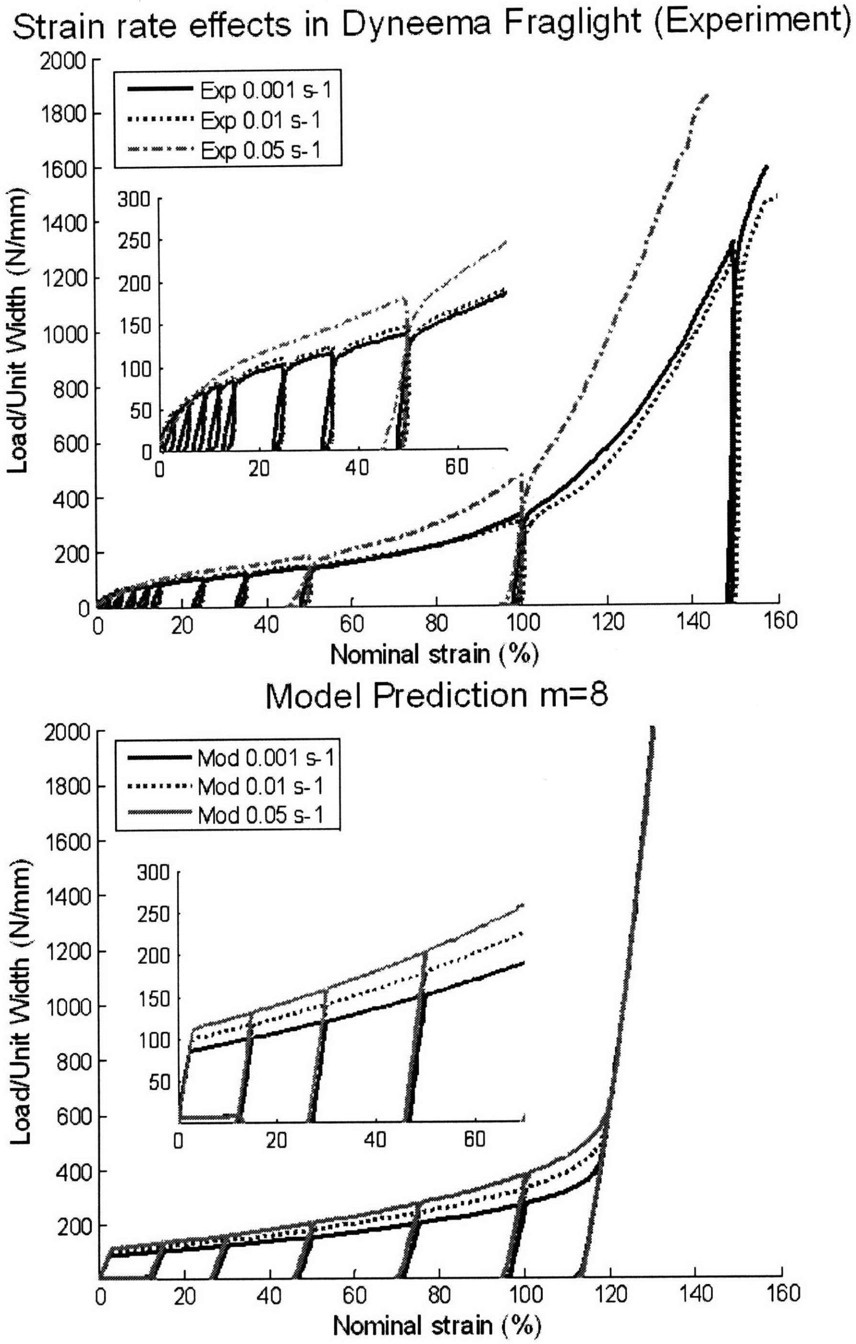

Figure 6-1: Strain rate effect of Dyneema Fraglight: (Top) Experiments and (Bottom) Model fit ($m = 8$)

these physically motivated parameters and the actual characteristics of the network have not been established in the current work, they can be verified by performing additional analysis on the fabric texture.

The relationship between the fitted fabric ellipsoid and the experimentally measurable morphological properties of the fabric should be further verified. Currently the in-plane components of the fabric ellipsoid are estimated from the two dimensional images of fabric structure, while the out-of-plane component serves as a fitting parameter. The robustness of the microstructural representation via fabric ellipsoid cannot be tested until related technique enabling the measurement of fabric structural properties in three dimensions are developed.

The proposed fabric model assumes that nonwoven fabrics can be represented, via homogenization, by a continuum with uniform properties. However, the characterization of the Dyneema Fraglight structure reveals an inhomogeneous texture due to non-uniform spatial distributions of fibers with increased fiber density around entanglement points. Consequently, the fabric exhibits an inhomogeneous response at areas of higher fiber density. Following standard approaches in the characterization of fabric texture, the fabric inhomogeneity can be analyzed using image analysis techniques. e.g., [66], [67], and quantified in terms of gray-scale intensity distribution. The inhomogeneity data can be incorporated into the current model by relating spatial statistical variations in model parameters (e.g., the modulus μ) to the measured intensity distribution.

This project was the preliminary step to develop a model capable of capturing the nonwoven fabric response under ballistic impact. The current model has been implemented only for quasi-static in-plane implicit analysis. To capture the fabric ballistic response, the model must be implemented in a 3D membrane (or shell) formulation in conjunction with an explicit code for dynamic analysis.

Further development in the areas described above will result in a model capable of predicting the mechanical response of nonwoven fabrics both at macro and mesostructural levels in a wide range of applications.

Appendix A

Relationship between Orientation Distribution of Junction-to-junction Distance (JJD) and Fiber Orientation Distribution (FOD)

For a fiber network with junction points defined by random bonding pattern (e.g., self-entanglement of constituent fibers), the junction-to-junction distance distribution (JJD) of the network can be related to its fiber orientation distribution (FOD) because the locations of inter-fiber junctions are statistically biased by the number of fiber intersections, which is related to the fiber orientation distribution. This appendix demonstrates a preliminary attempt to relate the two orientation distributions in a simplified network of straight, cylindrical, inter-penetrable fibers using (1) numerical simulation (termed "simplified straight fiber model") and (2) structural analysis.

A.1 Simplified straight fiber model

To evaluate the relationship between the JJD and the FOD of a network with a random bonding pattern, we performed a numerical simulation of a simplified network of infinitely long, straight,

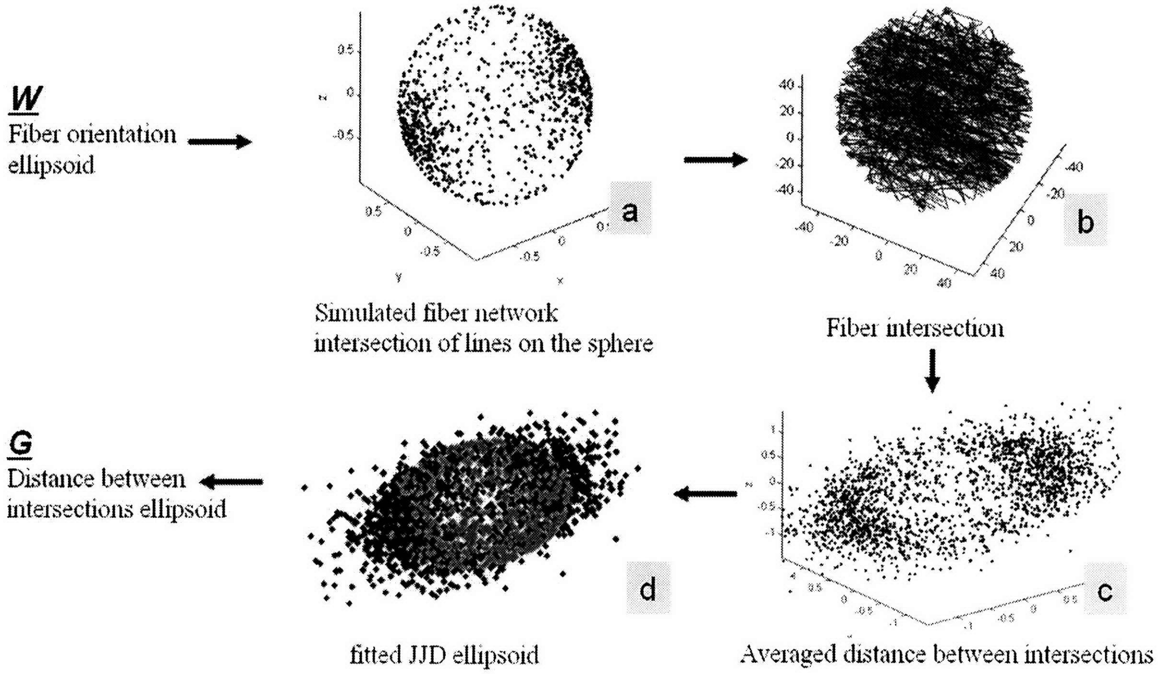

Figure A-1: Schematic of the simulation: an approach to calculate a JJD ellipsoid from a given FOD ellipsoid in a simplified network of straight fibers

cylindrical, inter-penetrable fibers randomly located in a three dimensional spherical window. The relationship between the fiber orientation distribution (FOD) and the junction-to-junction distance distribution of this network is determined by assigning the orientations of the simulated fibers according to the prescribed FOD, and calculating the corresponding JJD of the network. The calculation procedure in Figure A-1 can be described as follows.

Given a network of n fibers that are oriented according to the prescribed FOD ellipsoid (figure A-1(a)), the intersections of the network can be determined using the following tracking algorithm. First, the shortest distances between every pairs of fibers in this network are calculated. If the distance between two fibers is less than a threshold value d, a intersection is created on each fiber at the location of the shortest inter-fiber distance. With the locations of all intersections specified (figure A-1(b)), the intersection-to-intersection distance in a given direction can be determined by averaging the distances between every neighboring intersections on each fiber. The averaged intersection-to-intersection distance is then plotted as a function of the fiber orientation in Figure A-1(c). The fabric ellipsoid describing the orientation distribution of junction-to-junction distances is assumed to scale with the intersection distribution and is subsequently constructed by fitting a three-dimensional ellipsoid over this plot using a simplex algorithm (figure A-1(d)).

Note that the repeatability of the results obtained with this method increases with the number of fibers being simulated (i.e., the size of the computational volume). However, the computational cost also increases exponentially for increasing fiber numbers. This calculation typically fails under two circumstances: (1) when the input FOD ellipsoid is highly anisotropic, in which case, numerical singularity arises when locating the junctions in the non-preferential direction, and (2) when the simplex algorithm does not converge.

The measured FOD and JJD pairs presented in Table A.1 are obtained from simulations of n number of fibers with d diameter in a spherical window of radius $50L$, where L being an arbitrary length scale.

The simulation results indicate that for a network with random bonding pattern (1) the principal directions of the JJD ellipsoid co-align with the principal directions of the FOD ellipsoid, and (2) the JJD ellipsoid may be approximated from the FOD ellipsoid.

A.2 Structural analysis

To verify the simulation result, we performed a structural analysis of the simplified straight fiber network. The analytical relation of JJD and FOD provided here is a modification of the analysis of inter-fiber contact by Komori et al. [48]-[47] and Toll [71]. Suppose that the network under consideration consists of n fibers *per unit volume* arranged according to a given fiber orientation distribution $w\left(\underline{p}\right)$ (See Eq 3.4 for the relationship between the orientation distribution function $w\left(\underline{p}\right)$ and the corresponding fabric ellipsoid $\underline{\underline{W}}$). The fibers in this network are allowed to inter-penetrate, and the intersections are defined by these inter-penetration points. Consider a test fiber with average length L and diameter d aligned in the unit direction $\underline{p}$, see Figure A-2.

		Input FOD			Output normalized JJD $\underline{G}$					
		Component of $\underline{W}$			simulation prediction			analytical solution		
n	d	(AA)	(BB)	(CC)	(AA)	(BB)	(CC)	(AA)	(BB)	(CC)
4000	$2L$	1.000	1.000	1.000	1.000	1.000	1.000	1.000	1.000	1.000
4000	$2L$	1.800	0.600	0.600	1.353	0.819	0.827	1.243	0.878	0.879
4000	$2L$	2.143	0.429	0.429	1.420	0.790	0.790	1.405	0.798	0.797
4000	$2L$	2.500	0.250	0.250	1.840	0.547	0.613	1.701	0.649	0.650
4000	L	1.000	1.000	1.000	1.000	1.000	1.000	1.000	1.000	1.000
4000	L	1.800	0.600	0.600	1.346	0.830	0.824	1.243	0.878	0.879
4000	L	2.143	0.429	0.429	1.303	0.859	0.837	1.405	0.798	0.797
4000	L	2.500	0.250	0.250	2.020	0.570	0.410	1.701	0.649	0.650
2000	$2L$	1.000	1.000	1.000	0.999	1.001	1.000	1.000	1.000	1.000
2000	$2L$	1.800	0.600	0.600	1.371	0.810	0.818	1.224	0.885	0.891
2000	$2L$	2.143	0.429	0.429	1.359	0.834	0.806	1.394	0.803	0.803
2000	$2L$	2.500	0.250	0.250	2.050	0.468	0.481	1.685	0.657	0.658
3000	$2L$	1.000	1.000	1.000	1.000	1.000	1.000	1.000	1.000	1.000
3000	$2L$	1.800	0.600	0.600	1.372	0.814	0.814	1.247	0.879	0.874
3000	$2L$	2.143	0.429	0.429	1.420	0.790	0.790	1.424	0.787	0.788
3000	$2L$	2.500	0.250	0.250	1.840	0.580	0.580	1.713	0.644	0.644
3000	$2L$	1.200	1.200	0.600	1.063	1.063	0.874	1.049	1.040	0.910
3000	$2L$	0.857	1.714	0.429	0.932	1.384	0.684	0.939	1.218	0.843
3000	$2L$	0.750	2.000	0.250	0.936	1.412	0.652	0.873	1.360	0.767
3000	$2L$	1.250	1.500	0.250	1.199	1.221	0.580	1.058	1.139	0.803
3000	$2L$	0.750	1.000	1.250	0.912	1.020	1.068	0.932	1.006	1.062

Table A.1: Examples of the calculated JJD ellipsoid for a given FOD ellipsoid from numerical simulation and analytical solution

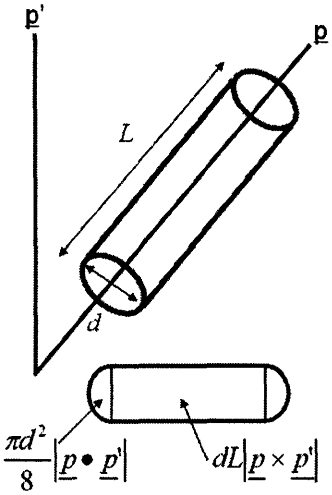

Figure A-2: Schematic of fiber-intersection

The number of points N on the test fiber that are in contact with fibers in an arbitrary direction $\underline{p}'$ is given by (Toll [71])

$$N\left(\underline{p},\underline{p}'\right) = n\left[A\left(\underline{p},\underline{p}'\right)L + V\right], \tag{A.1}$$

where $V = \frac{\pi d^2}{4}$ is the volume of the fiber, and $A\left(\underline{p},\underline{p}'\right) = dL\left|\underline{p}\times\underline{p}'\right| + \frac{\pi d^2}{8}\left|\underline{p}.\underline{p}'\right|$ is the projected area of the test fiber into the direction $\underline{p}'$. For non-aligned slender fibers (i.e., $\frac{L}{d} >> 1$), Equation A.1 reduces to

$$N\left(\underline{p},\underline{p}'\right) = ndL^2\left|\underline{p}\times\underline{p}'\right|. \tag{A.2}$$

Now consider the average number of contact points on the test fiber made by the fibers in all other directions;

$$\overline{N}\left(\underline{p}\right) = \oint N\left(\underline{p},\underline{p}'\right) w\left(\underline{p}'\right) d\underline{p}' = ndL^2 f\left(\underline{p}\right), \tag{A.3}$$

where $f\left(\underline{p}\right) = \oint \left|\underline{p}\times\underline{p}'\right| w\left(\underline{p}'\right) d\underline{p}'$. The average spacing between the contact points (inter-junction distance) along the test direction is given by

$$l\left(\underline{p}\right) = \frac{L}{\overline{N}\left(\underline{p}\right)} = \frac{\pi d}{4\phi f\left(\underline{p}\right)}, \tag{A.4}$$

and $\phi = n\frac{\pi d^2}{4}L$ is the volume fraction of the fibers. The inter-junction distance in each material direction is a product of the junction-to-junction distance orientation distribution $\left(g\left(\underline{p}\right)\right)$ and the average inter-junction distance $\bar{l}$;

$$l\left(\underline{p}\right) = g\left(\underline{p}\right)\bar{l}. \tag{A.5}$$

By substituting A.5 into A.4 and using $g\left(\underline{p}\right) = \underline{G} : \left(\underline{p} \otimes \underline{p}\right)$, Equation A.4 may be cast in term of the JJD ellipsoid

$$\underline{G} : \left(\underline{p} \otimes \underline{p}\right) = \frac{\pi d}{4\phi\bar{l}}\left(\oint \left|\underline{p}' \times \underline{p}\right| \left(\underline{W} : \left(\underline{p}' \otimes \underline{p}'\right)\right) d\underline{p}'\right)^{-1}. \tag{A.6}$$

The analytical expression in Equation A.6 illustrates a complex relationship between JJD and FOD ellipsoids in the network with infinitely-long, straight, cylindrical fibers. The analytical solution is compared to the simulation predictions in Table A.1. Good agreements between the two approaches confirm that in this simplified network of straight fibers with random bonding pattern the JJD ellipsoid and the FOD ellipsoid are related. Therefore, the JJD ellipsoid can be determined from a given (experimentally measurable) FOD ellipsoid.

Appendix B

Application of the Effective Stretch

The concept of effective stretch introduced in Chapter 3 is an effective yet simple-to-implement approach to model the complex effects due to stretching of fibers in anisotropic distributed elastic networks. This concept relates the contribution of the stretch of single fibers in the network to the macroscopic stretch of the network using a tensorial measure of deformation ($\underline{F}$) and a structural measure (fabric ellipsoid $\underline{G}_0$) representing the network anisotropy. In Chapter 3, we demonstrated the applicability of this concept by formulating a continuum model for a network with the force-stretch response of the constituent fibers following Langevin statistics. The JS-model was subsequently formulated by combining the effects of stretch of individual fibers and inter-fiber repulsion, and was shown to be favorably compared to the other orthotropic network models with the same form of force-stretch relation. Though the concept of the effective stretch was initially developed for a network of fibers with extensibility limit, we demonstrate in this appendix that this concept can be extended (with care) to model the response of an orthotropic fiber network with no extensibility limit as well.

B.1 Formulation of an orthotropic elastic model based on the effective stretch and the exponential force-stretch relation of individual fibers

Consider a distributed fiber network in which the mechanical response of the constituent fibers can be described by an exponential force-stretch response similar to the form given by Holzapfel [40] as follows:

$$f\left(\lambda_f\right) = 2k_1\left(\lambda_f - 1\right)\left(\exp\left(k_2\left(\lambda_f - 1\right)^2\right)\right). \tag{B.1}$$

where λ_f represents the end-to-end fiber stretch, $f\left(\lambda_f\right)$ is the resultant force, k_1 and k_2 are the constitutive parameters. Integrating the force-stretch expression in B.1 with respect to an incremental displacement $r_0 d\lambda_f$, where r_0 is the end-to-end (unstretched) fiber length, yields the strain energy associated with the stretching of a single fiber segment:

$$\psi_{fiber}^{\text{expo}}\left(\lambda_f\right) = \int_1^{\lambda_f} f\left(\lambda_f'\right) r_0 d\lambda_f' = \frac{r_0 k_1}{k_2}\left(\exp\left(k_2\left(\lambda_f - 1\right)^2\right)\right). \tag{B.2}$$

Note that the exponential force-stretch relation in B.1 does not account for the extensibility limit of the fibers, whereas the force-stretch relation in terms of Langevin statistic accounts for the extensibility limit in terms of a locking stretch, λ_L.

Following the concepts of the effective stretch, the strain energy density of the network $\overline{\Psi}_{network}$ associated with the stretching of n_0 exponential fiber segments per unit (reference) volume in a network with anisotropy captured by the fabric ellipsoid $\underline{G}_0$ is given by:

$$\overline{\Psi}_{network}^{\text{expo}} = \frac{n_0 r_0 k_1}{k_2}\left(\exp\left(k_2\left(\lambda_{eff} - 1\right)^2\right)\right). \tag{B.3}$$

Differentiating B.3 with respect to the right Cauchy Green tensor yields an expression for the macroscopic second Piola-Kirchhoff stress of the network:

$$\underline{T}_{network}^{\text{expo}} = \frac{\mu}{3}\frac{\left(\lambda_{eff} - 1\right)}{\lambda_{eff}}\left(\exp\left(k_2\left(\lambda_{eff} - 1\right)^2\right)\right)\underline{G}_0, \tag{B.4}$$

with corresponding Cauchy stress

$$\underline{\sigma}^{\text{expo}}_{network} = \frac{\mu}{3J}\frac{(\lambda_{eff}-1)}{\lambda_{eff}}\left(\exp\left(k_2\left(\lambda_{eff}-1\right)^2\right)\right)\underline{F}\underline{G}_0\underline{F}^T, \tag{B.5}$$

where $\mu = n_0 r_0 k_1$ represents a modulus-like parameter for this form of constitutive relation.

B.4 and B.5 account for contributions due to the stretch of individual fibers, and yield a stress-free configuration for $\lambda_{eff} = 1$. In contrast to the formulation of the JS-model, the forms of macroscopic stresses derived from the effective stretch and the exponential force-stretch relation need not be augmented by an additional constitutive term to enforce equilibrium conditions in the reference configuration. However, because the formulation in B.3 does not account for the effects of inter-fiber interaction, e.g., inter-fiber repulsion or bulk compressibility, it has no resistance to the deformation at constant effective stretch $\lambda_{eff} = 1$[1].

To account for the contribution of network resistance to the volume compaction, a strain energy representing the isotropic bulk compressibility is added to B.3 (similar to [12]);

$$\overline{\Psi}_{vol}\left(J\right) = \kappa\left(J\ln\left(J\right) - J\right), \tag{B.6}$$

The strain energy of the network with the contributions of fiber stretch and bulk compressibility becomes

$$\widetilde{\Psi} = \overline{\Psi}_{network} + \overline{\Psi}_{vol}, \tag{B.7}$$

with the second Piola-Kirchhoff stress,

$$\underline{\widetilde{T}} = \frac{\mu}{3}\frac{(\lambda_{eff}-1)}{\lambda_{eff}}\left(\exp\left(k_2\left(\lambda_{eff}-1\right)^2\right)\right)\underline{G}_0, + J\kappa\ln\left(J\right)\underline{C}^{-1}, \tag{B.8}$$

and the corresponding Cauchy stress

$$\underline{\widetilde{\sigma}} = \frac{\mu}{3J}\frac{(\lambda_{eff}-1)}{\lambda_{eff}}\left(\exp\left(k_2\left(\lambda_{eff}-1\right)^2\right)\right)\underline{F}\underline{G}_0\underline{F}^T + \kappa\ln\left(J\right)\underline{I}. \tag{B.9}$$

---

[1] There exists a combination of a non-trivial deformation gradient ($\underline{F} \neq \underline{1}$) and the fabric tensor that yields a stress free state with $\lambda_{eff} = 1$, e.g., $\underline{G}_0 = A_0^2\underline{e}_A \otimes \underline{e}_A + B_0^2\underline{e}_B \otimes \underline{e}_B + C_0^2\underline{e}_C \otimes \underline{e}_C$, and $\underline{F} = \frac{\sqrt{3-B_0^2-C_0^2}}{A_0^2}\underline{e}_A \otimes \underline{e}_A + 1\underline{e}_B \otimes \underline{e}_B + 1\underline{e}_C \otimes \underline{e}_C$.

B.9 resembles the compressible form of the *transversely isotropic* hyperelastic model by Gasser et al. [32][2]. As proven in [32], this form of stress is stable when modeling a distributed fiber network with isotropic or transversely isotropic symmetry. When extended to a network with orthotropic symmetry, however, the expression B.9 is unstable. The proof of instability is given as follows.

Consider a special case of deformations in which the fiber network is stretched (with macroscopic stretches $\lambda_A, \lambda_B, \lambda_C$) along the principal directions of material anisotropy $\underset{\sim}{e}_A, \underset{\sim}{e}_B, \underset{\sim}{e}_C$, the deformation gradient can be expressed as:

$$\underline{F} = \lambda_A\ \underset{\sim}{e}_A \otimes \underset{\sim}{e}_A + \lambda_B\ \underset{\sim}{e}_B \otimes \underset{\sim}{e}_B + \lambda_C\ \underset{\sim}{e}_C \otimes \underset{\sim}{e}_C. \tag{B.10}$$

In this state of deformation, the effective stretch is given by

$$\lambda_{eff}^2 = \frac{tr\left(\underline{F G_0 F^T}\right)}{3} = \frac{1}{3}\left(A_0^2\lambda_A^2 + B_0^2\lambda_B^2 + C_0^2\lambda_C^2\right), \tag{B.11}$$

and the volumetric strain is given by

$$\lambda_A\lambda_B\lambda_C = J. \tag{B.12}$$

Now, consider a non-trivial stretch along the $\underset{\sim}{e}_C$-direction ($\lambda_C \neq 1$) while constraining the material to the stress-free state ($\lambda_{eff} = 1, and J = 1$). Under this special case, B.11 and B.12 become

$$\begin{aligned} A_0^2\lambda_A^2 + B_0^2\lambda_B^2 + C_0^2\lambda_C^2 &= \left(A_0^2 + B_0^2 + C_0^2\right), && \text{(B.13a)} \\ \lambda_A\lambda_B\lambda_C &= 1. && \text{(B.13b)} \end{aligned}$$

The non-trivial stretches in the lateral directions λ_A and λ_B obtained from the conditions B.13a and B.13b are given by

---

[2] with some parameter adjustments and without the effects of the ground substance.

$$\lambda_A^2 = \frac{\left(tr\left(\underline{G}_0\right) - C_0^2\lambda_C^2\right) \pm \sqrt{\left(tr\left(\underline{G}_0\right) - C_0^2\lambda_C^2\right) - \frac{4A_0^2B_0^2}{\lambda_C^2}}}{2A_0^2}; \lambda_B^2 = \frac{1}{\lambda_A^2\lambda_C^2}. \tag{B.14}$$

The existence of non-trivial stretches ($\lambda_A \neq 1$,$\lambda_B \neq 1$,$\lambda_C \neq 1$) in a stress-free state proves the instability of B.9.

It can be inferred from the development of B.9 that a model which accounts for the contribution of fiber stretch (via the effective stretch) and the bulk compressibility does not have sufficient constraints to describe distributed networks with an orthotropic symmetry. To attain sufficient stability, the formulation in B.9 can be augmented by an additional constitutive contribution representing the effects of inter-fiber repulsion. The strain energy representing the inter-fiber repulsion is phenomenologically prescribed by:

$$\overline{\Psi}_{repulsion} = \frac{\mu}{2}\left(E^*\right)^2, \tag{B.15}$$

with

$$E^* = \frac{tr\left(\underline{C}^{-1}\underline{G}_0\right)}{tr\left(\underline{G}_0\right)} - 1, \tag{B.16}$$

and corresponding Cauchy stress

$$\underline{\sigma}_{repulsion} = -\frac{\mu E^*}{J tr\left(\underline{G}_0\right)}\underline{F}^{-T}\underline{G}_0\underline{F}^{-1}. \tag{B.17}$$

The strain energy of the inter-fiber repulsion in B.15, though seemingly arbitrarily prescribed, is chosen because the measure, E^*, combined with the effective stretch measure $\lambda_{eff} = \sqrt{\frac{tr\left(\underline{F}\underline{G}_0\underline{F}^T\right)}{3}} = \sqrt{\frac{tr\left(\underline{G}_0\underline{C}\right)}{3}}$ and the volumetric strain $J = \sqrt{\det\left(\underline{C}\right)}$ represent a set of linearly independent group of invariants of $\underline{C}$ and $\underline{G}_0$. It can be shown that alternative energy contributions can be proposed in place of B.15, provided that they are expressed in terms of invariants of $\underline{C}$ and $\underline{G}_0$ and are linearly independent from $tr\left(\underline{C}\underline{G}_0\right)$ and $\det\left(\underline{C}\right)$. For other possible invariants of $\underline{C}$ and $\underline{G}_0$, refer to the work by Spencer [69], Zheng [80], and Zysset [81].

By including the contribution from the inter-fiber repulsion, the orthotropic elastic model for distributed network with an exponential force-stretch relation of the constituent fibers can be written in the following form:

$$
\begin{aligned}
\overline{\Psi} &= \overline{\Psi}_{network} + \overline{\Psi}_{repulsion} + \overline{\Psi}_{vol} \qquad \text{(B.18a)} \\
&= \frac{\mu}{2}\left(\exp\left(k_2\left(\lambda_{eff}-1\right)^2\right)\right) + \frac{\mu}{2}\left(E^*\right)^2 + \kappa\left(J\ln\left(J\right) - J\right). \qquad \text{(B.18b)}
\end{aligned}
$$

with corresponding stress

$$
\underline{\sigma} = \frac{\mu}{Jtr\left(\underline{G}_0\right)}\left(\frac{\left(\lambda_{eff}-1\right)}{\lambda_{eff}}\left(\exp\left(k_2\left(\lambda_{eff}-1\right)^2\right)\right)\underline{F}\underline{G}_0\underline{F}^T - E^*\underline{F}^{-T}\underline{G}_0\underline{F}^{-1}\right) + \kappa\ln\left(J\right)\underline{I}. \tag{B.19}
$$

With the additional constraint for the stress-free configuration provided by B.16 ($E^* = 1$), B.19 is always stable. Figure B-1 show the uniaxial responses of the exponential model along the three principal directions of the fabric ellipsoid using $\mu = 1e6$Pa, $k_2 = 2$, $\kappa = 1e6$Pa, $A_0 = 1.33$, $B_0 = 1.00$,and $C_0 = 0.67$.

B.2 Concluding Remarks

We introduced an alternative formulation for the response of an orthotropic elastic networking using the effective stretchin an exponential force-stretch relation. In this formulation, we showed that a model that only accounts for the contributions of fiber stretch (via the effective stretch) and bulk compressibility does not have sufficient constraints to describe a distributed network with orthotropic symmetry. An additional energy contribution representing the effects of inter-fiber repulsion was prescribed as a function of $tr\left(\underline{C}^{-1}\underline{G}_0\right)$ to ensure the stability of the model. With the contribution from the fiber stretch, the inter-fiber repulsion, and the bulk compressibility, the proposed model is complete, and can be used to predict the response of orthotropic fiber networks.

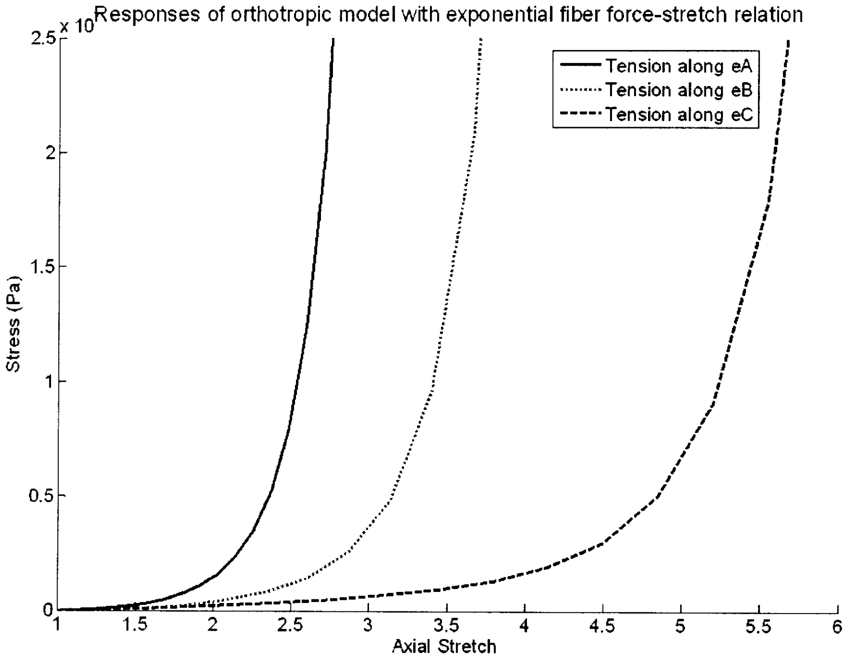

Figure B-1: Uniaxial responses of the orthotropic model for networks with an exponential force-stretch relation

Bibliography

[1] Anand, L., “A Constitutive Model for Compressible Elastomeric Solids”, *Computational Mechanics*, 18: 339-355 (1996).

[2] Arruda, E.M., and Boyce, M.C., "A Three-Dimensional Constitutive Model for the Large Stretch Behavior of Rubber Elastic Materials", *Journal of the Mechanics and Physics of Solids*, **41**(2):389-412 (1993).

[3] Aravas, N,. "Finite-strain Anisotropic Plasticity and the Plastic Spin", *Modelling and Simulation in Materials Science and Engineering*, 2: 483-504 (1994).

[4] Backer, S., and Petterson, D.R., “Some Principles of Nonwoven Fabrics”, *Textile Research Journal*, 30: 704-711 (1960).

[5] Ball, J., "Convexity Conditions and Existence Theorems in Nonlinear Elasticity", *Archive for Rational Mechanics and Analysis*, 63:: 337-403 (1977).

[6] Beatty, M.F., “Constitutive Equations for the Back Stress in Amorphous Glassy Polymers”, *Mathematics and Mechanics of Solids*, 10: 167-181 (2005).

[7] Bergstrom, J.S., and Boyce, M.C., “Constitutive Modeling of the Large Strain Time-dependent Behavior of Elastomers”, *Journal of the Mechanics and Physics of Solids*, 46(5): 931-954 (1998).

[8] Bias-Singh, S., Anandjiwala, R.D., and Goswami, B.C., “Characterizing Lateral Contraction Behavior of Spunbonded Nonwovens during Uniaxial Tensile Deformation”, *Textile Research Journal*, 66(3): 131-140 (1996).

[9] Billiar, K.L., and Sacks, M.S., "Biaxial Mechanical Properties of the Natural and Glutaraldehyde Treated Aortic Valve Cusp – Part I: Experimental Results", *Journal of Biomechanical Engineering – Transactions of the ASME*, 122(1): 23-30 (2000).

[10] Bischoff, J.E., Arruda, E.M., and Grosh, K., "Finite Element Modeling for Human Skin using an Isotropic, Nonlinear Elastic Constitutive Model", *Journal of Biomechanics*, 33: 645-652 (2000).

[11] Bischoff, J. E.,Arruda, E. M., and K. Grosh, "A new constitutive model for the compressibility of elastomers at finite deformations", *Rubber Chemistry and Technology*, 74(4) : 541-559 (2001).

[12] Bischoff, J.E., Arruda, E.M., and Grosh, K., "A Microstructurally-Based Orthotropic Hyperelastic Constitutive Law", *Journal of Applied Mechanics*, 69: 570-579 (2002).

[13] Bischoff, J.E., Arruda, E.M., and Grosh, K., "Finite Element Simulations of Orthotropic Hyperelasticity", *Finite Elements in Analysis and Design*, 38: 983-998 (2002).

[14] Bischoff, J.E., Arruda, E.M., and Grosh, K., "Orthotropic Hyperelasticity in Terms of an Arbitrary Molecular Chain Model", *Journal of Applied Mechanics-transactions of the ASME*, 69(2): 198-201 (2002).

[15] Britton, P.N., Sampson, A.J., Elliott, C.F., Graben, H.W., and Gettys, W.E., "Computer Simulation of the Mechanical Properties of Nonwoven Fabrics, Part I: The Method", *Textile Research Journal*, 53: 363-368 (1983).

[16] Britton, P.N., Sampson, A.J., and Gettys, W.E., "Computer Simulation of the Mechanical Properties of Nonwoven Fabrics, Part II: Bond Breaking", *Textile Research Journal*, 54: 1-5 (1984).

[17] Britton, P.N., Sampson, A.J., and Gettys, W.E., "Computer Simulation of the Mechanical Properties of Nonwoven Fabrics, Part III: Fabric Failure", *Textile Research Journal*, 54: 425-428 (1984).

[18] Boyce, M.C., Weber, G.G., and Parks, D.M., "On the Kinematics of Finite Strain Plasticity", Journal of the Mechanics and Physics of Solids, 37(5): 647-665 (1989).

[19] Boyce, M.C, and Arruda, E.M., “Constitutive Models of Rubber Elasticity: A Review”, *Rubber Chemistry and Technology*, 73(3): 504-523 (2000).

[20] Carnaby, G.A., Pan, N., “Theory of the Compression Hysteresis of Fibrous Assemblies”, *Textile Research Journal*, 59: 275-284 (1989).

[21] Chagnon, G., Verron, E., Marckmann, G., and Gornet, L., "Development of New Constitutive Equations for the Mullins Effect in Rubber using the Network Alteration Theory", *International Journal of Solids and Structures*, 43: 6817-6831 (2006).

[22] Chhabra, R., “Nonwoven Uniformity - Measurements Using Image Analysis”, *International Nonwovens Journal*, 43-50 (2003).

[23] Chocron S., Pintor, A., Cendon, D., Rosello, C., and Sanchez-Galvez, V., “Characterization of Fraglight Nonwoven Felt and Simulation of FSP’s Impact in It”, *Final Report to the US Army Research Contract No. N68171-00-M-5983.*

[24] Dafalias, Y.F., "Plastic Spin: Necessity or Redundancy", *International Journal of Plasticity*, 14(9): 909-931 (1998).

[25] Diani, J., Brieu, M., Vacherand, J.M., and Rezgui, A., “Directional Model for Isotropic and Anisotropic Hyperelastic Rubberlike Materials”, *Mechanics of Materials*, 36: 313-321 (2004).

[26] Diani, J., Brieu, M., and Gilormini, P., “Observation and Modeling of the Anisotropic Visco-Hyperelastic Behavior of a Rubberlike Material”, *International Journal of Solids and Structures*, 10: 3044-3056 (2006).

[27] Duling, R.R., Dupaix, R.B., Katsube, N., and Lannutti, J., “Mechanical Characterization of Electrospun Polycaprolactone (PCL): A Potential Scaffold for Tissue Engineering”, *Journal of Biomechanical Engineering*, 130(1): 011006-1-011006-13, (2008).

[28] Eidel, B., and Gruttmann, F., "Elastoplastic Orthotropy at Finite Strains: Multiplicative Formulation and Numerical Implementation", *Computational Materials Science*, 28: 732-742 (2003).

[29] Fitzgibbon, A., Pilu, M, and Fisher, R.B., "Direct Least Square Fitting of Ellipses", *IEEE Transactions on Pattern Analysis and Machine Intelligence*, 21(5), (1999).

[30] Fixman, M., and Kovac, J., "Polymer conformational Statistics. III. Modified Gaussian Models of Stiff Chains", *The Journal of Chemical Physics*, 58(4): 1564-1568 (1973).

[31] Y.C. Fung, K. Fronek and P. Patitucci, "Pseudoelasticity of Arteries and the Choice of its Mathematical Expression", *American Journal of Physiology: Heart and Circulatory Physiology*, 237: H620–H631 (1979).

[32] Gasser, T.C., Ogden, R.W., and Holzapfel, G.A., “Hyperelastic Modelling of Arterial Layers with Distributed Collagen Fibre Orientations”, *Journal of the Royal Society Interface*, 3: 15-35 (2006).

[33] Gong, R.H., Newton, A., “Image-analysis Techniques, Part I: The Measurement of Pore-size Distribution”, Journal of the Textile Institute, 83(2): 253-268 (1992).

[34] Gong, R.H., Newton, A., “Image-analysis Techniques, Part II: The Measurement of Fibre Orientation in Nonwoven Fabrics”, *Journal of the Textile Institute*, 87(2): 371-388 (1996).

[35] Gonzalez, C., and LLorca, J., "Stiffness of a Curved Beam Subjected to Axial Load and Large Displacements", *International Journal of Solids and Structures*, 42(5-6): 1537-1545 (2005).

[36] Grindstaff, T.H., and Hansen, S.M., “Computer Model for Predicting Point-Bonded Nonwoven Fabric Strength, Part I”, *Textile Research Journal*, 56(6): 383-388 (1986).

[37] Harrigan, T.P., and Mann, R.W., "Characterization of Microstructural Anisotropy in Orthotropic Materials using a Second-Rank Tensor", Journal of Materials Science 19: 761-767 (1984).

[38] Hart-Smith, L.J., “Elasticity Parameters for Finite Deformations of Rubber-like Materials”, *Zeitschrift fur Angewandte Mathematik und Physik (ZAMP)*, 17:608-626, (1966).

[39] Hearle, J.W.S., and Stevenson, P.J., “Studies in Nonwoven Fabrics, Part IV: Prediction of Tensile Properties”, *Textile Research Journal*, 34(3): 181-191 (1964).

[40] Holzapfel, G.A., Gasser, T.C., and Ogden, R.W., "A New Constitutive Framework for Arterial Wall Mechanics and a Comparative Study of Material Models", *Journal of Elasticity*, 61: 1-48 (2000).

[41] Holzapfel, G.A., "Nonlinear Solid Mechanics: A Continuum Approach for Engineering", 1st edition, Wiley (2001).

[42] Jahne, B., "Digital Image Processing", 6th edition, Springer, (2005).

[43] Jearanaisilawong, P., "Investigation of Deformation and Failure Mechanisms in Woven and Nonwoven Fabrics under Quasi-Static Loading Conditions", Master Thesis, MIT (2004).

[44] Jirsak, O., Lukas, D., and Charvat, R., "A Two-Dimensional Model of the Mechanical Properties of Textiles", *Journal of the Textile Institute*, 84(1): 1-15 (1993).

[45] Kanatani, K., "Distribution of Directional Data and Fabric Tensors", *International Journal of Engineering Science*, 22(2): 149-164 (1984).

[46] Kuhn, W., and Grun, F., "Beziehungen zwischen elastischen konstanten und dehnungsdoppelbrechung hochelastischer stoffe", *Kolloid Z.*, 101(3): 248 (1942)

[47] Komori, T., and Itoh, M., "A Modified Theory of Fiber Contact in General Fiber Assemblies", *Textile Research Journal*, 64: 519-528 (1994).

[48] Komori, T., and Itoh, M., "A New Approach to the Theory of the Compression of Fiber Assemblies", *Textile Research Journal*, 61: 420-428 (1991).

[49] Komori, T., and Itoh, M., "Theory of the General Deformation of Fiber Assemblies", Textile Research Journal, 61: 588-594 (1991).

[50] Kothari, V.K., and Patel, P.C., "Theoretical Model for Predicting Creep Behaviour of Nonwoven Fabrics", *Indian Journal of Fibre & Textile Research*, 26: 273-279 (2001).

[51] Lee, S.M., and Argon, A.S., "The Mechanics of the Bending of Nonwoven Fabrics", *Journal of the Textile Institute*, 74(1): 1-37 (1983).

[52] Lee, D.H., and Carnaby, G.A., "Compressional Energy of the Random Fiber Assembly, Part I: Theory", *Textile Research Journal*, 62: 185-191 (1992).

[53] Liao, T., Adanur, S., and Drean, J.Y., "Predicting the Mechanical Properties of Nonwoven Geotextiles with the Finite Element Method", *Textile Research Journal*, 67(10): 753-760 (1997).

[54] Liao, T., and Adanur, S., "Computerized Failure Analysis of Nonwoven Fabrics Based on Fiber Failure Criterion", *Textile Research Journal*, 69(7): 489-496 (1999).

[55] Marckmann, G., Verron, E., Gornet, L., Chagnon, G., Charrier, P., and Fort, P., "A Theory of Network Alteration for the Mullins Effect", *Journal of the Mechanics and Physics of Solids*, 50: 2011-2028 (2002).

[56] Marko, J.F., and Siggia, E.D., "Stretching DNA", *Macromolecules*, 28:8759-8770, (1995).

[57] Mulliken, A.D., and Boyce, M.C., "Mechanics of the Rate-dependent Elastic-plastic Deformation of Glassy Polymers from Low to High Strain Rates", *International Journal of Solids and Structures*, 43:1331-1356, (2006).

[58] Narter, M.A., Batra, S.K., and Buchanan, D.R., "Micromechanics of three-dimensional fibrewebs: constitutive equations", *Proceedings of the Royal Society of London, Series A*, 455: 3543-3563 (1999).

[59] Odgaard A., Kabel, J., van Rietbergen, B., Dalstra, M., and Huiskes, R., "Fabric and Elastic Principal Directions of Cancellous bone are closely related", *Journal of Biomechanics,* 30(5), 487-495 (1997).

[60] Pan, N., and Carnaby, G.A., "Theory of the Shear Deformation in Fibrous Assemblies", *Textile Research Journal*, 285-292 (1989).

[61] Patel, P.C., and Kothari, V.K., "Relationship between Tensile Properties of Fibres and Nonwoven Fabrics", *Indian Journal of Fibre & Textile Research*, 26: 398-402 (2001).

[62] Patel, P.C., and Kothari, V.K., "Effect of Specimen Size and Strain Rate on the Tensile Properties of Heat-sealed and Needle-punched Nonwoven Fabrics", *Indian Journal of Fibre & Textile Research*, 26: 409-413 (2001).

[63] Petterson, D.R., "On the Mechanics of Nonwoven Fabrics", Ph.D. Thesis, MIT (1958).

[64] Pourdeyhimi, B., Dent, R., and Davis, H., "Measuring Fiber Orientation in Nonwovens, Part III: Fourier Transform", *Textile Research Journal*, **67**(2):143-151 (1997).

[65] Pourdeyhimi, B., and Dent, R., "Measuring Fiber Orientation in Nonwovens, Part IV: Flow Field Analysis", Textile Research Journal, 67(3): 181-187 (1997).

[66] Scharcanski, J., and Dodson, C.T.J., "Texture analysis for estimating spatial variability and anisotropy in planar stochastic structures", *Optical Engineering*, 35(8): 2302-2309 (1998).

[67] Scharcanski, J., and Dodson, C.T.J., "Stochastic Texture Image Estimators for Local Spatial Anisotropy and Its Variability", *IEEE Transactions on Instrumentation and Measurement*, 49(5): 971-979 (2000).

[68] Schroder, J., and Neff, P., "Invariant formulation of hyperelastic transverse isotropy based on polyconvex free energy functions", *International Journal of Solids and Structures*, 40: 401-445 (2003).

[69] Spencer, A.J.M., "Part III Theory of Invariants", *Continuum Physics Volume 1-Mathematics*, Academic Press (1971).

[70] Termonia, Y., "Lattice Model for the Drape and Bending Properties of Nonwoven Fabrics", *Textile Research Journal*, 73(1): 74-78 (2003).

[71] Toll, S., "Note: On the Tube Model for Fiber Suspensions", *Journal of Rheology*, 37(1): 123-125 (1993).

[72] Treloar, L.R.G., "Physics of Rubber Elasticity", 3rd edition, University Press, Oxford (1975).

[73] Van Wyk, C.M., "Notes on the Compressibility of Wool", *Journal of Textile Institute*, 37:T285-T292 (1946).

[74] Wilde, T.P., "An Energy-based Model for the Compressive Behavior of Goose Down", Master Thesis, Georgia Institute of Technology (2004).

[75] Wu, X.F., and Dzenis, Y.A., “Elasticity of Planar Fiber Networks”, *Journal of Applied Physics*, 98: 093501 (2005).

[76] Wu, X., Levenston, M.E., and Chaikof, E.L., “A Constitutive Model for Protein-based Materials”, *Biomaterials*, 27:5315-5325 (2006).

[77] Wu, P.D., and van der Giessen, “On Improved Network Models for Rubber Elasticity and Their Applications to Orientation Hardening in Glassy Polymers”, *Journal of the Mechanics and Physics of Solids*, 41(3): 427-456 (1993).

[78] Xu, B., Pourdeyhimi, B., and Sobus, J., “Characterizing Fiber Crimp by Image Analysis: Definitions, Algorithms, and Techniques”, *Textile Research Journal*, 62(2) 73-80, 1992.

[79] Yu, J.H., Fridrikh, S.V., and Rutledge, G.C., "Production of Submicrometer Diameter Fibers by Two-fluid Electrospinning", *Advanced Materials*, 16(17):1562-1566 (2004).

[80] Zheng, Q.S., "Theory of representations for tensor functions - A unified invariant approach to constitutive equations", *Applied Mechanics Reviews*, 47(11): 545-586 (1994).

[81] Zysset, P.K., and Curnier, A., "An Alternative Model for Anisotropic Elasticity Based on Fabric Tensors", *Mechanics of Materials*, 21: 243-250 (1995).

[82] Zysset, P.K., and Goulet, R.W., and Hollister, S.J., "A Global Relationship between Trabecular Bone Morphology and Homogenized Elastic Properties", *Journal of Biomechanical Engineering*, 120: 640-646 (1998).

[83] Curnier, A., "An Alternative Model for Anisotropic Elasticity Based on Fabric Tensors", *Mechanics of Materials*, 21: 243-250 (1995).